UNIVERSITY OF CALIFORNIA
RIVERSIDE

Integrating New Methodologies and Materials Towards Advanced Surface Plasmon Resonance-Based Bioanalysis

A Dissertation submitted in partial satisfaction
of the requirements for the degree of

Doctor of Philosophy

in

Chemistry

by

Alexander Scott Lambert

June 2022

Dissertation Committee:
Dr. Quan Cheng, Chairperson
Dr. Min Xue
Dr. Haofei Zhang

The Dissertation of Alexander Scott Lambert is approved:

_____

_____

_____

Committee Chairperson

University of California, Riverside

ACKNOWLEDGEMENT

It has been my enduring privilege to spend the last five years at the University of California Riverside. Though I am excited for what the future holds for me, the people I have known and the experiences that I have had at this institution can never be replaced. First and foremost, I would like to thank my advisor and mentor, Professor Quan Jason Cheng. Your advice and support have helped to shape the scientist and researcher that I am now, and I am eternally grateful.

I would like to thank the staff and faculty at UCR, especially my committee members Profs. Min Xue and Haofei Zhang, who have provided much guidance and encouragement throughout my years here, both at the official stages of progression and for their kind words that have allowed me to receive various supports from unexpected sources. I would also like to thank Prof. Yinsheng Wang and the Environmental Toxicology Department at UCR for the two years of training and support via the T32 Training Grant. The work I did and people I met though that opportunity has helped me tremendously in finding new possible paths in my career. I also want to thank Profs. Greg Beran and Leonard Mueller from the bottom of my heart for their aid and support in the more volatile moments of my time at UCR. I also want to thank the UCR Graduate Student Association for the funding of several of my conference experiences, including Pittcon 2019, ACS 2019, Pittcon 2020, and Sample Treatment 2021.

I would also like to thank the many members of the Cheng lab past and present, who have helped with training, advice, brainstorming and companionship across all aspects of this academic experience, from classes to research to writing to conferences. The biggest

help in my early time here was from Dr. Kelvin Tran, who showed me the ropes and the tools of the trade for our style of investigations. I want to thank the visiting scholars and professors to the lab, especially Prof. Ichiro Tanabe, whose advice and guidance helped jump start one of the central projects of the following work.

Lastly, and most importantly, I want to thank my family. Their love and support throughout my life instilled the love of learning and persistence that led me to this point. To my wife, my sun and stars, Miatta Lebile, I literally never would have even made it to this point in my life and career without you, and I can't wait to start this next chapter of our lives together.

COPYRIGHT ACKNOWLEDGEMENT

The text of Chapter 1, Section 1.7 of this dissertation was previously published, reprinted with permission from *ACS Sens.* **2018**, *3*, 12, 2475-2491, with adaptation. The corresponding author, Dr. Quan Jason Cheng, directed and supervised the research that formed the basis of that chapter.

The text and figures of Chapter 4 of this dissertation were previously published, reprinted with permission from *Anal. Chem.* **2020**, *92*, 13, 8654-8659. The corresponding author, Dr. Quan Jason Cheng, directed and supervised the research that formed the basis of that chapter.

ABSTRACT OF THE DISSERTATION

Integrating New Methodologies and Materials Towards Advanced Surface Plasmon Resonance-Based Bioanalysis

by

Alexander Scott Lambert

Doctor of Philosophy, Graduate Program in Chemistry
University of California, Riverside, June 2022
Dr. Quan Cheng, Chairperson

Advances in life sciences in recent decades have revolutionized our understanding of biochemical and biophysical interactions associated with diseases and disorders of the human body. This newly acquired knowledge has fueled intense interest in a range of biotechnological strategies that can improve health outcomes, spanning from biosensors to drug development to tissue engineering. There is thus an increasing need for even better understanding of biomolecular interactions at nanoscale to explore new medical frontiers, and for powerful analytical tools of increasing complexity and diversity in multiplexed bioanalysis. Surface plasmon resonance (SPR) is a core optical spectroscopic principle in the bioanalytical sphere, and its label-free methodology for bioassays has been broadly applied in drug discovery, medical diagnosis, and environmental monitoring. Advances in materials sciences, however, have provided new opportunities for re-invention of the technique and expansion of the range of analyses by SPR. The aim of this dissertation is to develop and improve the fundamental technological diversity of SPR based techniques for enhanced biosensing applications.

The main strategy for the development takes the form of integrating novel methodologies and new materials to the SPR bioanalytical workflows. First, an orthogonal analytical platform was developed by combining SPR/SPR imaging with matrix-assisted laser desorption ionization mass spectrometry (MALDI-MS). A multistep functionalized plasmonic microarray was developed into a new mode (SPR-MALDI) for the sensitive detection of bacterial toxin proteins in complex environmental matrices. The combination of the techniques allowed for both quantitative determination and unambiguous qualitative identification of biological identity of the target. Second, SPR techniques were integrated with three-dimensional (3D) printing for enhancing analytical performance. A novel hybrid 3D printing and PDMS molding process was developed that overcomes fundamental resolution limits of the 3D printed optical components for spectroscopy. Prisms of multiple geometries were fabricated that demonstrated surface roughness comparable to commercial, glass-based components, providing economical alternative while yielding high sensitivity towards SPR biosensing of protein targets. Finally, we have developed a high performing SPR platform based on a more fundamental shift, switching the plasmonic material from gold to aluminum. Al thin films under Kretschmann configuration demonstrated a 60 % higher optical sensitivity in imaging mode and reduced surface fouling by 75 %. They proved excellent substrates for array-based chemical surface modifications by ionic polymers that were further employed for successful analysis of urine-based chemokine biomarkers. The work presented here should pave the way for more complex modalities in developing the next generation of biotechnology.

TABLE OF CONTENTS

LIST OF FIGURES

LIST OF TABLES

Chapter 1: Introduction and Background

1.1 Introduction

This chapter aims to present and discuss the relevant subject areas that form the basis of the research presented in the proceeding chapters. Principle areas of discussion will include the roles and technical aspects of optical biosensing, the fundamentals and roles of surface plasmon resonance-based analysis within that broader field. The ever-advancing march of technology constantly creates new avenues of investigation into every subject area, including SPR and biosensing. The remaining sections will thus expand on the areas of three-dimensional (3D) printing, mass spectrometry, and novel materials as they relate to and improve the scope and applicability of SPR-related techniques.

1.2 Principles of Biosensors

Biosensors are a core component of biomedical analysis, disease and pathogen detection, defense, agriculture, and environmental monitoring.[1-5] The term "biosensor" simply derives from the ability to recognize and signal a biological component of interest, and the basic form of a biosensor requires three main features (see Figure 1.1): (1) a recognition element of the target of interest; (2) a transducing mechanism that communicates the recognition into (3) a measurable readout by a user.[6] The first component, the recognition element, can be any biological molecule that can bind to a target of interest, and is a huge area of research interest. Examples include antibodies, aptamers, native binding pairs, DNA/RNA, and cells.[7] The second component, a transduction mechanism, is usually inherent in the materials or instrument used. This can be an electric or magnetic field that is perturbed by the recognition event, or a fluorescent

or luminescent emission induced at the site of recognition by components attached to the recognition element, among many others. The final measurable readout is simply a quantitation of the transduced signal by a detector, either optical, electrical or biological (eyes).

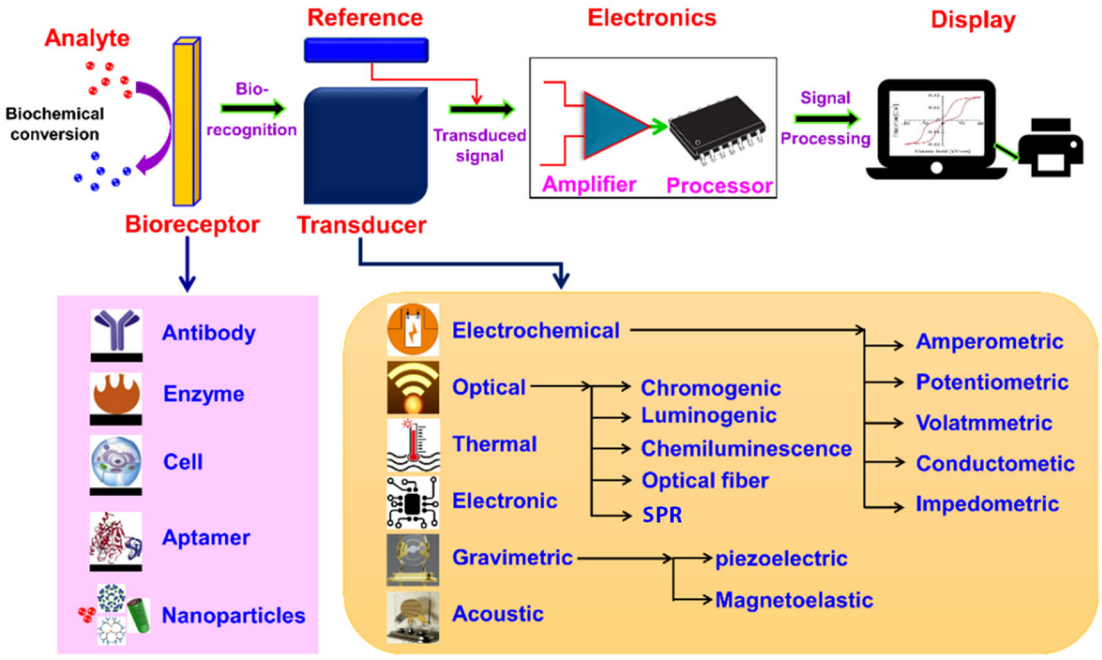

Figure 1.1. Summary of biosensor components. Reprinted from Reference 6.

Biosensors can be qualitative, indicating the presence of a given target of interest, or quantitative, giving a specific concentration or amount of the target. A large portion of biosensor applications is in the diagnosis and monitoring of diseases by monitoring specific molecular components that point towards states of disease, such as small molecules like glucose or hormones, proteins like antibodies or interleukins, or whole cells.[6] The most common examples in consumer products are glucose monitors, a quantitative type of electrochemical assay, and pregnancy tests, a qualitative type of lateral flow assay.

Biosensing schemes are typically much more user-friendly, faster, and more portable than other detection types,[8] and so are well-suited to the problem of widespread diagnosis and monitoring required in a large-scale health emergency. More intricate lab-based assays, such as PCR and culture tests, take much more time (hours to days) than a typical biosensor (minutes to hours), and require much more expertise on the part of the user. The increasing need for easy to use and effective tools for medical diagnosis is especially pertinent in light of the recent pandemic of COVID-19, the disease caused by the virus SARS-CoV-2. Community monitoring of levels of viral spread is vital to health outcomes in the near and long term of a given outbreak.

Additionally, biosensors are broadly used in the fields of drug discovery and biomedical analysis, as they fundamentally quantify the interaction between targets of interest. The biological centers of many internal diseases such as cancer and autoimmune disorders are proteins that participate in signaling cascades that result in these negative outcomes. Biosensors provide a means of analyzing disease-related biology in two primary ways. First, sensing and quantifying the levels of disease related proteins acts as a way to diagnose a disease or disorder, such as with antibodies to double-stranded DNA indicating the onset of lupus-related illnesses. Most prominently, lateral flow assays have been developed and distributed around the world for the diagnosis of COVID-19 based on the quantification of the viral spike (S) protein or nucleocapsid (N) protein, tests that are commonly referred to as “antigen tests”. Second, biosensors are a means to study the biological pathways of a disease, as with studies that induce a disease or negative health state and measure the changes in a given protein. Biosensors have been implemented

extensively in this capacity, as proteomic studies frequently use them as a primary means of quantitation.[9-12]

Biosensors can be further divided into labeled and label-free techniques. Labeled techniques, such as enzyme-linked immunosorbent assay (ELISA), includes a non-native component attached to the recognition element that is used as the means of signal generation. In the case of ELISA, an initial antibody for the analyte of interest is incubated, followed by a secondary antibody, such as an immunoglobulin G (IgG), that binds to the stalk of the initial antibody. A horseradish peroxidase or similar enzyme is ligated to this secondary antibody that catalyzes the formation of a fluorescent form of a small molecule that is also added to the solution. These techniques are very high sensitivity but are complex and do not directly sense the actual recognition interaction.

Label-free techniques, as the name implies, have operating principles that detect the presence of an analyte without the secondary component. This can take the form of an electric or magnetic field that is perturbed by mass changes or based on tension changes. Common examples of label-free techniques include field-effect transistors (FETs), magnetoelastic sensors, quartz crystal microbalance (QCM) and optical biosensors like surface plasmon resonance (SPR). Label-free techniques directly sense the analyte binding interaction, and so give signal quickly, in realtime, enabling integration into constant monitoring configurations. The lack of a tag also removes any hindering constraints from the added material, a large benefit when sensing very small targets like small molecules, peptides, or lipids. Label-free techniques are frequently very sensitive to mass or material changes at the surface of any kind. Though this is a benefit, care is usually taken to ensure

that only the specific target interactions are being measured. While label-free techniques have many benefits over labeled techniques, fouling and concurrent non-specific interactions are the central challenge to their use, one that been the subject of much investigation.

1.3 Theoretical Basis of SPR

The basic working principle of SPR is that the nanoscale optical environment of a surface is sensitive to changes from the binding of new materials, thus shifting the "SPR angle" in a linear response. While straightforward in analysis, the fundamental underpinnings of SPR spectroscopy and related techniques rely on a delicate and complex interplay of several optical relationships. Multiple chapters in this work revolve around these fundamental optical interactions, so a summary of the relevant concepts is presented here.

1.3.1 Total Internal Reflection and Evanescent Fields

Plasmonic absorption can occur and alter incident radiation under many different conditions, including from directly perpendicular light sources, so transmission-based configurations are not uncommon in the plasmonic research space.[13-15] Perturbations from plasmonic coupling form the basis of a wide range of techniques in this category, such as surface-enhanced Raman scattering and extraordinary optical transmission.[16-18] However, the most common modes of SPR involve the total internal reflection (TIR) configuration, where incident radiation is passed through mediums of two different refractive index n_1 and n_2, above the critical angle, θ_c such that the light is entirely or almost entirely reflected,

rather than transmitted or refracted, as shown in Figure 1.2. From Snell's law,[19] this critical angle, θ_c, is defined by:

$$\theta_c = \sin^{-1}\frac{n_2}{n_1} \tag{1.1}$$

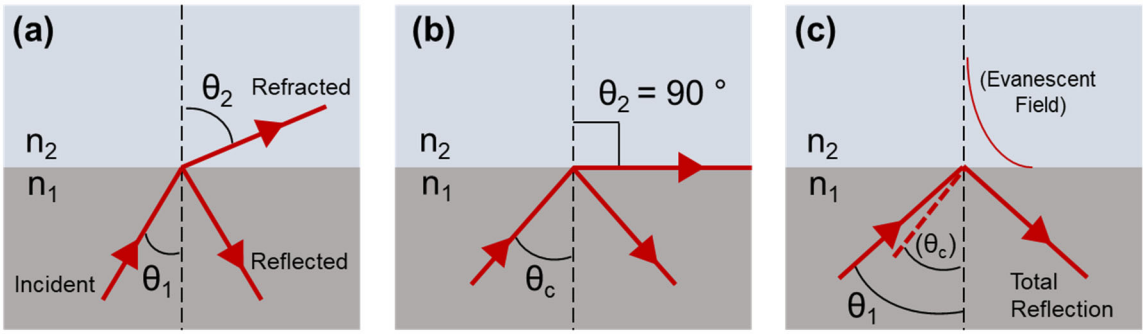

Figure 1.2. Reflection and/or refraction when (a) $\theta_1 < \theta_c$. (b) $\theta_1 = \theta_c$, and (c) $\theta_1 > \theta_c$.

When using this effect for analytical purposes, the n_1 region is often an optical component, or optical coupler, that is constructed of high refractive index material. This TIR effect forms the basis of many basic and modern technologies, such as cameras, telescopes, and optical fibers.[20] For analytical purposes, the TIR effect is most notable for creating an evanescent field, a localized oscillation of the electrons at the surface, in the n_2 region, i.e. the immediate vicinity of the surface.[21] The amplitude of the standing wave decays exponentially with distance from the surface, and the wave vector of the evanescent field, k_{ev}, that runs parallel to the n_1/n_2 boundary is given as:

$$k_{ev} = \frac{\omega}{c}\sqrt{\varepsilon_p}sin\theta \tag{1.2}$$

where c and ω are the speed of light in a vacuum and the angular frequency of the incident light, respectively. Alternate formulations are possible given that $2\pi c = \lambda\omega$, and that, for non-dispersive media, the refractive index is the square root of the permittivity dielectric constant, ε:

$$k_{ev} = \frac{2\pi}{\lambda} n sin\theta \qquad (1.3)$$

The penetration depth of the evanescent field is generally defined by the wavelength of light being reflected at the n_1/n_2 barrier and extends a distance ~ λ/2 nm. Since the critical angle is partially defined by n_2, chemical or physical changes in the n_2 region will change the coupling conditions. Many electronically and optically active materials can be used as a means of sensing the region outside the surface, and fiber optic sensors have been developed that sense the many spectral ranges at the surface.[22]

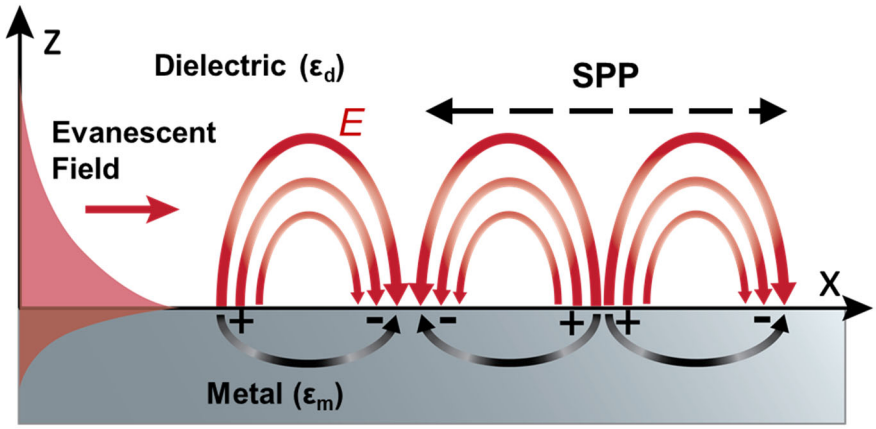

Figure 1.3. Cartoon depiction of an excited surface plasmon polariton at a metal/dielectric interface.

1.3.2 Surface Plasmons

When the TIR effect described above is used in conjunction with a metal and prism, surface plasmons are excited. Surface plasmons arise as a collective oscillating excited state of the electrons in the conduction band of a solid material at its interface with another material (or "surface", if the other material is liquid or gas). Mathematically, surface plasmons can be predicted from applying Maxwell's equations to material surfaces. The effect was theoretically predicted in 1957,[23] and experimentally verification was reported in 1959,[24] but available technology limited their practical application across many fields until the 1980s. The free electrons in the surface conduction band are resonantly excited by the momentum transfer (absorption) of an incident photon of appropriate energy and momentum. This removes that photon from being reflected, so the resonant absorption creates a very large perturbation to the outgoing light intensity and resulting spectra, generating the so-called "plasmonic dip" at angles higher than the TIR critical angle. This plasmonic behavior can be predicted by multilayer Fresnel equations, and key empirical parameters of a metal's behavior are its *n* and *k*, the real and imaginary portions of the refractive index. Reflected spectra in a two-layer system can be modeled with two of the four classical Fresnel equations:

$$r_s = \frac{\boldsymbol{n}_1 \cos\theta_i - \boldsymbol{n}_2 \cos\theta_t}{\boldsymbol{n}_1 \cos\theta_i + \boldsymbol{n}_2 \cos\theta_t} \tag{1.4}$$

$$r_p = \frac{\boldsymbol{n}_2 \cos\theta_i - \boldsymbol{n}_1 \cos\theta_t}{\boldsymbol{n}_2 \cos\theta_i + \boldsymbol{n}_1 \cos\theta_t} \tag{1.5}$$

where $\mathbf{n}_1$ and $\mathbf{n}_2$ have been expanded to represent the complex refractive indices $\mathbf{n}_1 = n_1 + ik_1$ of the materials and r_s and r_p are the s- and p-polarized portions of the reflected light. A three-layer Fresnel system, using a prism, metal, and surface layer is more common (see Figure 1.4) but also more complex, while full treatments have been reported,[25] in practice, software packages can calculate expected spectra. The fundamental physical source of the *n* and *k* of a given material is typically explained by the Lorentz-Drude model of electron transport in materials.[26] The reflectivity coefficient for a thin film independent of incident angle via Lorentz-Drude is given by:

$$\mathrm{R} = \frac{(n-1)^2+k^2}{(n+1)^2+k^2} \tag{1.6}$$

The n and k values are themselves defined by the material's relative dielectric functions ϵ_r and ϵ_i and its relative magnetic permeability, μ_r:

$$n = \sqrt{\frac{\mu_r}{2}\left(\sqrt{\epsilon_r^2+\epsilon_i^2}+\epsilon_r\right)} \tag{1.7}$$

$$k = \sqrt{\frac{\mu_r}{2}\left(\sqrt{\epsilon_r^2+\epsilon_i^2}-\epsilon_r\right)} \tag{1.8}$$

Most metals used for plasmonics (Au, Ag, Cu, Al, Ti, Ta, etc.) are non-ferromagnetic, so $\mu_r \approx 1$. Pursued further, the dielectric functions are themselves defined in terms of the frequency of the incident light ω, the metal plasma frequency ω_p, and the metal damping frequency Γ:

$$\epsilon_r = 1 - \frac{\omega_p^2}{\omega^2 + \Gamma^2} \qquad (1.9) \qquad\qquad \epsilon_i = \frac{\omega_p^2 \Gamma}{\omega(\omega^2 + \Gamma^2)} \qquad (1.10)$$

The plasma frequency is one of the fundamental physical properties most shaping the behavior of materials towards plasmonic excitation, and is defined by:

$$\omega_p^2 = \frac{Ne^2}{m\epsilon_0} \qquad (1.11)$$

where N is the metal's free electron density, e and m are the charge and mass of an electron, respectively, and ϵ_0 is the permittivity of free space.

1.3.3. Surface Plasmon Resonance Spectroscopy

Though surface plasmon excitation is itself unidirectional, when the plasmonic layer is a thin film of a metal, the increased absorption leading to the reflected spectral dip is due to the evanescent field from the TIR reflection coupling to the collective plasmonic excitation states of the surface. These collective states manifest as what is termed a propagating surface plasmon polariton (SPP). The wave vector of the SPP is defined by[27]:

$$k_{sp} = \frac{\omega}{c}\sqrt{\frac{\varepsilon_{mr}\varepsilon_s}{\varepsilon_{mr} + \varepsilon_s}} \qquad (1.12)$$

When the k_{sp} matches the k_{ev} of the incident photon (Eqn. 1.2), the photon is absorbed into excitation of the SPP (see Figure 1.4). As the dielectric values or refractive index at the surface shifts, the angle or wavelength of maximum absorption, i.e., minimum reflected intensity, will also shift. The shift in reflected spectral intensity, plotted either angularly or by wavelength, forms the basis of SPR spectroscopy.

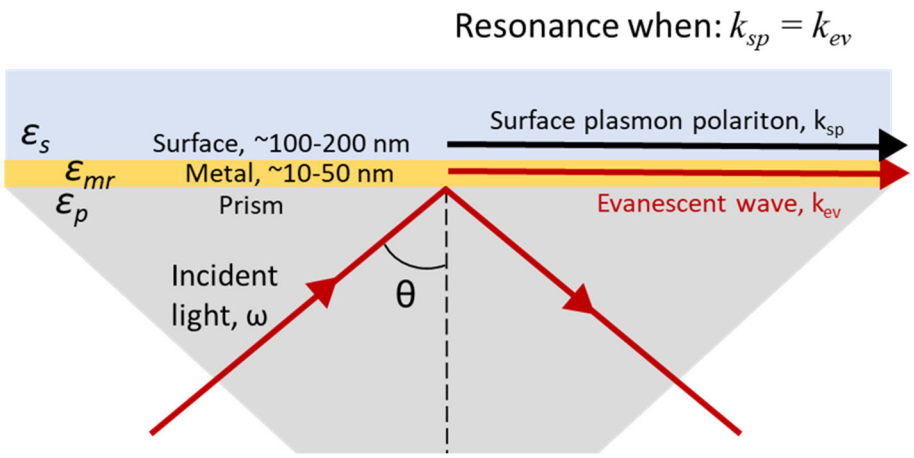

Figure 1.4. Kretschmann configuration of SPR, indicating the resonant matching condition based on the incident light wavelength, angle, and relative dielectric values.

SPR instruments larger utilize the Kretscshmann configuration, as shown in Figure 1.4 and originally proposed in 1968.[28] The geometry is an ATR setup, where a plasmonic film is placed directly in contact with both the prism and the analyte solution, and forms the basis of all commercialized versions of SPR spectroscopy. The source laser or LED, usually 650-700 nm, is aimed at the desired angle, and scanned either angularly or by wavelength. For angular versions, either the incident angle is physically rotated, or the system is fixed and a photodiode array at the collection point generates the angular displacement of the reflected light. In wavelength scanning mode, a broad white light sourced is used, the system remains fixed, and a spectroscopic grating separates the reflected intensities into the analyzed spectra. Some reports use the alternative Otto configuration, that separates the prism from the sensing surface,[29-32] if one of the operating materials interacts unfavorably with aqueous solutions. Fiber optic SPR uses a form of ATR in combination with a waveguide material, so that signals can be introduced and drawn out in a very small space, such as a fiber optic cable.[33] This method has high

practicality and convenience towards experimental configurations, as the fiber optic can function as a probe to dip into an analyte solution. The downside is that results are typically difficult to make consistent, as the light path within the cable alters enough with the movement of the probe arm that it alters the highly sensitive plasmonic response outside of analyte binding.

The evanescent field from the TIR incident light can also couple to individual plasmonic particles whose size is smaller than the wavelength of the incident light. When nanoparticles and nanostructures of this size regime (approximately less than 500 nm) are exposed to the corresponding radiation, a localized surface plasmon is excited and oscillates from one side of the structure to the other. This behavior of the plasmonic absorption and resulting scattering is highly dependent on the geometry of the nanostructure, and the overall process is usually termed localized surface plasmon resonance (LSPR).[34] This effect is not directionally specific, so LSPR can be used in a number of other configurations other than TIR.

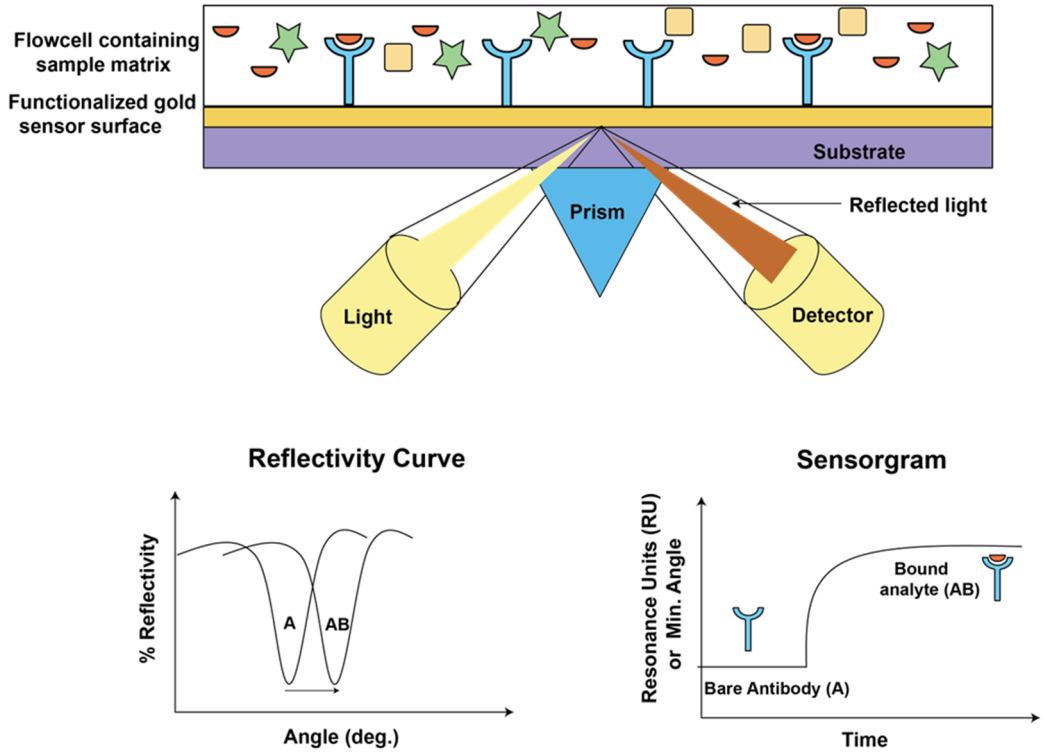

Figure 1.5. Typical SPR-based biosensing configuration with a single analyte and sensing/receptor element, along with a diagram of the generation of a sensorgram based on the shift in the angle of minimum reflected intensity. Reprinted from Reference 35 with permission of Springer.

An experimental readout, known as a sensorgram, is shown in Figure 1.5, where a single component is bound to the sensor surface.[35] Technically, the shift in "binding signal" is simply caused by a change in the dielectric environment or refractive index at the surface, translated into a changing n_2 or ε_1 in the above equations. This shifts the position of minimum reflected intensity, sometimes called the "SPR angle", to a new angle or wavelength, which is tracked on the y-axis over time. Practically, the shift is representative of the binding of solid or semisolid materials to the surface, as the experimental conditions are usually such that the existing n_2 layer is air, water or aqueous buffer. These typically have refractive indices (RIs) of 1.00-1.34, while analytes such as biological materials have

RIs of approximately 1.6.[36] The shift in the sensorgram thus reflects a replacement and increase of the average RI of the n2 region at the surface, and so a linear relationship can be drawn to the deposited or bound analyte.[37]

Alternatively, SPR spectroscopy can be used to determine film thicknesses and absolute quantities of mass at the surface.[38-40] This is accomplished via the well-established relationship:

$$R = m(\eta_a - \eta_s)[1 - e^{-\frac{2d}{l_d}}] \quad (1.13)$$

where R is the reflected signal shift (wavelength, angle, or intensity), m is the sensitivity over small refractive index (RI) increments, η_a is the RI of the adsorbed layer, η_s is the RI of the overall solution, d is the layer thickness, and l_d is the decay length of the evanescent field (based on the incident wavelength from the light source).[41]

1.3.4 SPR Imaging

A major alternative mode of SPR based analysis, SPR imaging, makes use of the shift in plasmonic dip in a different way.[42] As shown in Figure 1.6, if a specific angle between the TIR angle and the SPR angle, then the intensity of the reflected light will be shifted higher upon binding of analytes to the surface.[43] Most centrally, SPR monitoring at a fixed angle greatly expands the total analyzable area; since the tracked signal is a pure intensity, full images with a camera can be dataset. As a result, the spatial resolution of the image and substrate may be taken into account, enabling array-based analysis. SPR imaging is thus considered to be the high-throughput version of SPR spectroscopy. Higher-

throughput traditional SPRs are offered with increasing frequency by major manufacturers such as Biacore and Bruker, but SPR imaging is natively highly multiplexable and high-throughput. Technically, each pixel on the image can serve as an individual experiment, though Regions of Interest (ROI) are usually chosen by the user or a software algorithm. Fixed-angle intensity-based analysis is typically more practical to implement in a device, so SPR imaging has good potential to be used as the method for practical devices. SPR imaging with microarrays has been reported for biomarker panels of proteins, cells, and nucleic acids.[44-50]

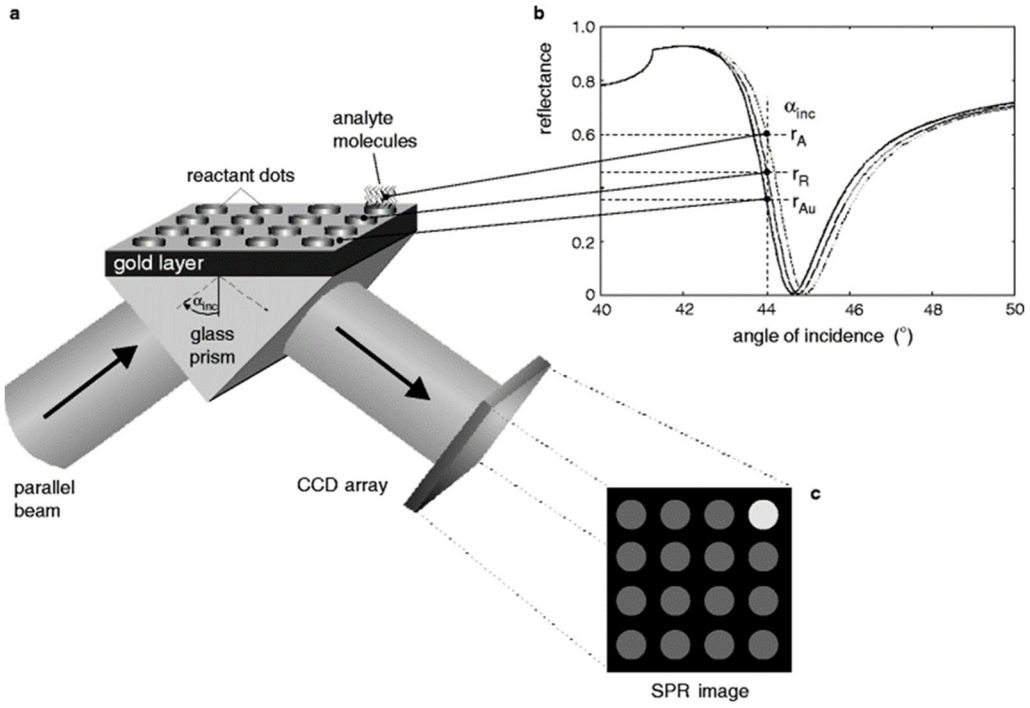

Figure 1.6. SPR imaging with a fixed angle, detecting change in reflected intensity. Wells with bound analyte shift the reflectivity curve further, and thus have higher intensity. Reprinted from Reference 43 with permission of Springer.

Additionally, fixed-angle imaging modes have the upside that they can be further converted into microscopy-based methods, or surface plasmon resonance microscopy (SPRM). Multiple sources have pursued SPRM and found that individual cells and even proteins can be analyzed and quantified in their binding and motion.[51-53] This is a highly useful aspect, as single-cell imaging can analyze for both their collective behavior and individual cell heterogeneity, a point of significant interest in modern cell-based studies.

Drawbacks of imaging modes include the potential for noise at individual spots and minor surface inconsistencies leading to slightly altered spectral shapes and different sensitivities. These issues can be overcome by utilizing the high volume of data that is natively obtainable with SPR imaging. Control regions can account for the variation in sensitivity between individual surface preparations and the collective use of a high number of large regions of interest (and many wells when in microarray form) serve to normalize out any variations. Additionally, data processing and machine learning algorithms have been reported that further improve the data classification from high-volume imaging analysis.[54]

1.4 Plasmonic Materials

In principle, many metals may be used for their plasmonic properties. A broad range of metals have the plasma frequency to be used in the visible or IR regions as a plasmonic substrate, such as Cu, Al, In, Ag, Pt, Pd, W and Ti. However, the most common and most commercialized form of SPR, thin films in the Kretschmann configuration, almost exclusively uses Au films of ~50 nm, with over 99% of reported SPR spectroscopy applications.[55] This is for three principal reasons. First, Au films have a very well-defined,

sharp, “plasmonic dip” that is easy to pinpoint regardless of the quality of surface preparation. Second, gold films are considered to be chemically stable across many experimental conditions. This is in particular comparison to Ag films, which have similar positive plasmonic properties to Au, but suffer harsher sulfur fouling in ambient conditions.[56] Third, Au films have a very straightforward functionalization pathway, that of the Au-thiol bond. For bioanalytical purposes, many types of biological components need to be immobilized to the sensor surface, and thiols are both an easy functional group to synthesize onto the end of a small-chain molecule, such as 16-mercaptohexadecanoic acid, as well as a naturally-occurring amino acid component of proteins. While the exact nature of the Au-thiol bond is still a matter of investigation, the relative ease of use with Au film functionalization, along with the other benefits, make Au films a relatively practical choice for SPR thin film applications.

However, there is an increasing interest in alternative materials with strong plasmonic characteristics.[57] While Au films have good benefits, the scope of possible research is necessarily limited to the capabilities of Au films. First, Au films have an optical absorption range that cuts off below 500 nm, and plasmonic absorption signal significantly degrades in quality below ~600 nm.[58] This is due to the fundamental band structure of gold, as the interband threshold (IT) for gold is ~500 nm, and electrons excited above the energy cut-off (i.e. lower wavelength) will predominantly excite electron-hole pairs, thus not participating in the conduction-band excitation of plasmonic absorption.[59] By comparison, multiple other metals, including aluminum, indium, and titanium, have alternate band structures that allow them to maintain their metallic character at higher energies and thus

lower wavelengths.[60] Second, while the Au-thiol bond is very useful for immobilization, it places a cap on the space of targets that can be functionalized to the surface. More functionalization pathways via a wider variety of coupling chemistries would allow more flexibility in methodological development. Finally, Au films present specific challenges in medical devices due to its natural affinity for fouling interactions even while being chemically inert. Gold as a material is naturally hydrophobic, thus is vulnerable to non-specific sticking from the many protein components present in blood, serum, plasma, sputum or cerebrospinal fluid matrices common in medical applications. Furthermore, the gold-thiol bond is a double-edged sword, as while it is a convenient means of immobilizing most proteins, it is also a source of direct pull-down of non-target proteins with cysteines. While there is a broad depth of literature directed towards surface chemistry that protects the Au surface from non-specific binding,[61-65] it is a fundamental issue that must be accounted for in essentially every biosensing application that uses Au films.

1.4.1 Aluminum for Plasmonics

The original observations of plasmonic behavior in aluminum films can be traced back to the original experimental confirmation of surface plasmons in 1959, with the observation of a plasmonic peak in electron energy loss spectra of aluminum.[24] In more modern times, aluminum has attracted increasing interest as a plasmonic substrate. Its positive traits stem from its basic plasmonic parameters. As a result band structures discussed previously, aluminum has an ω_p of ~15 eV, while gold is ~8 eV.[60, 66] The quasi-static surface plasmon frequency is $\omega_s = \omega_p/\sqrt{2}$ at a simplified metal-air interface, and plasmons are expected to be generated in the range of $0 \leq \omega \leq \omega_s$.[67] This higher frequency

for aluminum thus allows plasmonic coupling with higher-frequency radiation and thus a broader plasmon tuning range than silver or gold,[68] as shown in Figure 1.7. This characteristic has several further downstream effects, as the imaginary portion of the refractive index, *k*, is highly determinant of a metal's plasmonic behavior and *k* is ~7.5 for Al and ~3.0 for Au in the red-visible range.[69] Aluminum also presents an opportunity due to its plasmonic absorption in the UV range. Recent reports have shown that organic materials can be quantified using the far-UV range as the probe beam.[70, 71] This analysis is enhanced by the absorption of organic materials in the same range, which couples to the incident beam through plasmon-exciton coupling, a phenomenon well-established since the early days of SPR spectroscopy. This type of analysis is not possible with Au or Ag films.

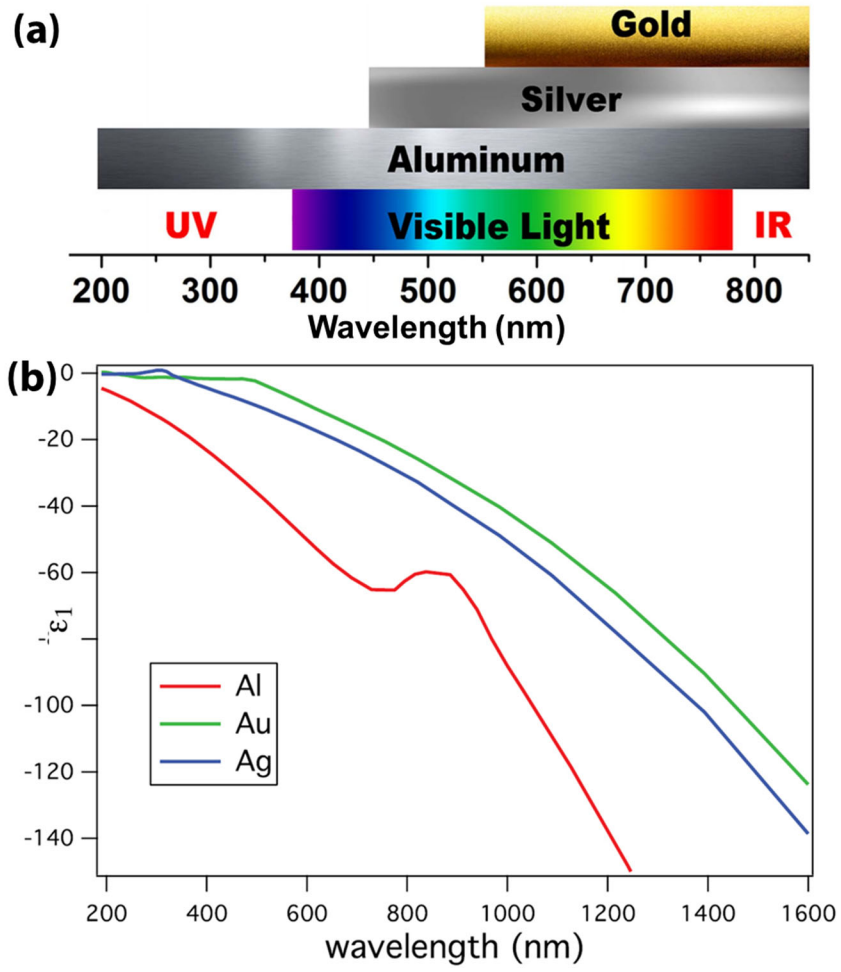

Figure 1.7. (a) Plasmonic tuning ranges of the plasmonic materials of Au, Ag and Al. Reprinted from Reference 68 with permission of IOP Publishing. (b) Real part of the dielectric functions for aluminum, gold and silver. Reprinted from Reference 67 with permission of IOP Publishing.

Furthermore, the potential use of dual-wavelengths for SPR analysis has been reported since the mid-1990s.[72, 73] The increase in parameters has many potential avenues of benefits of analysis. First, the determination of objective dielectric optical constants is possible along with film thickness, but only through the use of two separate wavelengths setting up a system of equations with Eqn. 1.13.[41] Refractive index is typically assumed to

be constant in this mode of analysis to simplify to the standard form,[74] but this does not hold for optically active materials, such as metal nanoparticles or fluorescent proteins. Additionally, wavelengths of different sensitivity to near- vs far-range binding or surface vs bulk response allow sensors to be self-referential and normalize binding response.[75, 76] Finally, multiple wavelength channels allow simple addition of their change in values, at minimum doubling or tripling the sensitivity of a given scheme.[77-79] With Au films, this potential is limited by the smaller range of visible wavelengths. Multiwavelength models of SPRs are commercially available,[80] but the close wavelength proximity between the channels (e.g., 670 nm and 785 nm) limits the differentiation in response.

Aluminum is well-known as a plasmonic material in nanostructure form,[81-87] but aluminum as plasmonic substrate is often associated with a number of challenges that hinder its analytical implementation, especially in thin film form. A primary concern is the chemical and structural stability of aluminum and aluminum oxide in aqueous conditions.[88, 89] Additionally, oxidation along the surface area of aluminum nanostructures, especially at sharp tips, can decrease the sensitivity of spectra to changes in refractive index.[90] For larger-scale aluminum films and larger-feature nanoscale materials, the oxidation could be impactful on aluminum's plasmonic performance. The range of experimental reports that have utilized aluminum is very limited. If robust experimental work is to be conducted, much fundamental work about Al thin films plasmonic behavior and performance is greatly needed and is discussed in Chapters 4 and 5.

1.5 SPR-based Biosensing and Bioanalysis

1.5.1 Fundamental Approaches

SPR provides several of the biosensing benefits discussed in previous sections. It is label-free, so the signal readout is a direct detection of interactivity at the surface. It is also real time, so results are essentially immediate, not requiring the successful applications of a slate of secondary steps afterwards. As such, SPR can be employed both as a quick method of bioanalyte detection[91] or as a means of constant monitoring of environmental contaminations.[92] As a further expansion of the realtime data acquisition, the binding of material to the surface, as represented in a sensorgram, is subject to the standard relationships of mass transfer kinetics. The association, steady state, and dissociation regions of the sensorgram (see Figure 1.8) at a range of concentrations can be converted into affinity (K_d), association rate (k_a) and dissociation rate (k_d).[93] This makes up one of the long-time core applications of SPR, as a means of determining drug-target affinities.[94]

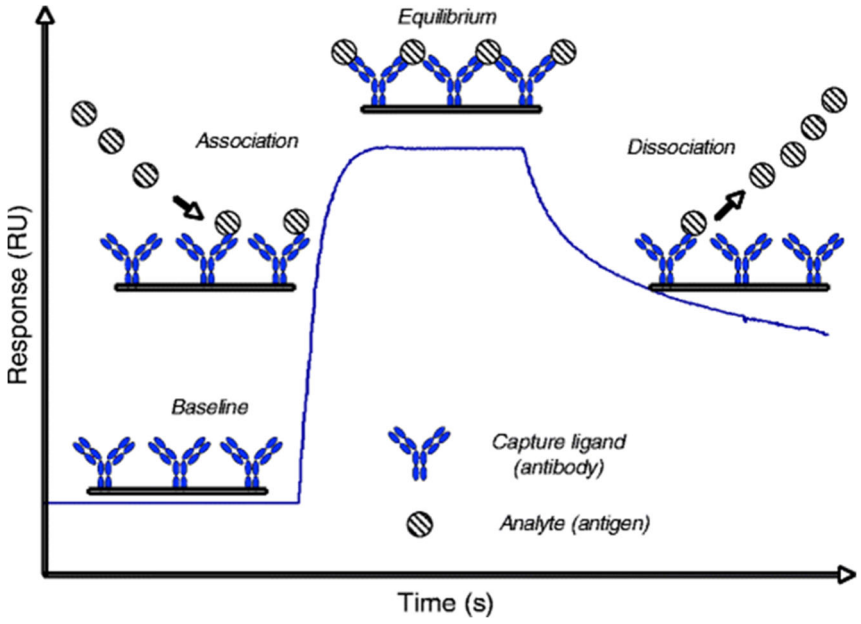

Figure 1.8. Diagram of the kinetic regions of an SPR sensorgram that are used for affinity calculations. Reprinted from Reference 93 with permission of Springer.

In SPR biosensing applications, amplification of initial signals is frequently conducted via the binding of additional materials to the initial binding events, as shown in Figure 1.9.[95, 96] Antibodies are a common source of amplification, as they have or can be conjugated to a variety of chemical moieties that can serve as means of amplification, such as biotin, HRP, and their tyrosine residues. The mechanism of amplification is straightforward: the increase in mass at the surface further shifts the binding signal, leading to easier quantification. Further shifts and perturbations in the minimum intensity can arise from optically active materials, such as gold nanoparticles, being used as "signal enhancers". This is based on plasmon-exciton coupling of the optically active material to the surface plasmon states. The coupling radically alters the dispersion curve of the incident radiation, an effect known as "back-bending".[97] As a result, gold nanoparticles are a common means of signal enhancement.[98-102]

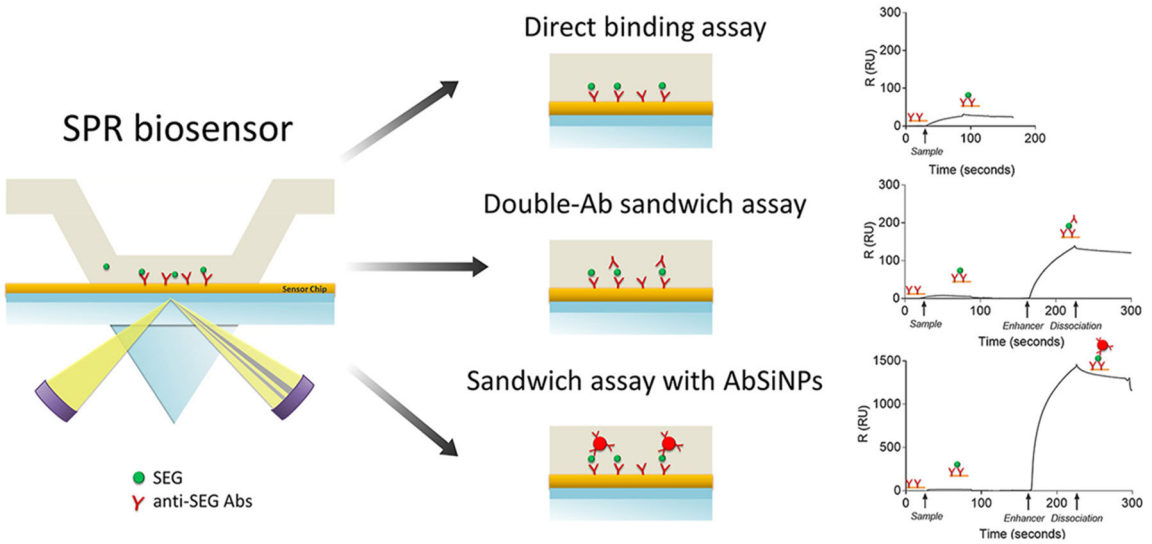

Figure 1.9. Illustration of mass-based SPR binding signal amplification. Reprinted from Reference 96 with permission of Elsevier.

1.5.2 Biomimetic Lipid Bilayers

The surface-based analysis of SPR is also synergistic with the implementation of biomimetic configurations such as supported lipid bilayers (SLBs), shown in Figure 1.10. SLBs are an increasingly popular means of generating an analysis surface and form the basis of a wide variety of bioanalysis in the current analytical literature.[103-105] Lipid bilayers form a fundamental component of cell biology, as they separate the exterior of the cell from the interior, while also playing host to a wide range of proteins, glycans, and lipids that participate in many central biological functions, such as ion-gating, cell-to-cell communication, adhesion, and immune response.[106-109] Lipids of a desired composition are mixed and extruded into vesicles for deposition onto the surface interface. The vesicle then unfurls and fuses to the surface, though this process can be controlled by vesicle composition. Most commonly, a "matrix" lipid such as palmitoyl-2-oleoyl-glycero-3-phosphocholine (POPC) or dioleoyl-sn-glycero-3-phosphoethanolamine (DOPE) is the primary constituent, and 0.1-5% are other lipids. A benefit of this methodology is its flexibility, as different lipid components can be incorporated into the vesicle that impart both functionality and biological specificity. For example, a head group of nitriloacetic acid (NTA) is frequently used with a dioleoyl-sn-glycero-succinyl lipid and complexed with Ni^{2+} or Co^{2+} ion (e.g., Ni:NTA-DGS). This lipid headgroup binds strongly to polyhistidine tags that are frequently expressed at the end of recombinant proteins as a means of pulldown in the purification steps of the protein production. Recombinant proteins can thus be immobilized to the membrane surface, mimicking the cell surface environment. Towards biological specificity, a wide range of tissue-specific lipids and

membrane components can easily be incorporated, such as glycolipids like gangliosides and sphingomyelin, sterol lipids and cholesterol, and phosphoinositides. SLBs can also serve as a means of anti-fouling in biosensing, as the presented charged outer surface is not subject to the same hydrophobic non-specific binding from biological matrices.[110]

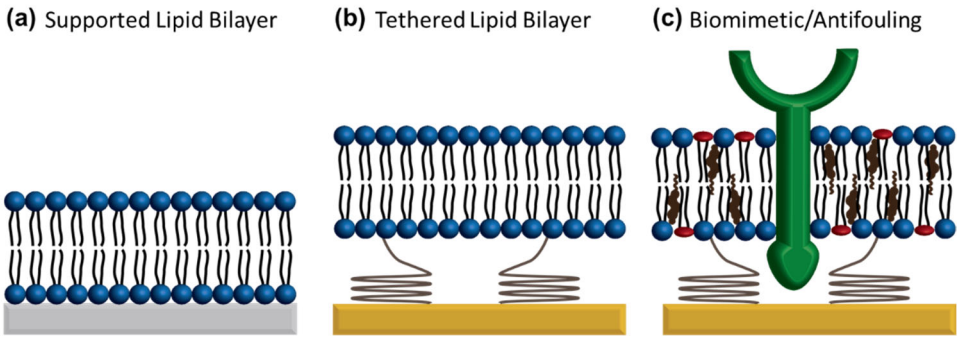

Figure 1.10. Illustration of (a) supported lipid bilayers and (b) tethered lipid bilayers on an SPR or silica surface. (c) A biomimetic lipid bilayer with membrane lipid and protein components. In this form, non-specific proteins cannot reach the surface and adhere to the Au film.

In SPR reports, while lipid bilayers are a common means of both anti-fouling and generating biomimetic interfaces, bare Au films are not optimal surfaces for direct immobilization of lipid membranes. This is due to the slight native hydrophobicity of the Au surface, which slightly repels the highly polar head groups of the lipid components. Multiple means are used to overcome this challenge. First, the Au surface can be modified with functional groups amenable to SLB formation. This includes hydrophobic alkyl chains that induce fusion of the vesicle as a monolayer, and so functionally serve as one half of lipid bilayer. Alternatively, thin films (<5 nm) of silicate (SiO_2 or SiO_x) material may be deposited onto the Au surface by either wet or dry deposition techniques as an adhesion

layer. The silica layer is thin enough that it does significantly affect the plasmonic absorption and may even enhance the sensitivity.[111] Additionally, the vesicles themselves can be constructed to include PEG-ylated or thiolated lipids that "tether" the resulting bilayer to the surface, aka a tethered lipid bilayer (TLB). Any affinities generated from these biomimetic interfaces have an advantage over traditional dextran-based surfaces, as has been noted in several recent reports. Additionally, the label-free nature of the SPR analysis is itself more representative of the native states of interactions, as no labels can interfere with binding. Labeled techniques frequently report binding affinities, but the data obtained is limited to the steady-state overall affinity K_d, and cannot obtain the k_a and k_d.

1.6 Integration of SPR with Mass Spectrometry Techniques

While surface plasmon resonance can provide excellent quantification of surface binding events, the binding event, even if strictly specific in its interactions, only reflects the binding moieties themselves, and not greater biological information about the material that binds outside of its refractive index. SPR, along with the other prominent label-free techniques, can thus benefit from a coupling to methodologies that can give qualitative information about the identity of the binding molecules. Mass spectrometry, as such, is a natural fit for this integrated form of analysis, and a number of studies have been published that combine SPR with a variety of mass spec techniques.[112-118] In this mode, SPR can function as a means of pulldown that both gives real-time kinetic information and specific molecular information about the analytes that have been pulled down. However, the surface-based analysis of SPR leads to a practical limitation for coupling to electrospray ionization (ESI)-based techniques, which typically require samples to be in solution phase.

Some work has reported collecting elute from the SPR device for use with ESI,[112] but many more literature reports use the other major mass spec methodology for biomolecules: MALDI-TOF-MS.[113-118]

1.6.1 MALDI-TOF-MS

Laser desorption-ionization as an analytical tool was posited in the late 1960s, but came to prominence in the 1980s, when researchers found that light absorbing matrices aided in the ionization of otherwise non-absorbing analytes. This developed into the technique now known as matrix-assisted laser-desorption ionization mass spectrometry (MALDI-MS). While there are other surface-based methods of mass spectrometry, including desorption electrospray ionization (DESI), laser ablation-inductively coupled plasma ionization (LA-ICP), and direct analysis in real time (DART), MALDI is the most popular for a wide array of bioanalytical and medical applications, such as profiling studies of proteins,[119] lipids[120] and metabolites.[121]

The fundamental mechanism (see Figure 1.11) involves a light-absorbing organic molecule, such as 2,5-dihydroxybenzoic acid (DHB) or α-cyano-4-hydroxycinnamic acid (CHCA), that usually has an aromatic benzene ring that absorbs in the ultraviolet region.[122] The analyte is deposited onto a steel MALDI "plate" surface and dried, followed by deposition of a highly concentrated aqueous mixture of the UV-absorbing molecule. Drying co-crystallizes the "matrix" UV-absorbing molecule with the analyte, and upon irradiation with (usually) a UV CO_2 laser, the matrix crystal both ablates and ionizes the contained analytes.[123] The resulting gas-phase material is then uptaken into the mass

spectrometer, which is, for MALDI-MS, most commonly in the form of time-of-flight (TOF) mass spectrometry.[124]

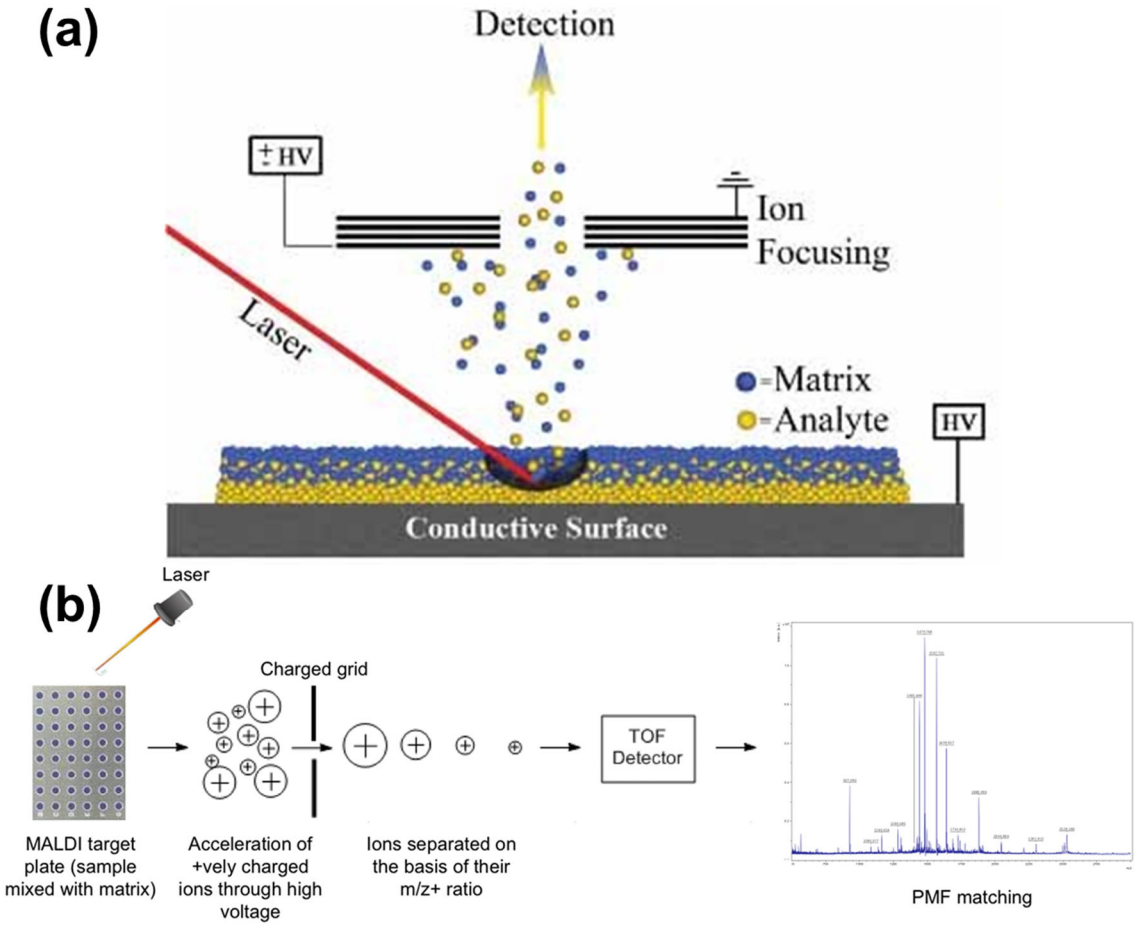

Figure 1.11. Illustration of MALDI operating principle. Reprinted from Reference 123 with permission of Wiley. (b) Full MALDI-TOF-MS process. Reprinted from Reference 124.

MALDI-MS is typically known as a "soft" ionization method, where the analyte ionization is indirect and low-intensity enough so as not to fragment the analyte significantly. As a result, ions in MALDI-MS tend to be singly charged or whole molecules, making for simple m/z to mass identifications. An additional limitation of

MALDI as an ionization method is its low efficiency at ionizing large mass biomolecules. This is partially due to the non-linear response of the detection plates in TOF spectrometers. Impact velocity on the detector is inversely proportional to m/z, and increasingly lower velocity impacts (i.e. higher m/z) generate increasingly lower electron counts at the detector.[125] While the technical upper limit of analysis is ~100 kDa, the practical limit for reliable high sensitivity use in most instruments is ~15-20 kDa. Thus, larger proteins are often required as a digestion down to their constituent peptides for MALDI-MS. Profiling of other biomolecules, especially lipids and small-molecule metabolites, which all typically have masses < 3 kDa in their native forms, is not hindered, and MALDI-MS is very commonly used.

1.6.2 Surface-assisted MALDI with Plasmonic Substrates

As an alternative to light-absorbing matrices, there is much development towards solid substrates and nanomaterials that themselves generate ionization in deposited analyte. This can alternatively remove the need for matrix-based preparation, or work in combination with the MALDI matrix to further enhance ionization and resulting analytical signal. Many nanomaterials that either have high photothermal conversion efficiency or high charge-transfer properties or both, such as metals and semiconductors, have been reported as surfaces of ionization for LDI, also known as surface-assisted LDI (SALDI).[126-130] As recently demonstrated,[131, 132] plasmonic materials also appear to participate in assisting ionization. This is not unexpected, as conversion of incident light into thermal radiation with plasmonic nanomaterials is a common application of plasmonic absorption. Au and Ag nanoclusters are used as a means to target and locally heat regions of interest

as a potential treatment for a variety of diseases.[133] In the context of MALDI-MS, the plasmonic conversion of incident radiation on the substrate aids in both the desorption by direct heating and by the excited hot electron bands of the metal aiding in ionization. However, Au's plasmonic absorption of the UV radiation (usually 337 nm) is low-efficiency, so this technique type may be enhanced by the use of a plasmonic metal with higher UV absorption, such as aluminum or indium.

1.7 Three-Dimensional (3D) Printing

The popularity and rising interest in the general culture toward 3D printing technologies has correlated well with its rapid propagation across many fields of academic research. Originating in the late 1980s, 3D printing is a form of additive manufacturing, where an object is built layer-by-layer and some process fuses the individual layers into a contiguous whole, as opposed to subtractive manufacturing techniques, like etching, that take a block of material and remove pieces until the design is complete. Objects to be built are designed software, though some versions will convert images of real objects into software models first. The models are then converted into universally-recognized .STL files, which are sliced into the individual component layers by the 3D printer software before they are physically printed. Though there are a wide range of materials that can be used for 3D printing, the archetypal use is with plastic and polymer-based components.

The software model-to-completed object process forms one of the fundamental benefits of 3D printing over older methods of lab component creation: ease of manufacture. Hot embossing and injection molding, two standard industrial techniques for plastic parts, are far too costly and inconvenient to set up practically outside of a large-scale purpose-

built facility.[134] The dominant form of small parts manufacture in academic laboratories before 3D printing was soft lithography, the most common form of which involved molding and curing a viscous solution of polydimethylsiloxane (PDMS).[135, 136] PDMS has many upsides, including excellent stability, chemical inertness, and good optical properties, but suffers if modifications are needed to the prototype. A mask or mold is required for the PDMS to be molded to, which must be machined via traditional methods like photolithography, and can be a costly and time-consuming process. 3D printing, on the other hand, requires only a few clicks of the mouse to change the model and reprint. Furthermore, complex internal structures are trivial to make in 3D printing that would be nearly impossible to the average user using previous methods. This ease of manufacture leads to so-called "rapid prototyping", one of the most useful aspects of 3D printing, which allows a user to quickly optimize the component for their purposes.[137] PDMS still has several advantages over to 3D printing; most crucially, the resolution and subsequent component feature size that can be manufactured via a PDMS mask is much smaller (nanometer scale) than can be achieved with most current 3D printers (micrometer scale).[138] However, with the level of interest in 3D printing, improvements to the technologies are likely to equal or surpass the capabilities of PDMS-based soft lithography.

The term 3D printing actually refers to a suite of additive manufacturing techniques that all share the same core steps from software-design to automatic layer-by-layer construction. The complexity and sophistication of current techniques has also expanded as key patents on two major technologies (stereolithography and fused deposition modeling) have expired in recent years.[139] The work in the proceeding chapters is focused

around a single technique, stereolithography, but the other deserve mention as a contrast. Fused deposition modeling (FDM) is a popular, less-expensive technique, where the desired material, initially in the form of a long filament, is pulled through a heated nozzle onto the working surface, where it binds with the previous lower layer in a semi-liquid form.[140] The bonding between layers is fundamentally weaker for FDM than SLA because there is no chemical polymerization reaction to bond the layers, but FDM as a consequence can use a wider range of materials,[141] and has been reported for a wide range of analytical methods.[142-147] Inkjet printing is another form of 3D printing still in the early stages of development, wherein the preexisting mechanical structure of ink printers is adapted to trace the active layer of fabrication.[148] Inkjet printing, in both a powder-based and ink-based form been reported for a number of analytical applications,[149-152] and while the resulting parts are relatively low strength compared to SLA and FDM,[153] inkjet printing is well-suited to dense microfluidic constructions.

1.7.1 Stereolithography

The most prominent current form of 3D printing as implemented in academic research is stereolithography (SLA). The working principle begins with a working surface submerged in a reservoir of photocurable resin. A movable laser then polymerizes the resin at the working surface into a solid form; the stage is moved, and the process repeats. Each 2D layer solidifies and melds into the previous layer, creating a continuous solid object. There are two primary physical configurations for SLA. The free surface, or bath, configuration, places the working surface at the top of the bath, and the stage is lowered for each successive layer.[154] The inverted “bat” configuration, or constrained surface

configuration, as shown in Figure 1.12. instead places the working surface at the bottom of the reservoir over a transparent window.[155] The stage is raised with each layer, lessening the height restrictions and limiting the oxygen inhibition of the polymerization reaction because the working surface is submerged, significantly speeding up the curing time. Another advancement, CLIP, makes the bottom window oxygen permeable so that the lowest layer of the resin is oxygen-inhibited, preventing adhesion of the still-forming object to the window. Many alternate forms of SLA are used in the literature, including 2 photon polymerization (2PP), a high resolution version where a femtosecond laser sends ultrafast pulses that initiate two-photon absorption and polymerization on a very precisely targeted small volume of the photopolymer,[156] and digital light processing stereolithography (SLA-DLP), where, a digital micromirror is used as the laser source projector, which can simultaneously shine on and polymerize the entire working fabrication surface at once instead of scanning with a single source, significantly increasing build speed.[157]

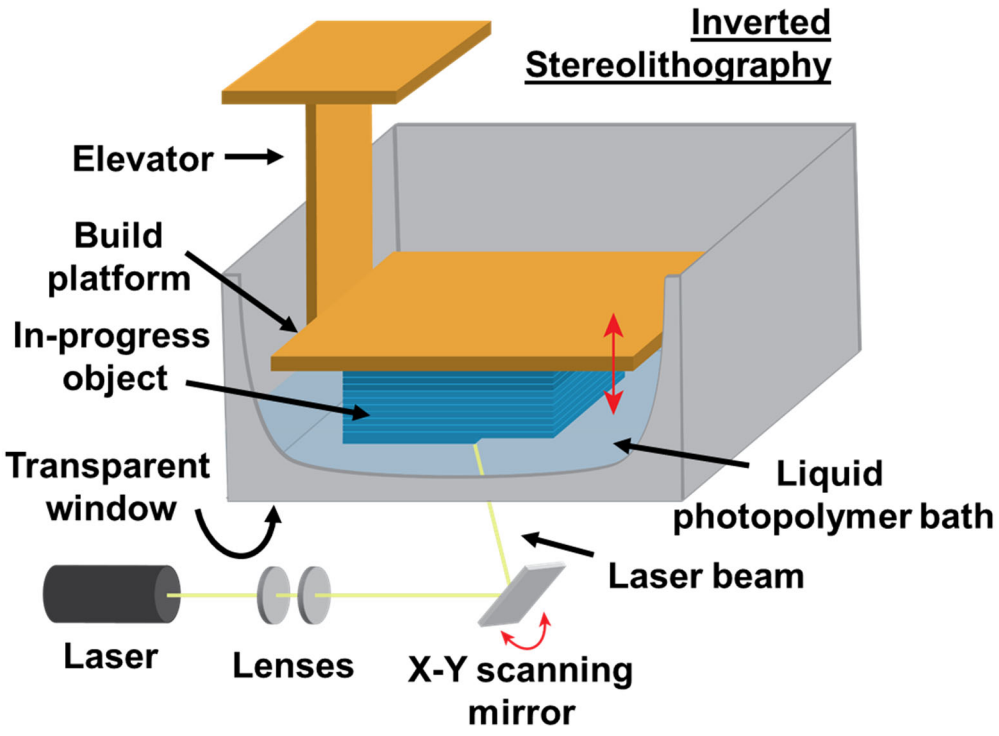

Figure 1.12. Diagram of inverted bath stereolithography, the most common form in commercial instrumentation.

1.7.2 Analytical applications of 3D printing

The customization and rapid prototyping capability of 3D printing have made it highly appealing for use in academic research, where development of new methodologies and analyses are a constant. A core use-case for of 3D printing for analytical purposes is in the manufacture of microfluidic components, as complex internal designs are more facile with the layer-by-layer additive fabrication than with conventional subtractive fabrication. Many printed components have been reported as parts of analytical sensing and bioanalysis, such as preconcentrators,[158-161] complex separation and mixing chambers,[162-166] small-volume sensing channels for optical detection.[167-169] Even simple structures such

as fluidic flowcells for larger-scale devices can be easily designed and molded with PDMS. Structural components can also be created to offer precise and complicated arrangements for conventional optical equipment.[170-174] These pieces indicate the true flexibility and utility of 3D-printing in the lab, as any design can be aided in its implementation by fully customized parts. The focus in successive chapters will be on the implementation of 3D printed optics, so a fuller background is presented here.

1.7.3 3D-printed Optics

Another significant development in the use of 3D printing in labs was the introduction of transparent polymer resins that enable the basic form of optical components to be printed with refractive indices in the range of commercial glass (~1.5-1.6). A number of reports have shown the successful implementation of prisms, lenses, mirrors and waveguides into analytical methodologies.[175-181] A primary benefit of 3D printing in this case is that the optimization of the experimental setup can tilt in more than one direction: the optical configuration can be optimized to the rest of the system rather than the rest of the system having to comport to the available optical components. An additional benefit of the 3D printed optics is that additives can be included in the resin, filament, or ink used that alters the optical properties of the resulting part. Examples in the literature include TiO_2-SiO_2 core-shell nanoparticles to tune the refractive index,[182] and silver[183] and gold[184] nanoparticles to generate plasmonic responses in the final product.

Glass itself would be the ideal material to 3D print for optical components, as it is more structurally and chemically stable than polymers and have higher transmission in the UV and IR regions.[185] However, glass has been one of the more difficult materials to 3D

print, due to the high temperatures needed to soften it enough to work with (>1000 °C) and its quick hardening upon exposure to lower ambient temperatures. As a result, most research until recently has only been able to produce transparent glass for decorative purposes.[186] The quick cooling makes the final product ribbed, and so not suitable for optical measurements. Much research is ongoing that seeks to create hybrid methods that can reliably produce glass with automated additive manufacturing of 3D printing, especially the inclusion of silica particles in the resin or ink, followed by part manufacture then decoupling the resin or ink from the silica via a high-temperature sintering step, leaving the fused silica object. For now and the near future, the most effective means of 3D printing optics is still transparent polymers.

1.8 Aims and Scope of Dissertation

The aims of this dissertation are to develop and improve the underlying technological diversity of SPR based techniques for bioanalysis and biosensing. This will primarily be conducted by the addition of new techniques and materials to the core SPR functionality, especially MALDI-MS, 3D printing, and aluminum thin films. These techniques and materials have been described in the preceding sections, along with their applicability to SPR spectroscopy and how they may solve various pitfalls in current SPR application development. Each succeeding chapter will address the use of these new additions, along with the methodological adaptions required to incorporate them into SPR analyses. The overall scope is the diversification of SPR applications; As more and more optical and biological technologies operate at the nanoscale, there is a strong need for

exploring new aspects of photonic-plasmonic interactions at the basic knowledge level, so that new technologies can be effectively developed.

Chapter 2 begins with a study of the integration of SPR imaging with MALDI-MS for detection of environmental pathogens. The coupling of the techniques was achieved with a silicated gold microarray substrate previously used for both SPR imaging and MALDI separately but had not yet been combined into an integrated package. A novel surface immobilization scheme utilized self-assembled monolayers of fluorinated hydrocarbons and a natural ganglioside sensing moiety to quantitatively pull down cholera toxin, followed by a tryptic digestion and MALDI analysis on the same chip to analyze and identify the protein-specific peptide profile. This method was additionally able to identify the presence of CT even in a complex biological matrix at environmentally relevant levels. This work serves as a starting point for the further implementation of array-based coupling of SPR and MALDI-MS.

Chapter 3 expands on previous work with 3D printing and plasmonic analysis to incorporate a hybridized 3D printing-PDMS molding process to the optical components used for SPR analysis. A challenge to 3D printing for optical components is the technological level of 3D printing is far from the high-quality surface roughness requirements for spectroscopy. This has previously been overcome by traditional means such as polishing, but this report details an alternative means of fabrication that sidesteps the issue almost entirely. PDMS molds of the printed part or other smooth surface were made, followed by spin-coat smoothing and pouring of photocurable resin into the molds to make high-quality prisms. The optical performance of the final prisms in SPR

configurations was almost identical to the much more expensive glass prisms, and this method allows geometrical flexibility inherent in 3D to be maintained in polymer prisms.

Chapter 4 shifts the focus of development from new technologies to new materials, namely plasmonic aluminum thin films in place of traditional gold films. Basic information of the analytical merits of Al films was lacking in the literature and investigated here. Films were predicted and fabricated, and spectral characteristics were found to match predictions well, and several key unexpected traits were found. First, while Al films were approximately equal to Au films in angle-tracking sensitivity, Al was substantially more sensitive in the SPR imaging mode than Au. Interestingly, aluminum films were also found to be significantly more antifouling than Au films. Finally, the Al films were found to be very stable over the lifetime of experiments, in contrast to previous assumptions about their chemical stability and usability.

Chapter 5 builds on the work from the previous chapter with an emphasis on the bioanalytical applications of plasmonic aluminum thin films. Chemical reactions at the aluminum and aluminum oxide surface were investigated, starting with phosphate-oxide interactions for enrichment of phosphorylated proteins from biological digests. Furthermore, functionalization of Al_2O_3 layer was accomplished with a silane-conjugated sensing moiety for sensing of bacterial proteins. Additionally, physical modifications of the Al surface with ionic polymers were compared with the bare surface for qualitatively comparing pulldown of charge lipid vesicles. The physical modifications were then used in tandem with the high sensitivity SPR imaging mode to analyze biophysical binding dynamics of charged peptide biomarkers with the charged polymers across a full

microarray simultaneously, both in standard buffer and in a more complex biological matrix. Each type of analysis points towards a broad potential of applications going forward for plasmonic Al thin films. These further applications also form the basis of discussion in Chapter 6, where active and ongoing research on each of the primary subject areas (SPR-MALDI, plasmonic 3D printing, Al thin-film SPR) are detailed and discussed in regard to their future potential.

1.9 References

1. Su, L. A.; Jia, W. Z.; Hou, C. J.; Lei, Y., Microbial biosensors: A review. *Biosens. Bioelectron.* **2011,** *26* (5), 1788-1799.

2. Xu, X.; Ying, Y. B., Microbial Biosensors for Environmental Monitoring and Food Analysis. *FOOD REVIEWS INTERNATIONAL* **2011,** *27* (3), 300-329.

3. Mohankumar, P.; Ajayan, J.; Mohanraj, T.; Yasodharan, R., Recent developments in biosensors for healthcare and biomedical applications: A review. *MEASUREMENT* **2021,** *167*.

4. Pohanka, M.; Skladal, P.; Kroea, M., Biosensors for biological warfare agent detection. *DEFENCE SCIENCE JOURNAL* **2007,** *57* (3), 185-193.

5. Scognarniglio, V.; Arduini, F.; Palleschi, G.; Rea, G., Biosensing technology for sustainable food safety. *TRAC-TRENDS IN ANALYTICAL CHEMISTRY* **2014,** *62*, 1-10.

6. Naresh, V.; Lee, N., A Review on Biosensors and Recent Development of Nanostructured Materials-Enabled Biosensors. *SENSORS* **2021,** *21* (4).

7. Chambers, J. P.; Arulanandam, B. P.; Matta, L. L.; Weis, A.; Valdes, J. J., Biosensor recognition elements. *CURRENT ISSUES IN MOLECULAR BIOLOGY* **2008,** *10*, 1-12.

8. Bahadir, E. B.; Sezginturk, M. K., Applications of commercial biosensors in clinical, food, environmental, and biothreat/biowarfare analyses. *ANALYTICAL BIOCHEMISTRY* **2015,** *478*, 107-120.

9. Catimel, B.; Rothacker, J.; Catimel, J.; Faux, M.; Ross, J.; Connolly, L.; Clippingdale, A.; Burgess, A. W.; Nice, E., Biosensor-based micro-affinity purification for the proteomic analysis of protein complexes. *JOURNAL OF PROTEOME RESEARCH* **2005,** *4* (5), 1646-1656.

10. Nelson, R. W.; Nedelkov, D.; Tubbs, K. A., Biosensor chip mass spectrometry: A chip-based proteomics approach. *ELECTROPHORESIS* **2000,** *21* (6), 1155-1163.

11. Yuk, J. S.; Ha, K. S., Proteomic applications of surface plasmon resonance biosensors: analysis of protein arrays. *EXPERIMENTAL AND MOLECULAR MEDICINE* **2005,** *37* (1), 1-10.

12. Zhang, S. X.; Greening, D. W.; Hong, Y. N., Recent advances in bioanalytical methods to measure proteome stability in cells. *ANALYST* **2021,** *146* (7), 2097-2109.

13. Lertvachirapaiboon, C.; Supunyabut, C.; Baba, A.; Ekgasit, S.; Thammacharoen, C.; Shinbo, K.; Kato, K.; Kaneko, F., Transmission Surface Plasmon Resonance Signal Enhancement via Growth of Gold Nanoparticles on a Gold Grating Surface. *Plasmonics* **2013,** *8* (2), 369-375.

14. Roh, S.; Chung, T.; Lee, B., Overview of the Characteristics of Micro- and Nano-Structured Surface Plasmon Resonance Sensors. *SENSORS* **2011,** *11* (2), 1565-1588.

15. Eftekhari, F.; Escobedo, C.; Ferreira, J.; Duan, X. B.; Girotto, E. M.; Brolo, A. G.; Gordon, R.; Sinton, D., Nanoholes As Nanochannels: Flow-through Plasmonic Sensing. *Anal. Chem.* **2009,** *81* (11), 4308-4311.

16. Bantz, K. C.; Meyer, A. F.; Wittenberg, N. J.; Im, H.; Kurtulus, O.; Lee, S. H.; Lindquist, N. C.; Oh, S. H.; Haynes, C. L., Recent progress in SERS biosensing. *Phys. Chem. Chem. Phys.* **2011,** *13* (24), 11551-11567.

17. Bauch, M.; Toma, K.; Toma, M.; Zhang, Q. W.; Dostalek, J., Plasmon-Enhanced Fluorescence Biosensors: a Review. *Plasmonics* **2014,** *9* (4), 781-799.

18. Coe, J. V.; Heer, J. M.; Teeters-Kennedy, S.; Tian, H.; Rodriguez, K. R., Extraordinary transmission of metal films with arrays of subwavelength holes. *ANNUAL REVIEW OF PHYSICAL CHEMISTRY* **2008,** *59*, 179-202.

19. Born, M. A. X.; Wolf, E., CHAPTER III - FOUNDATIONS OF GEOMETRICAL OPTICS. In *Principles of Optics (Sixth Edition)*, Born, M. A. X.; Wolf, E., Eds. Pergamon: 1980; pp 109-132.

20. Nilsson, D.-E., From cornea to retinal image in invertebrate eyes. *Trends in neurosciences* **1990,** *13* (2), 55-64.

21. Sapsford, K. E., Total-internal-reflection platforms for chemical and biological sensing applications. In *Optical guided-wave chemical and biosensors I*, Springer: 2010; pp 3-20.

22. Pospisilova, M.; Kuncova, G.; Trogl, J., Fiber-Optic Chemical Sensors and Fiber-Optic Bio-Sensors. *SENSORS* **2015,** *15* (10), 25208-25259.

23. Ritchie, R. H., PLASMA LOSSES BY FAST ELECTRONS IN THIN FILMS. *PHYSICAL REVIEW* **1957,** *106* (5), 874-881.

24. Powell, C. J.; Swan, J. B., ORIGIN OF THE CHARACTERISTIC ELECTRON ENERGY LOSSES IN ALUMINUM. *PHYSICAL REVIEW* **1959,** *115* (4), 869-875.

25. Kurihara, K.; Suzuki, K., Theoretical understanding of an absorption-based surface plasmon resonance sensor based on Kretchmann's theory. *Anal. Chem.* **2002,** *74* (3), 696-701.

26. Rakić, A. D., Algorithm for the determination of intrinsic optical constants of metal films: application to aluminum. *Appl. Opt.* **1995,** *34* (22), 4755-4767.

27. Raether, H., SURFACE-PLASMONS ON SMOOTH AND ROUGH SURFACES AND ON GRATINGS. *SPRINGER TRACTS IN MODERN PHYSICS* **1988,** *111*, 1-133.

28. Kretschm.E; Raether, H., RADIATIVE DECAY OF NON RADIATIVE SURFACE PLASMONS EXCITED BY LIGHT. *ZEITSCHRIFT FUR NATURFORSCHUNG PART A-ASTROPHYSIK PHYSIK UND PHYSIKALISCHE CHEMIE* **1968,** *A 23* (12), 2135-&.

29. Otto, A., Excitation of nonradiative surface plasma waves in silver by the method of frustrated total reflection. *Zeitschrift für Physik A Hadrons and nuclei* **1968,** *216* (4), 398-410.

30. Wu, L. M.; Jia, Y.; Jiang, L. Y.; Guo, J.; Dai, X. Y.; Xiang, Y. J.; Fan, D. Y., Sensitivity Improved SPR Biosensor Based on the MoS2/Graphene-Aluminum Hybrid Structure. *JOURNAL OF LIGHTWAVE TECHNOLOGY* **2017,** *35* (1), 82-87.

31. Wang, J. C.; Song, C.; Hang, J.; Hu, Z. D.; Zhang, F., Tunable Fano resonance based on grating-coupled and graphene-based Otto configuration. *Opt. Express* **2017,** *25* (20), 23880-23892.

32. Akowuah, E. K.; Gorman, T.; Haxha, S., Design and optimization of a novel surface plasmon resonance biosensor based on Otto configuration. *Opt. Express* **2009,** *17* (26), 23511-23521.

33. Zhao, Y.; Tong, R. J.; Xia, F.; Peng, Y., Current status of optical fiber biosensor based on surface plasmon resonance. *Biosens. Bioelectron.* **2019,** *142*.

34. Sepulveda, B.; Angelome, P. C.; Lechuga, L. M.; Liz-Marzan, L. M., LSPR-based nanobiosensors. *Nano Today* **2009,** *4* (3), 244-251.

35. Linman, M. J.; Cheng, Q. J., Surface Plasmon Resonance: New Biointerface Designs and High-Throughput Affinity Screening. In *Optical Guided-wave Chemical and Biosensors I*, Zourob, M.; Lakhtakia, A., Eds. Springer Berlin Heidelberg: Berlin, Heidelberg, 2009; pp 133-153.

36. McMeekin, T. L.; Groves, M. L.; Hipp, N. J., Refractive Indices of Amino Acids, Proteins, and Related Substances. In *Amino Acids and Serum Proteins*, AMERICAN CHEMICAL SOCIETY: 1964; Vol. 44, pp 54-66.

37. Schasfoort, R. B. M., *Introduction to Surface Plasmon Resonance*. 2017; p 1-26.

38. Altug, H.; Oh, S. H.; Maier, S. A.; Homola, J., Advances and applications of nanophotonic biosensors. *NATURE NANOTECHNOLOGY* **2022,** *17* (1), 5-16.

39. Shumaker-Parry, J. S.; Campbell, C. T., Quantitative methods for spatially resolved adsorption/desorption measurements in real time by surface plasmon resonance microscopy. *Anal. Chem.* **2004,** *76* (4), 907-917.

40. Zhu, L.; Wang, K.; Cui, J.; Liu, H.; Bu, X. L.; Ma, H. L.; Wang, W. Z.; Gong, H.; Lausted, C.; Hood, L.; Yang, G.; Hu, Z. Y., Label-Free Quantitative Detection of Tumor-Derived Exosomes through Surface Plasmon Resonance Imaging. *Anal. Chem.* **2014,** *86* (17), 8857-8864.

41. Jung, L. S.; Campbell, C. T.; Chinowsky, T. M.; Mar, M. N.; Yee, S. S., Quantitative interpretation of the response of surface plasmon resonance sensors to adsorbed films. *LANGMUIR* **1998,** *14* (19), 5636-5648.

42. Scarano, S.; Mascini, M.; Turner, A. P. F.; Minunni, M., Surface plasmon resonance imaging for affinity-based biosensors. *Biosens. Bioelectron.* **2010,** *25* (5), 957-966.

43. Steiner, G., Surface plasmon resonance imaging. *ANALYTICAL AND BIOANALYTICAL CHEMISTRY* **2004,** *379* (3), 328-331.

44. Malinick, A. S.; Lambert, A. S.; Stuart, D. D.; Li, B.; Puente, E.; Cheng, Q., Detection of Multiple Sclerosis Biomarkers in Serum by Ganglioside Microarrays and Surface Plasmon Resonance Imaging. *ACS Sensors* **2020**, Submitted.

45. Yuk, J. S.; Kim, H. S.; Jung, J. W.; Jung, S. H.; Lee, S. J.; Kim, W. J.; Han, J. A.; Kim, Y. M.; Ha, K. S., Analysis of protein interactions on protein arrays by a novel spectral surface plasmon resonance imaging. *Biosens. Bioelectron.* **2006,** *21* (8), 1521-1528.

46. Houngkamhang, N.; Vongsakulyanon, A.; Peungthum, P.; Sudprasert, K.; Kitpoka, P.; Kunakorn, M.; Sutapun, B.; Amarit, R.; Somboonkaew, A.; Srikhirin, T., ABO Blood-Typing Using an Antibody Array Technique Based on Surface Plasmon Resonance Imaging. *SENSORS* **2013,** *13* (9), 11913-11922.

47. Suraniti, E.; Sollier, E.; Calemczuk, R.; Livache, T.; Marche, P. N.; Villiers, M. B.; Roupioz, Y., Real-time detection of lymphocytes binding on an antibody chip using SPR imaging. *LAB ON A CHIP* **2007,** *7* (9), 1206-1208.

48. Beusink, J. B.; Lokate, A. M. C.; Besselink, G. A. J.; Pruijn, G. J. M.; Schasfoort, R. B. M., Angle-scanning SPR imaging for detection of biomolecular interactions on microarrays. *Biosens. Bioelectron.* **2008,** *23* (6), 839-844.

49. Wood, J. B.; Szyndler, M. W.; Halpern, A. R.; Cho, K.; Corn, R. M., Fabrication of DNA Microarrays on Polydopamine-Modified Gold Thin Films for SPR Imaging Measurements. *LANGMUIR* **2013,** *29* (34), 10868-10873.

50. Jordan, C. E.; Frutos, A. G.; Thiel, A. J.; Corn, R. M., Surface plasmon resonance imaging measurements of DNA hybridization adsorption and streptavidin/DNA multilayer formation at chemically modified gold surfaces. *Anal. Chem.* **1997,** *69* (24), 4939-4947.

51. Zhou, X. L.; Yang, Y. Z.; Wang, S. P.; Liu, X. W., Surface Plasmon Resonance Microscopy: From Single-Molecule Sensing to Single-Cell Imaging. *Angew. Chem.-Int. Edit.* **2020,** *59* (5), 1776-1785.

52. Peterson, A. W.; Halter, M.; Tona, A.; Plant, A. L., High resolution surface plasmon resonance imaging for single cells. *BMC CELL BIOLOGY* **2014,** *15*.

53. Zhang, P. F.; Ma, G. Z.; Dong, W.; Wan, Z. J.; Wang, S. P.; Tao, N. J., Plasmonic scattering imaging of single proteins and binding kinetics. *NATURE METHODS* **2020,** *17* (10), 1010-+.

54. Malinick, A. S.; Stuart, D. D.; Lambert, A. S.; Cheng, Q., Surface plasmon resonance imaging (SPRi) in combination with machine learning for microarray analysis of multiple sclerosis biomarkers in whole serum. *Biosensors and Bioelectronics: X* **2022,** *10*, 100127.

55. Strobbia, P.; Languirand, E.; Cullum, B. M., Recent advances in plasmonic nanostructures for sensing: a review. *Opt. Eng.* **2015,** *54* (10), 21.

56. Yang, Z. T.; Wang, J. Y.; Shao, Y. B.; Jin, Y. L.; Yi, M., Studying corrosion of silver thin film by surface plasmon resonance technique. *OPTICAL AND QUANTUM ELECTRONICS* **2020,** *52* (1).

57. West, P. R.; Ishii, S.; Naik, G. V.; Emani, N. K.; Shalaev, V. M.; Boltasseva, A., Searching for better plasmonic materials. *Laser Photon. Rev.* **2010,** *4* (6), 795-808.

58. Johnson, P. B.; Christy, R. W., Optical Constants of the Noble Metals. *Physical Review B* **1972,** *6* (12), 4370-4379.

59. Beversluis, M. R.; Bouhelier, A.; Novotny, L., Continuum generation from single gold nanostructures through near-field mediated intraband transitions. *PHYSICAL REVIEW B* **2003,** *68* (11).

60. Ehrenreich, H.; Philipp, H. R.; Segall, B., OPTICAL PROPERTIES OF ALUMINUM. *PHYSICAL REVIEW* **1963,** *132* (5), 1918-&.

61. Hinman, S. S.; McKeating, K. S.; Cheng, Q., Surface Plasmon Resonance: Material and Interface Design for Universal Accessibility. *Anal. Chem.* **2018,** *90* (1), 19-39.

62. Joshi, S.; Pellacani, P.; van Beek, T. A.; Zuilhof, H.; Nielen, M. W. F., Surface characterization and antifouling properties of nanostructured gold chips for imaging surface plasmon resonance biosensing. *SENSORS AND ACTUATORS B-CHEMICAL* **2015,** *209*, 505-514.

63. Rodriguez-Emmenegger, C.; Brynda, E.; Riedel, T.; Houska, M.; Subr, V.; Alles, A. B.; Hasan, E.; Gautrot, J. E.; Huck, W. T. S., Polymer Brushes Showing Non-Fouling in Blood Plasma Challenge the Currently Accepted Design of Protein Resistant Surfaces. *MACROMOLECULAR RAPID COMMUNICATIONS* **2011,** *32* (13), 952-957.

64. D'Agata, R.; Bellassai, N.; Jungbluth, V.; Spoto, G., Recent Advances in Antifouling Materials for Surface Plasmon Resonance Biosensing in Clinical Diagnostics and Food Safety. *POLYMERS* **2021,** *13* (12).

65. Ye, H. J.; Wang, L. B.; Huang, R. L.; Su, R. X.; Liu, B. S.; Qi, W.; He, Z. M., Superior Antifouling Performance of a Zwitterionic Peptide Compared to an Amphiphilic, Non-Ionic Peptide. *ACS APPLIED MATERIALS & INTERFACES* **2015,** *7* (40), 22448-22457.

66. Cooper, B. R.; Ehrenreich, H.; Philipp, H. R., Optical Properties of Noble Metals. II. *Physical Review* **1965,** *138* (2A), A494-A507.

67. Gerard, D.; Gray, S. K., Aluminium plasmonics. *J. Phys. D-Appl. Phys.* **2015,** *48* (18), 14.

68. Gonzalez-Campuzano, R.; Saniger, J. M.; Mendoza, D., Plasmonic resonances in hybrid systems of aluminum nanostructured arrays and few layer graphene within the UV-IR spectral range. *Nanotechnology* **2017,** *28* (46), 9.

69. Filmetrics Refractive Index Database. http://www.filmetrics.com/refractiveindex-database (accessed December).

70. Tanabe, I.; Tanaka, Y. Y.; Watari, K.; Hanulia, T.; Goto, T.; Inami, W.; Kawata, Y.; Ozaki, Y., Far- and deep-ultraviolet surface plasmon resonance sensors working in aqueous solutions using aluminum thin films. *Sci Rep* **2017,** *7*, 7.

71. Tanabe, I.; Tanaka, Y. Y.; Watari, K.; Hanulia, T.; Goto, T.; Inami, W.; Kawata, Y.; Ozaki, Y., Aluminum Film Thickness Dependence of Surface Plasmon Resonance in the Far- and Deep-ultraviolet Regions. *Chem. Lett.* **2017,** *46* (10), 1560-1563.

72. Peterlinz, K. A.; Georgiadis, R., Two-color approach for determination of thickness and dielectric constant of thin films using surface plasmon resonance spectroscopy. *OPTICS COMMUNICATIONS* **1996,** *130* (4-6), 260-266.

73. Peterlinz, K. A.; Georgiadis, R. M.; Herne, T. M.; Tarlov, M. J., Observation of hybridization and dehybridization of thiol-tethered DNA using two-color surface plasmon resonance spectroscopy. *JOURNAL OF THE AMERICAN CHEMICAL SOCIETY* **1997,** *119* (14), 3401-3402.

74. Chinowsky, T. M.; Yee, S. S., Quantifying the information content of surface plasmon resonance reflection spectra. *SENSORS AND ACTUATORS B-CHEMICAL* **1998,** *51* (1-3), 321-330.

75. Homola, J.; Lu, H. B.; Yee, S. S., Dual-channel surface plasmon resonance sensor with spectral discrimination of sensing channels using dielectric overlayer. *ELECTRONICS LETTERS* **1999,** *35* (13), 1105-1106.

76. Guo, J.; Keathley, P. D.; Hastings, J. T., Dual-mode surface-plasmon-resonance sensors using angular interrogation. *OPTICS LETTERS* **2008,** *33* (5), 512-514.

77. Lee, K. L.; You, M. L.; Wei, P. K., Aluminum Nanostructures for Surface-Plasmon-Resonance-Based Sensing Applications. *ACS APPLIED NANO MATERIALS* **2019,** *2* (4), 1930-1939.

78. Suzuki, A.; Kondoh, J.; Matsui, Y.; Shiokawa, S.; Suzuki, K., Development of novel optical waveguide surface plasmon resonance (SPR) sensor with dual light emitting diodes. *SENSORS AND ACTUATORS B-CHEMICAL* **2005,** *106* (1), 383-387.

79. Zeng, Y. J.; Zhou, J.; Sang, W.; Kong, W. F.; Qu, J. L.; Ho, H. P.; Zhou, K. M.; Gao, B. Z.; Chen, J. J.; Shao, Y. H., High-Sensitive Surface Plasmon Resonance Imaging Biosensor Based on Dual-Wavelength Differential Method. *FRONTIERS IN CHEMISTRY* **2021,** *9*.

80. Parkkila, P.; Elderdfi, M.; Bunker, A.; Viitala, T., Biophysical Characterization of Supported Lipid Bilayers Using Parallel Dual-Wavelength Surface Plasmon Resonance and Quartz Crystal Microbalance Measurements. *Langmuir* **2018,** *34* (27), 8081-8091.

81. Knight, M. W.; Liu, L. F.; Wang, Y. M.; Brown, L.; Mukherjee, S.; King, N. S.; Everitt, H. O.; Nordlander, P.; Halas, N. J., Aluminum Plasmonic Nanoantennas. *Nano Lett.* **2012,** *12* (11), 6000-6004.

82. Liang, Y. Z.; Cui, W. L.; Li, L. X.; Yu, Z. Y.; Peng, W.; Xu, T., Large-Scale Plasmonic Nanodisk Structures for a High Sensitivity Biosensing Platform Fabricated by Transfer Nanoprinting. *Adv. Opt. Mater.* **2019,** *7* (7).

83. Li, W. B.; Zhang, L.; Zhou, J. H.; Wu, H. K., Well-designed metal nanostructured arrays for label-free plasmonic biosensing. *JOURNAL OF MATERIALS CHEMISTRY C* **2015,** *3* (25), 6479-6492.

84. Li, X. M.; Bi, M. H.; Cui, L.; Zhou, Y. Z.; Du, X. W.; Qiao, S. Z.; Yang, J., 3D Aluminum Hybrid Plasmonic Nanostructures with Large Areas of Dense Hot Spots and Long-Term Stability. *ADVANCED FUNCTIONAL MATERIALS* **2017,** *27* (10).

85. Li, Z.; Li, C. H.; Yu, J.; Li, Z. X.; Zhao, X. F.; Liu, A. H.; Jiang, S. Z.; Yang, C.; Zhang, C.; Man, B. Y., Aluminum nanoparticle films with an enhanced hot-spot intensity for high-efficiency SERS. *Opt. Express* **2020,** *28* (7), 9174-9185.

86. Lee, K. L.; Tsai, P. C.; You, M. L.; Pan, M. Y.; Shi, X.; Ueno, K.; Misawa, H.; Wei, P. K., Enhancing Surface Sensitivity of Nanostructure-Based Aluminum Sensors Using Capped Dielectric Layers. *ACS OMEGA* **2017,** *2* (10), 7461-7470.

87. Lay, C. L.; Koh, C. S. L.; Wang, J.; Lee, Y. H.; Jiang, R. B.; Yang, Y. J.; Yang, Z.; Phang, I. Y.; Ling, X. Y., Aluminum nanostructures with strong visible-range SERS activity for versatile micropatterning o molecular security labels. *Nanoscale* **2018,** *10* (2), 575-581.

88. Jha, R.; Sharma, A. K., High-performance sensor based on surface plasmon resonance with chalcogenide prism and aluminum for detection in infrared. *Optics Letters* **2009,** *34* (6), 749-751.

89. Correa, G. C.; Bao, B.; Strandwitz, N. C., Chemical Stability of Titania and Alumina Thin Films Formed by Atomic Layer Deposition. *Acs Applied Materials & Interfaces* **2015,** *7* (27), 14816-14821.

90. Langhammer, C.; Schwind, M.; Kasemo, B.; Zoric, I., Localized surface plasmon resonances in aluminum nanodisks. *Nano Lett.* **2008,** *8* (5), 1461-1471.

91. Masson, J. F., Surface Plasmon Resonance Clinical Biosensors for Medical Diagnostics. *ACS SENSORS* **2017,** *2* (1), 16-30.

92. Zhang, P.; Chen, Y. P.; Wang, W.; Shen, Y.; Guo, J. S., Surface plasmon resonance for water pollutant detection and water process analysis. *TRAC-TRENDS IN ANALYTICAL CHEMISTRY* **2016,** *85*, 153-165.

93. Hearty, S.; Leonard, P.; O'Kennedy, R., Measuring Antibody–Antigen Binding Kinetics Using Surface Plasmon Resonance. In *Antibody Engineering: Methods and Protocols, Second Edition*, Chames, P., Ed. Humana Press: Totowa, NJ, 2012; pp 411-442.

94. Homola, J., Present and future of surface plasmon resonance biosensors. *ANALYTICAL AND BIOANALYTICAL CHEMISTRY* **2003,** *377* (3), 528-539.

95. Nguyen, H. H.; Park, J.; Kang, S.; Kim, M., Surface Plasmon Resonance: A Versatile Technique for Biosensor Applications. *SENSORS* **2015,** *15* (5), 10481-10510.

96. Belen, S. M.; Sofia, N. T.; Romina, M.; Belen, A. M.; Santiago, C.; Julieta, F. L. M.; Pablo, R.; Cristina, V.; Martin, D.; Mauricio, D.; Emilio, M.; Marisa, F., Optimized surface plasmon resonance immunoassay for staphylococcal enterotoxin G detection using silica nanoparticles. *BIOCHEMICAL AND BIOPHYSICAL RESEARCH COMMUNICATIONS* **2021,** *558*, 168-174.

97. Pockrand, I.; Brillante, A.; Mobius, D., EXCITON SURFACE-PLASMON COUPLING - AN EXPERIMENTAL INVESTIGATION. *JOURNAL OF CHEMICAL PHYSICS* **1982,** *77* (12), 6289-6295.

98. Yao, X.; Li, X.; Toledo, F.; Zurita-Lopez, C.; Gutova, M.; Momand, J.; Zhou, F. M., Sub-attomole oligonucleotide and p53 cDNA determinations via a high-resolution surface plasmon resonance combined with oligonucleotide-capped gold nanoparticle signal amplification. *ANALYTICAL BIOCHEMISTRY* **2006,** *354* (2), 220-228.

99. Liu, Y.; Cheng, Q., Detection of Membrane-Binding Proteins by Surface Plasmon Resonance with an All-Aqueous Amplification Scheme. *Anal. Chem.* **2012,** *84* (7), 3179-3186.

100. Hong, L.; Lu, M. D.; Dinel, M. P.; Blain, P.; Peng, W.; Gu, H. Y.; Masson, J. F., Hybridization conditions of oligonucleotide-capped gold nanoparticles for SPR sensing of microRNA. *Biosens. Bioelectron.* **2018,** *109*, 230-236.

101. Yang, Z.; Malinick, A. S.; Yang, T.; Cheng, W.; Cheng, Q., Gold nanoparticle-coupled liposomes for enhanced plasmonic biosensing. *Sensors and Actuators Reports* **2020,** *2* (1), 100023.

102. Wang, Q.; Zou, L. Y.; Yang, X. H.; Liu, X. F.; Nie, W. Y.; Zheng, Y.; Cheng, Q.; Wang, K. M., Direct quantification of cancerous exosomes via surface plasmon resonance with dual gold nanoparticle-assisted signal amplification. *Biosens. Bioelectron.* **2019,** *135*, 129-136.

103. Kiessling, V.; Yang, S. T.; Tamm, L. K., Supported Lipid Bilayers as Models for Studying Membrane Domains. In *LIPID DOMAINS*, Kenworthy, A. K., Ed. 2015; Vol. 75, pp 1-23.

104. Castellana, E. T.; Cremer, P. S., Solid supported lipid bilayers: From biophysical studies to sensor design. *SURFACE SCIENCE REPORTS* **2006,** *61* (10), 429-444.

105. Andersson, J.; Koper, I., Tethered and Polymer Supported Bilayer Lipid Membranes: Structure and Function. *MEMBRANES* **2016,** *6* (2).

106. Schmick, M.; Bastiaens, P. I. H., The Interdependence of Membrane Shape and Cellular Signal Processing. *Cell* **2014,** *156* (6), 1132-1138.

107. Hansen, S. B., Lipid agonism: The PIP2 paradigm of ligand-gated ion channels. *BIOCHIMICA ET BIOPHYSICA ACTA-MOLECULAR AND CELL BIOLOGY OF LIPIDS* **2015,** *1851* (5), 620-628.

108. Szlasa, W.; Zendran, I.; Zalesinska, A.; Tarek, M.; Kulbacka, J., Lipid composition of the cancer cell membrane. *JOURNAL OF BIOENERGETICS AND BIOMEMBRANES* **2020,** *52* (5), 321-342.

109. Robbins, P. D.; Morelli, A. E., Regulation of immune responses by extracellular vesicles. *NATURE REVIEWS IMMUNOLOGY* **2014,** *14* (3), 195-208.

110. McKeating, K. S.; Hinman, S. S.; Rais, N. A.; Zhou, Z.; Cheng, Q., Antifouling Lipid Membranes over Protein A for Orientation Controlled Immunosensing in Undiluted Serum and Plasma. *ACS Sensors* **2019**.

111. Abbas, A.; Linman, M. J.; Cheng, Q. A., Patterned Resonance Plasmonic Microarrays for High-Performance SPR Imaging. *Anal. Chem.* **2011,** *83* (8), 3147-3152.

112. Joshi, S.; Zuilhof, H.; van Beek, T. A.; Nielen, M. W. F., Biochip Spray: Simplified Coupling of Surface Plasmon Resonance Biosensing and Mass Spectrometry. *Anal. Chem.* **2017,** *89* (3), 1427-1432.

113. Kim, Y. E.; Yi, S. Y.; Lee, C. S.; Jung, Y.; Chung, B. H., Gold patterned biochips for on-chip immuno-MALDI-TOF MS: SPR imaging coupled multi-protein MS analysis. *Analyst* **2012,** *137* (2), 386-392.

114. Rouleau, A.; El Osta, M.; Lucchi, G.; Ducoroy, P.; Boireau, W., Immuno-MALDI-MS in Human Plasma and On-Chip Biomarker Characterizations at the Femtomole Level. *Sensors* **2012,** *12* (11), 15119-15132.

115. Musso, J.; Buchmann, W.; Gonnet, F.; Jarroux, N.; Bellon, S.; Frydman, C.; Brunet, D. L.; Daniel, R., Biomarkers probed in saliva by surface plasmon resonance imaging coupled to matrix-assisted laser desorption/ionization mass spectrometry in array format. *ANALYTICAL AND BIOANALYTICAL CHEMISTRY* **2015,** *407* (5), 1285-1294.

116. Forest, S.; Breault-Turcott, J.; Chaurand, P.; Masson, J. F., Surface Plasmon Resonance Imaging-MALDI-TOF Imaging Mass Spectrometry of Thin Tissue Sections. *Anal. Chem.* **2016,** *88* (4), 2072-2079.

117. Anders, U.; Schaefer, J. V.; Hibti, F. E.; Frydman, C.; Suckau, D.; Pluckthun, A.; Zenobi, R., SPRi-MALDI MS: characterization and identification of a kinase from cell lysate by specific interaction with different designed ankyrin repeat proteins. *ANALYTICAL AND BIOANALYTICAL CHEMISTRY* **2017,** *409* (7), 1827-1836.

118. Breault-Turcot, J.; Chaurand, P.; Masson, J. F., Unravelling Nonspecific Adsorption of Complex Protein Mixture on Surfaces with SPR and MS. *Anal. Chem.* **2014,** *86* (19), 9612-9619.

119. Hortin, G. L., The MALDI-TOF mass spectrometric view of the plasma proteome and peptidome. *CLINICAL CHEMISTRY* **2006,** *52* (7), 1223-1237.

120. Zhao, C.; Xie, P. S.; Yong, T.; Wang, H. L.; Chung, A. C. K.; Cai, Z. W., MALDI-MS Imaging Reveals Asymmetric Spatial Distribution of Lipid Metabolites from Bisphenol S-Induced Nephrotoxicity. *Anal. Chem.* **2018,** *90* (5), 3196-3204.

121. Shroff, R.; Rulisek, L.; Doubsky, J.; Svatos, A., Acid-base-driven matrix-assisted mass spectrometry for targeted metabolomics. *PROCEEDINGS OF THE NATIONAL ACADEMY OF SCIENCES OF THE UNITED STATES OF AMERICA* **2009,** *106* (25), 10092-10096.

122. McDonnell, L. A.; Heeren, R. M. A., Imaging mass spectrometry. *MASS SPECTROMETRY REVIEWS* **2007,** *26* (4), 606-643.

123. Watrous, J. D.; Alexandrov, T.; Dorrestein, P. C., The evolving field of imaging mass spectrometry and its impact on future biological research. *JOURNAL OF MASS SPECTROMETRY* **2011,** *46* (2), 209-222.

124. Singhal, N.; Kumar, M.; Kanaujia, P. K.; Virdi, J. S., MALDI-TOF mass spectrometry: an emerging technology for microbial identification and diagnosis. *FRONTIERS IN MICROBIOLOGY* **2015,** *6*.

125. Gilmore, I. S.; Seah, M. P., Ion detection efficiency in SIMS: dependencies on energy, mass and composition for microchannel plates used in mass spectrometry. *INTERNATIONAL JOURNAL OF MASS SPECTROMETRY* **2000,** *202* (1-3), 217-229.

126. Chiang, C. K.; Chiang, N. C.; Lin, Z. H.; Lan, G. Y.; Lin, Y. W.; Chang, H. T., Nanomaterial-Based Surface-Assisted Laser Desorption/Ionization Mass Spectrometry of Peptides and Proteins. *JOURNAL OF THE AMERICAN SOCIETY FOR MASS SPECTROMETRY* **2010,** *21* (7), 1204-1207.

127. Duan, J. C.; Wang, H.; Cheng, Q. A., On-Plate Desalting and SALDI-MS Analysis of Peptides with Hydrophobic Silicate Nanofilms on a Gold Substrate. *Anal. Chem.* **2010,** *82* (22), 9211-9220.

128. Silina, Y. E.; Volmer, D. A., Nanostructured solid substrates for efficient laser desorption/ionization mass spectrometry (LDI-MS) of low molecular weight compounds. *Analyst* **2013,** *138* (23), 7053-7065.

129. Huang, Y. H.; Wang, C. W.; Chen, W. T.; Chen, L. Y.; Chang, H. T., Nanomaterial based mass spectrometry of oligodeoxynucleotide-drug complexes. *ANALYTICAL METHODS* **2015,** *7* (15), 6360-6364.

130. Zhang, Y. H.; Song, Y. Y.; Wu, J.; Li, R. J.; Hu, D.; Lin, Z. A.; Cai, Z. W., A magnetic covalent organic framework as an adsorbent and a new matrix for enrichment and rapid determination of PAHs and their derivatives in PM2.5 by surface-assisted laser desorption/ionization-time of flight-mass spectrometry. *CHEMICAL COMMUNICATIONS* **2019,** *55* (26), 3745-3748.

131. Shanta, P. V.; Li, B.; Stuart, D. D.; Cheng, Q., Plasmonic Gold Templates Enhancing Single Cell Lipidomic Analysis of Microorganisms. *Anal. Chem.* **2020,** *92* (9), 6213-6217.

132. Li, B.; Stuart, D. D.; Shanta, P. V.; Pike, C. D.; Cheng, Q., Probing Herbicide Toxicity to Algae (Selenastrum capricornutum) by Lipid Profiling with Machine Learning and Microchip/MALDI-TOF Mass Spectrometry. *Chemical Research in Toxicology* **2022,** *35* (4), 606-615.

133. Jauffred, L.; Samadi, A.; Klingberg, H.; Bendix, P. M.; Oddershede, L. B., Plasmonic Heating of Nanostructures. *CHEMICAL REVIEWS* **2019,** *119* (13), 8087-8130.

134. Gross, B.; Lockwood, S. Y.; Spence, D. M., Recent Advances in Analytical Chemistry by 3D Printing. *Anal. Chem.* **2017,** *89* (1), 57-70.

135. Kim, P.; Kwon, K. W.; Park, M. C.; Lee, S. H.; Kim, S. M.; Suh, K. Y., Soft lithography for microfluidics: a review. *BioChip J.* **2008,** *2* (1), 1-11.

136. Au, A. K.; Huynh, W.; Horowitz, L. F.; Folch, A., 3D-Printed Microfluidics. *Angew. Chem.-Int. Edit.* **2016,** *55* (12), 3862-3881.

137. Dirkzwager, R. M.; Liang, S. L.; Tanner, J. A., Development of Aptamer-Based Point-of-Care Diagnostic Devices for Malaria Using Three-Dimensional Printing Rapid Prototyping. *Acs Sensors* **2016,** *1* (4), 420-426.

138. Macdonald, N. P.; Currivan, S. A.; Tedone, L.; Paull, B., Direct Production of Microstructured Surfaces for Planar Chromatography Using 3D Printing. *Anal. Chem.* **2017,** *89* (4), 2457-2463.

139. Bechtold, S., 3D Printing, Intellectual Property and Innovation Policy. *IIC - International Review of Intellectual Property and Competition Law* **2016,** *47* (5), 517-536.

140. Waldbaur, A.; Rapp, H.; Lange, K.; Rapp, B. E., Let there be chip-towards rapid prototyping of microfluidic devices: one-step manufacturing processes. *Analytical Methods* **2011,** *3* (12), 2681-2716.

141. Chia, H. N.; Wu, B. M., Recent advances in 3D printing of biomaterials. *J. Biol. Eng.* **2015,** *9*, 4.

142. Li, F.; Smejkal, P.; Macdonald, N. P.; Guijt, R. M.; Breadmore, M. C., One-Step Fabrication of a Microfluidic Device with an Integrated Membrane and Embedded Reagents by Multimaterial 3D Printing. *Anal. Chem.* **2017,** *89* (8), 4701-4707.

143. Bauer, M.; Kulinsky, L., Fabrication of a Lab-on-Chip Device Using Material Extrusion (3D Printing) and Demonstration via Malaria-Ab ELISA. *Micromachines* **2018,** *9* (1), 27.

144. Fichou, D.; Morlock, G. E., Open-Source-Based 3D Printing of Thin Silica Gel Layers in Planar Chromatography. *Anal. Chem.* **2017,** *89* (3), 2116-2122.

145. Zhang, C. G.; Chen, C. J.; Settu, K.; Liu, J. T., Angle-Scanning Surface Plasmon Resonance System with 3D Printed Components for Biorecognition Investigation. *Adv. Condens. Matter Phys.* **2018**, 5654010.

146. Sood, A. K.; Ohdar, R. K.; Mahapatra, S. S., Parametric appraisal of mechanical property of fused deposition modelling processed parts. *Mater. Des.* **2010,** *31* (1), 287-295.

147. Belka, M.; Ulenberg, S.; Baczek, T., Fused Deposition Modeling Enables the Low-Cost Fabrication of Porous, Customized-Shape Sorbents for Small-Molecule Extraction. *Anal. Chem.* **2017,** *89* (8), 4373-4376.

148. Farahani, R. D.; Dube, M.; Therriault, D., Three-Dimensional Printing of Multifunctional Nanocomposites: Manufacturing Techniques and Applications. *Adv. Mater.* **2016,** *28* (28), 5794-5821.

149. Gross, B. C.; Anderson, K. B.; Meisel, J. E.; McNitt, M. I.; Spence, D. M., Polymer Coatings in 3D-Printed Fluidic Device Channels for Improved Cellular Adherence Prior to Electrical Lysis. *Anal. Chem.* **2015,** *87* (12), 6335-6341.

150. Waheed, S.; Cabot, J. M.; Macdonald, N. P.; Lewis, T.; Guijt, R. M.; Paull, B.; Breadmore, M. C., 3D printed microfluidic devices: enablers and barriers. *Lab on a Chip* **2016,** *16* (11), 1993-2013.

151. Gawedzinski, J.; Pawlowski, M. E.; Tkaczyk, T. S., Quantitative evaluation of performance of three-dimensional printed lenses. *Opt. Eng.* **2017,** *56* (8), 084110.

152. Paknahad, M.; Bachhal, J. S.; Ahmadi, A.; Hoorfar, M., Characterization of channel coating and dimensions of microfluidic-based gas detectors. *Sensors and Actuators B-Chemical* **2017,** *241*, 55-64.

153. Walczak, R.; Adamski, K., Inkjet 3D printing of microfluidic structures-on the selection of the printer towards printing your own microfluidic chips. *J. Micromech. Microeng.* **2015,** *25* (8), 085013.

154. Cooke, M. N.; Fisher, J. P.; Dean, D.; Rimnac, C.; Mikos, A. G., Use of stereolithography to manufacture critical-sized 3D biodegradable scaffolds for bone ingrowth. *J. Biomed. Mater. Res. Part B* **2003,** *64B* (2), 65-69.

155. Bartolo, P. J., Stereolithographic Processes. In *Stereolithography: Materials, Processes and Applications*, Bartolo, P. J., Ed. Springer: New York, USA, 2011; pp 1-36.

156. Ovsianikov, A.; Schlie, S.; Ngezahayo, A.; Haverich, A.; Chichkov, B. N., Two-photon polymerization technique for microfabrication of CAD-designed 3D scaffolds from commercially available photosensitive materials. *J. Tissue Eng. Regen. Med.* **2007,** *1* (6), 443-449.

157. Patel, D. K.; Sakhaei, A. H.; Layani, M.; Zhang, B.; Ge, Q.; Magdassi, S., Highly Stretchable and UV Curable Elastomers for Digital Light Processing Based 3D Printing. *Adv. Mater.* **2017,** *29* (15), 1606000.

158. Park, C.; Lee, J.; Kim, Y.; Kim, J.; Park, S., 3D-printed microfluidic magnetic preconcentrator for the detection of bacterial pathogen using an ATP luminometer and antibody-conjugated magnetic nanoparticles. *Journal of Microbiological Methods* **2017,** *132*, 128-133.

159. Calderilla, C.; Maya, F.; Cerda, V.; Leal, L. O., 3D printed device including disk-based solid-phase extraction for the automated speciation of iron using the multisyringe flow injection analysis technique. *Talanta* **2017,** *175*, 463-469.

160. Su, C. K.; Peng, P. J.; Sun, Y. C., Fully 3D-Printed Preconcentrator for Selective Extraction of Trace Elements in Seawater. *Anal. Chem.* **2015,** *87* (13), 6945-6950.

161. Ganesh, I.; Tran, B. M.; Kim, Y.; Kim, J.; Cheng, H.; Lee, N. Y.; Park, S., An integrated microfluidic PCR system with immunomagnetic nanoparticles for the detection of bacterial pathogens. *Biomedical Microdevices* **2016,** *18* (6), 116.

162. Tang, C. K.; Vaze, A.; Rusling, J. F., Automated 3D-printed unibody immunoarray for chemiluminescence detection of cancer biomarker proteins. *Lab on a Chip* **2017,** *17* (3), 484-489.

163. Santangelo, M. F.; Libertino, S.; Turner, A. P. F.; Filippini, D.; Mak, W. C., Integrating printed microfluidics with silicon photomultipliers for miniaturised and highly sensitive ATP bioluminescence detection. *Biosens. Bioelectron.* **2018,** *99*, 464-470.

164. Lee, W.; Kwon, D.; Choi, W.; Jung, G. Y.; Jeon, S., 3D-Printed Microfluidic Device for the Detection of Pathogenic Bacteria Using Size-based Separation in Helical Channel with Trapezoid Cross-Section. *Sci Rep* **2015,** *5*, 7717.

165. Liu, C. C.; Liao, S. C.; Song, J. Z.; Mauk, M. G.; Li, X. W.; Wu, G. X.; Ge, D. T.; Greenberg, R. M.; Yang, S.; Bau, H. H., A high-efficiency superhydrophobic plasma separator. *Lab on a Chip* **2016,** *16* (3), 553-560.

166. Kataoka, E. M.; Murer, R. C.; Santos, J. M.; Carvalho, R. M.; Eberlin, M. N.; Augusto, F.; Poppi, R. J.; Gobbi, A. L.; Hantao, L. W., Simple, Expendable, 3D-Printed Microfluidic Systems for Sample Preparation of Petroleum. *Anal. Chem.* **2017,** *89* (6), 3460-3467.

167. Han, N.; Shin, J. H.; Han, K. H., An on-chip RT-PCR microfluidic device, that integrates mRNA extraction, cDNA synthesis, and gene amplification. *Rsc Advances* **2014,** *4* (18), 9160-9165.

168. Hampson, S. M.; Rowe, W.; Christie, S. D. R.; Platt, M., 3D printed microfluidic device with integrated optical sensing for particle analysis. *Sensors and Actuators B-Chemical* **2018,** *256*, 1030-1037.

169. Patrick, W. G.; Nielsen, A. A. K.; Keating, S. J.; Levy, T. J.; Wang, W.; Rivera, J. J.; Mondragn-Palomino, O.; Carr, P. A.; Voigt, C. A.; Oxman, N.; Kong, D. S., DNA Assembly in 3D Printed Fluidics. *PLOS ONE* **2015,** *10* (12).

170. Wang, Y. J.; Zeinhom, M. M. A.; Yang, M. M.; Sun, R. R.; Wang, S. F.; Smith, J. N.; Timchalk, C.; Li, L.; Lin, Y. H.; Du, D., A 3D-Printed, Portable, Optical-Sensing Platform for Smartphones Capable of Detecting the Herbicide 2,4-Dichlorophenoxyacetic Acid. *Anal. Chem.* **2017,** *89* (17), 9339-9346.

171. Cevenini, L.; Calabretta, M. M.; Tarantino, G.; Michelini, E.; Roda, A., Smartphone-interfaced 3D printed toxicity biosensor integrating bioluminescent "sentinel cells". *Sensors and Actuators B-Chemical* **2016,** *225*, 249-257.

172. Schafer, M.; Brauler, V.; Ulber, R., Bio-sensing of metal ions by a novel 3D-printable smartphone spectrometer. *Sensors and Actuators B-Chemical* **2018,** *255*, 1902-1910.

173. Bayram, A.; Serhatlioglu, M.; Ortac, B.; Demic, S.; Elbuken, C.; Sen, M.; Solmaz, M. E., Integration of glass micropipettes with a 3D printed aligner for microfluidic flow cytometer. *Sensors and Actuators a-Physical* **2018,** *269*, 382-387.

174. Mendoza-Gallegos, R. A.; Rios, A.; Garcia-Cordero, J. L., An Affordable and Portable Thermocycler for Real-Time PCR Made of 3D-Printed Parts and Off-the-Shelf Electronics. *Anal. Chem.* **2018,** *90* (9), 5563-5568.

175. Comina, G.; Suska, A.; Filippini, D., Autonomous Chemical Sensing Interface for Universal Cell Phone Readout. *Angew. Chem.-Int. Edit.* **2015,** *54* (30), 8708-8712.

176. Comina, G.; Suska, A.; Filippini, D., A 3D printed device for quantitative enzymatic detection using cell phones. *Analytical Methods* **2016,** *8* (32), 6135-6142.

177. Hinman, S. S.; McKeating, K. S.; Cheng, Q., Plasmonic Sensing with 3D Printed Optics. *Anal. Chem.* **2017,** *89* (23), 12626-12630.

178. Vaidya, N.; Solgaard, O., 3D printed optics with nanometer scale surface roughness. *Microsyst. Nanoeng.* **2018,** *4*, 18.

179. Pandey, S.; Gupta, B.; Nahata, A., Terahertz plasmonic waveguides created via 3D printing. *Opt. Express* **2013,** *21* (21), 24422-24430.

180. Busch, S. F.; Castro-Camus, E.; Beltran-Mejia, F.; Balzer, J. C.; Koch, M., 3D Printed Prisms with Tunable Dispersion for the THz Frequency Range. *Journal of Infrared Millimeter and Terahertz Waves* **2018,** *39* (6), 553-560.

181. Squires, A. D.; Constable, E.; Lewis, R. A., 3D Printed Terahertz Diffraction Gratings And Lenses. *Journal of Infrared Millimeter and Terahertz Waves* **2015,** *36* (1), 72-80.

182. Destino, J. F.; Dudukovic, N. A.; Johnson, M. A.; Nguyen, D. T.; Yee, T. D.; Egan, G. C.; Sawvel, A. M.; Steele, W. A.; Baumann, T. F.; Duoss, E. B.; Suratwala, T.; Dylla-Spears, R., 3D Printed Optical Quality Silica and Silica-Titania Glasses from Sol-Gel Feedstocks. *Adv. Mater. Technol.* **2018,** *3* (6), 1700323.

183. Haring, A. P.; Khan, A. U.; Liu, G. L.; Johnson, B. N., 3D Printed Functionally Graded Plasmonic Constructs. *Adv. Opt. Mater.* **2017,** *5* (18), 1700367.

184. Nguyen, D. T.; Meyers, C.; Yee, T. D.; Dudukovic, N. A.; Destino, J. F.; Zhu, C.; Duoss, E. B.; Baumann, T. F.; Suratwala, T.; Smay, J. E.; Dylla-Spears, R., 3D-Printed Transparent Glass. *Adv. Mater.* **2017,** *29* (26), 1701181.

185. Weber, M. J., *Handbook of optical materials*. CRC Press: 2002.

186. Klein, J.; Stern, M.; Franchin, G.; Kayser, M.; Inamura, C.; Dave, S.; Weaver, J. C.; Houk, P.; Colombo, P.; Yang, M.; Oxman, N., Additive Manufacturing of Optically Transparent Glass. *3D Print. Addit. Manuf.* **2015,** *2* (3), 92-105.

Chapter 2: Orthogonal Analysis of Bacterial Protein Toxins by Carbohydrate Microarray-Coupled SPR Imaging and MALDI-MS

2.1 Introduction

Surface plasmon resonance (SPR) has long played a central role in biomedical and pharmacological research.[1] The label-free technique allows for analysis of many types of binding interactions between biomolecules in a simple and convenient manner that is real-time, highly sensitive, and non-destructive.[2] This fundamental ability of SPR has unlocked many applications across a broad spectrum of fields, such as drug delivery,[3, 4] cell-based analysis,[5-7] biomarker profiling,[8, 9] and disease diagnosis.[10, 11] Recently, label-free techniques like SPR have become more popular for food and environmental testing, as they are typically very fast, simple and straightforward compared to labeled techniques.[12-15] The fundamental sensing interaction is defined by the molecular binding of the target analytes, without requiring any additional reagents or complex procedural sequences. Despite their broad use, conventional SPR instruments are somewhat limited in the number of samples that can be analyzed at once, which has led to the increasing popularity of SPR imaging. Instead of measuring the change in angle of maximum incident light absorbance like conventional SPR, SPR imaging instead measures the change in light intensity at a fixed incident angle.[16] The benefit of this construction is that SPR imaging can collect reflected data using a camera, which can be aimed at an array composed of many individual elements. This drastically increases throughput and enables multiplexed analysis, making SPR imaging appealing for wider-spread sensing applications.[17, 18]

One area of weakness for SPR screening techniques is that the binding signal lacks a source of more complex information about the interacting molecules themselves. The unique configuration of SPR measurement allows for development of new methods and strategies with integration with other analytical tools that are surface based. Matrix-assisted laser desorption ionization time-of-flight mass spectrometry, or MALDI-TOF-MS, is a natural fit to couple with SPR, as depicted in Figure 2.1. Coupling to mass spectrometry techniques allows for specific molecular physiochemical determination.[19] MALDI-TOF-MS is the most synergistic technique for pairing to SPR, as both techniques are surface-based and generally label-free, and the ability of qualitative identification and analysis of captured analytes by MALDI is a great strength. The coupling of SPR to MALDI-TOF-MS, or SPR-MALDI, has primarily been reported for biological fluid-based protein analysis,[20-23] with more studies demonstrating proteomics analyses,[24] medicinal pathology studies,[25] and drug screening[26] and have all been conducted using SPR-MALDI. For sensing applications, MALDI allows for unambiguous identification of captured target analytes. Quantitative biological immunosensors have been developed that couple SPR and MALDI-MS for sensing of proteins using antibodies as the surface recognition element.[20, 27, 28] SPR imaging has also been applied to SPR-MALDI methods as a way to increase throughput.[22, 23] SPR-MALDI is an emerging technique, with excellent potential for development into new types of analytical sensing. Previous work in our lab utilizing SPR-MALDI has used self-assembled monolayers (SAMs) of perfluorinated alkanes as a means of immobilizing carbohydrate-based sensing molecules.[29, 30] Perfluorinated arrays show excellent compatibility with both the capture of proteins in SPR and subsequent release for

MALDI-MS analysis. This super-hydrophobic SAM-based immobilization presents a dense and ordered surface of sensing molecules in order to maximize capture efficiency.[31]

In this work, we report the fabrication of a perfluorinated carbohydrate array using plasmonic patterns for SPR-MALDI, and its application for high-throughput pathogen analysis from environmental samples (Figure 2.1). Cholera toxin (CT) was chosen as a model water-borne pathogenic target. Many bacterial proteins including CT have strong native binding to the carbohydrate moieties of natural receptors, which make an ideal platform for affinity capture and analysis by SPR-MALDI.[32] Affinity capture of bacterial proteins for MALDI-MS has been shown to be feasible,[33] but a high-throughput microarray that can additionally quantify the binding and robustly sense the target in a complex environmental matrix, river water, would be of great use for water quality measurements. Highly sensitive functionalized silicate gold microwell arrays were developed and used for coupling of SPR and MALDI-MS. A sensing surface was generated by embedding GM_1, the cell membrane carbohydrate moiety to which CT initially binds in host organisms, into the surface fluorocarbons. This served as a densely-packed sensing apparatus for highly efficient native CT capture, which could then be quantified in an array format via SPR imaging. An on-chip digestion of the protein leaves a peptide fingerprint that can be identified via MALDI-MS. Furthermore, the MALDI-MS step adds a means of qualitative identification even in extremely complex background, as the peptide peaks are clearly distinguishable even when mixed and digested with lysates of full bacteria *Escherichia coli* and *V. cholerae*, as could be found in a highly-contaminated water source. The method here is highly flexible, requiring only a strongly hydrophobic tail joined to the sensing

moiety. Since a wide range of water-borne bacterial protein toxins rely on similar types of cell binding interactions to cholera toxin, this substrate and methodology should have good applicability to a number of other diseases and could serve as a broader water-screening platform.

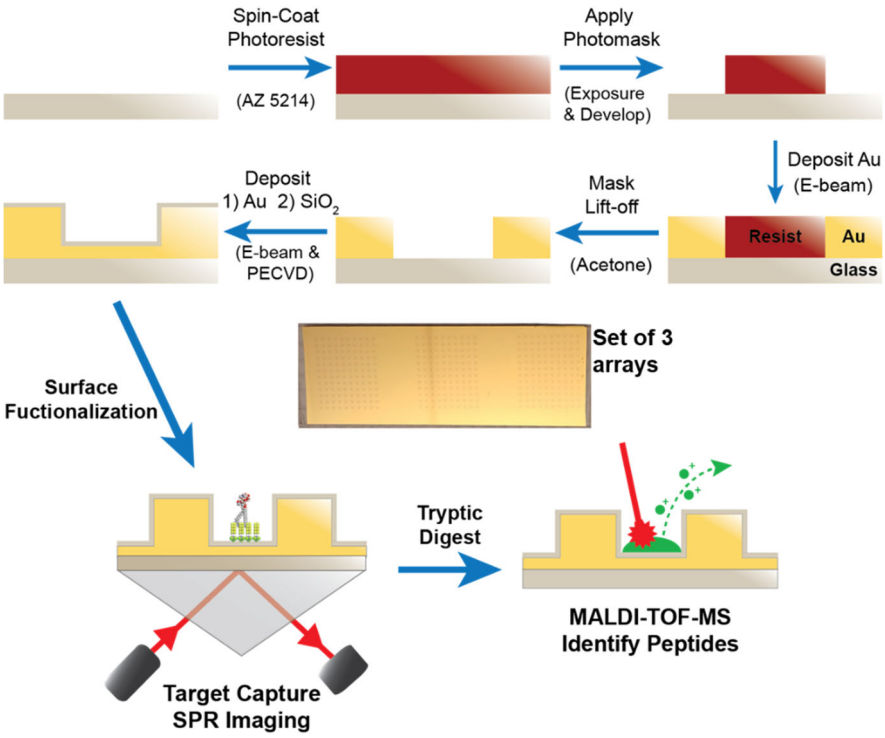

Figure 2.1. Schematic of the fabrication of the microarray substrate, along with subsequent steps of SPR-MALDI analysis.

2.2 Experimental Methods

Materials and Reagents. *1H,1H,2H,2H*-Perfluorodecyltrichlorosilane (PFDTS) was obtained from Fisher Scientific (Pittsburgh, PA). Monoganglioside GM_1, as NH_4^+ salt, was obtained from Matreya (Pleasant Gap, PA). Cholera Toxin (CT), trypsin, α-cyano-4-hydroxycinnamic acid (CHCA), LB broth (Miller), Triton X-100 and tris(hydroxymethyl)aminomethane (tris) were obtained from Sigma-Aldrich (St. Louis,

MO). BK-7 glass substrates were obtained from Corning (Painted Post, NY). Gold and chromium targets used for electron-beam evaporation were acquired as pellets of 0.9999% purity from Kurt. J Lesker (Jefferson Hills, PA). Bacteria *Escherichia coli* 25922 and *Vibrio cholerae* 39315 were purchased from ATCC (Manassas, Virginia) as powder.

Fabrication of SPR chips. Both SPR and SPR imaging chips were fabricated using BK-7 glass microscope slides as initial substrate, as reported previously.[34] The slides were cleaned with boiling piranha-etching solution (3:1 H_2SO_4:30% H_2O_2) for 1 hr, followed by rinsing with ultrapure water and drying with ethanol and compressed nitrogen gas. For conventional SPR chips, 2 nm of chromium (0.5 Å/s), followed by 48 nm of gold (2.0 Å/s), were deposited on one side of the slides via electron beam physical vapor deposition (EBPVD) (Temescal, Berkeley, CA). To form the final silica layer, 4 nm of SiO2 was deposited onto the gold layer via plasma enhanced chemical vapor deposition (PECVD) using a Unaxis Plasmatherm 790 system (Santa Clara, CA).

High-sensitivity gold well microarrays for SPR imaging analysis were fabricated according to previously developed methods[34] with some modification, as depicted in Figure 2.1. The cleaned glass substrates were spin-coated with hexamethyldisilazane (HMDS) to promote adhesion, then with AZ5214E at 4000 rpm for 45 s. After one minute of baking at 110 C, the photoresist was patterned into an array by UV exposure using a Karl-Suss MA-6 system and a patterned photomask, followed by standard photoresist development protocols. To form the well walls, a 2 nm layer of chromium followed by a 200 nm layer of gold were deposited via EBPVD. The remaining photoresist was lifted off using acetone, after which an additional 2 nm of chromium and 50 nm of gold were

deposited onto the surface with EBPVD to form the surface of the actual wells. The final microarray consisted of a 10 × 10 array of wells that were 600 μm in diameter and 250 nm deep. A final PECVD deposition of 4 nm SiO_2 created the full array substrate to be functionalized.

Surface Functionalization and Preparation. Prior to use, each SPR and SPRi substrate was rinsed with ethanol and dried with nitrogen. In order to form the fluorinated monolayer, the chips were then submerged in 1 mM *1H,1H,2H,2H*-perfluorodecyltrichlorosilane (PFDTS) diluted in toluene, for 30 min, then rinsed with toluene, ethanol and deionized (DI) water, then blown dry with N_2. 20 μL of a solution of 100 μg/mL of GM_1 in chloroform was then pipetted onto the chip and was quickly covered with a glass cover slip and allowed to incubate to dryness. Control experiments were conducted without the incubation of GM_1. Contact angle measurements of the relative surfaces were performed on a home-built device with deionized water (1 μL). The images for water droplets on substrate were collected by a computer controlled 12-bit cooled CCD camera. All measurements were made in ambient atmosphere at room temperature.

SPR and SPR imaging analysis. A dual-channel SPR spectrometer, **NanoSPR5-321** (NanoSPR, Chicago, IL), with a GaAs semiconductor laser light source (λ = 670 nm) was used for all spectroscopic measurements for conventional SPR. The device was equipped with a manufacturer-supplied prism of high refractive index (n = 1.61) and a 30 μL flow cell. Surface interactions at the functionalized substrate-liquid interface were monitored using the angular scanning mode and tracking the resonance angle.

SPR imaging was conducted via a home-built setup, a detailed description of which was reported in previous work.[35] In brief, each functionalized gold well microarray was mounted onto an optical stage that housed an S-shaped flow cell. The array was placed in contact with an equilateral SF2 prism (n = 1.616) with a layer of refractive index matching fluid (n = 1.616, Cargill Laboratories, Cedar Grove, NJ), The optical stage was fixed to a rotatable goniometer that allowed manual tuning of the incident angle of a 648 nm light emitting diode (LED) source that was used for SPR excitation. Reflected images of the microarray were captured by a cooled 12-bit CCD camera (QImaging Retiga 1300) with a resolution of 1.3 MP (1280 × 1024 pixels) and 6.7 μm × 6.7 μm pixel size. Real time changes in reflectance upon injection of sample solutions were recorded every 300 ms inside the individual well elements. Difference images were obtained by digitally subtracting the images, before and after incubation, from each other. Intensity data was normalized by dividing the intensity from p-polarized light by the intensity generated by s-polarized light.

During analysis for both SPR and SPR imaging, home-built fluidic systems ran 1×PBS as the running buffer at 5 mL/h at ambient temperature. Solutions of cholera toxin at varying concentrations in 1 × PBS were incubated for 30 min before rinsing. Additionally, CT was spiked into water samples collected from the Santa Ana River in Riverside, CA.

Cell Culture and Lysis. Each bacterial cell line was cultured in LB broth in culture flasks for 48 hr. Initial reconstitution of pellets, culturing and final aliquoting was done in a BSL-2 biosafety cabinet. Bacterial concentrations were determined with a 0.0025 mm^2

cell counting chamber (Zenith Lab, Changzhou, China) and a light microscope. Cell lysis was conducted in a lysis buffer consisting of 1% Triton X-100, 5% glycerol and 25 mM Tris HCl with a pH of 7.4. Solutions were mixed and incubated on ice with agitation for 30 min, followed by centrifugation at 15000 rpm for 5 min through a 3 kDa cutoff centrifuge filter to remove debris and lysis buffer, and remaining lysate solution was stored at -20 °C until use.

On-Chip Digestion and MALDI-MS analysis. Cholera toxin that was captured on the surface was enzymatically digested by spotting on each microwell 5 µL of 0.05 mg/mL trypsin in 100 mM Tris buffer pH 8.3. The digestion was carried out at 37 ºC for 8 h in a humidified chamber to minimize solvent evaporation. Multiple digestion times were tested, and 8 h was chosen as sufficient to distinguish the peptide peaks in the resulting MALDI-MS spectra. After digestion, the chip was then removed from the chamber and allowed to dry, followed by a 5 µL DI H_2O desalting step to remove buffer salts. As MALDI matrix, CHCA was diluted to 10 mg/mL 50 % acetonitrile, 49 % DI H_2O, and 1% trifluoroacetic acid. One microliter of matrix solution was pipetted onto each digested microwell and allowed to dry. Chips were mounted on a steel MALDI plate and analyzed with an AB SCIEX TOF/TOF 5800 spectrometer operating in positive ion reflector mode with a laser fluence of 4500.

Peptide masses in the resulting spectra were confirmed with the FindPept tool in Expasy,[36] as well as compared to literature sources. At low concentrations, CT detection was defined as containing at least four of the characteristic peptide masses. Cholera toxin b subunit was detected on the surface as a control using linear mode. The surface was also

analyzed for standard GM_1 peaks after GM_1 incubation in negative ion mode. GM_1 was spotted onto a standard stainless-steel plate for comparison peak analysis.

2.3 Results and Discussion

Surface capture of cholera toxin and detection by SPR. Protein analysis via coupling MALDI and SPR has been an active area of interest in recent years,[37] as the techniques have very synergistic strengths and weaknesses, along with using similar surface-based substrates.. SAMs of perfluorinated hydrocarbons have shown promise as the basis for microarrays, as their ordered nature and intense hydrophobicity can strongly adhere to a hydrophobic tag that is attached to analyte, presenting the antigenic sensing site in an ordered arrangement.[38] We have reported that a silicated gold surface shows high plasmonic response to even unamplified surface binding, so we sought to combine the concepts into a capture surface for bacterial proteins, which have strong native binding to their host cell targets. To generate the fluorodecan monolayer, the silicated gold surface is immersed in a solution PFDTS, and the chlorine substituents quickly hydrolyze and polymerize to form oxygen bridges with both nearby PFDTS molecules and the SiO_2 substrate surface,[39] as depicted in Figure 2.2. The hydrophilic nature of the silica substrate further promotes the ordering of the monolayer out away from the silica surface. The incubation of ganglioside GM_1 on the surface embeds the sensing apparatus into the monolayer, which serves to display the molecule in a dense, ordered arrangement. Cholera toxin's B subunit (blue in Figure 2.2a) is the recognition element of the protein, and it targets the GM_1 displayed on the surface of host cells before endocytosis, binding very

tightly to the sialic acid and carbohydrate moieties of the GM_1.[40] The AB_5 structure of CT has been shown to lead to multiple-site binding,[41-43] which this microarray takes advantage of through the dense packing of the sensing molecule. This concept, in principle, could be applied to a range of other bacterial proteins, as they are of similar AB_5 structure and frequently target surface glycans of the cells of host organisms.[44, 45]

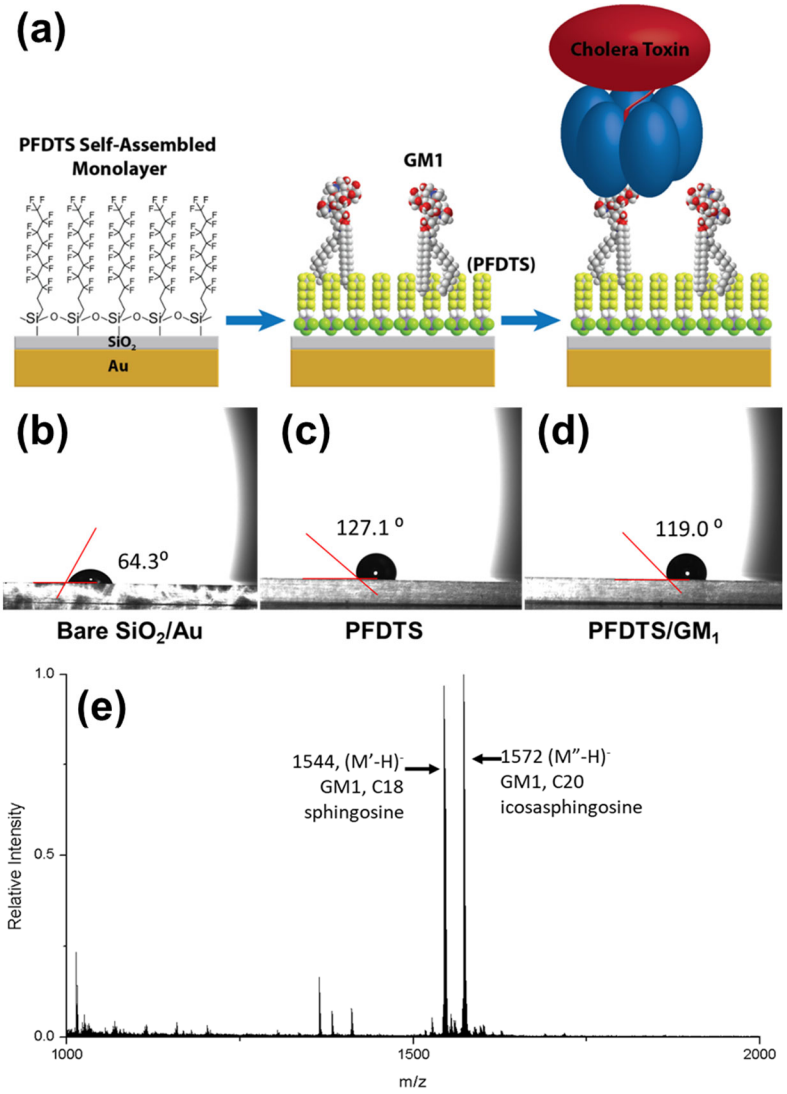

Figure 2.2. (a) Surface functionalization scheme for the capture of cholera toxin protein. (b-d): contact angle measurements of substrate at varying stages of functionalization. (e) MALDI-TOF-MS of incubated GM_1 post-wash.

To confirm the surface functionalization of the microarray, some surface characterization was carried out. First, contact angle was used as a check of the hydrophobicity of the surface, and so confirm the perfluorination, and is shown in Figure 2.2b-d. Initially, the thin SiO_2 top layer of the chip creates a slightly hydrophilic contact angle (64 º). Once the PFDTS SAM is polymerized onto the surface, the contact angle drastically increases to 127 º, which is near the standard range of a superhydrophobic surface.[46] This indicates a successful PFDTS surface assembly. After incubation of the GM_1 onto the surface, the contact angle decreases somewhat, to 119 º, as the carbohydrate groups of the ganglioside present a hydrophilic molecule amongst the PFDTS monolayer without completely removing the hydrophobic character of the surface. This is important for the flexibility of the microarray, as a retention of the surface hydrophobicity aids its effectiveness for MALDI chip preparation techniques such as desalting.[47] Second, MALDI-MS was conducted on the microarray surface after GM_1 incubation and thorough rinsing with DI H_2O to remove unimbedded ganglioside. Standard GM_1 ions were identified in their two native forms, with a sphingosine tail (m/z 1544) and an icosasphingosine tail (m/z 1572).[48, 49] This indicates that the microarray surface will retain the embedded ganglioside across exposure of aqueous solutions throughout the later steps of analysis. To confirm that the perfluorinated SAM is the source of the retention of peaks, we also spotted GM_1 onto a conventional stainless-steel MALDI plate and analyzed for the GM_1 ions before and after on-plate rinsing, and found no comparable m/z signal.

To test and optimize the protein capture effectiveness of the microarray, initial analysis was carried out via conventional SPR. Since most of the surface modification is off-line, the actual SPR analysis is very straightforward, consisting of simply the incubation of the sample CT solutions. This is followed by a rinse, which gives the final resonant angle shift due CT captured by the surface. As shown in Figure 2.3, nearly all of the SPR angle shift due to CT incubation remains after rinse, which is indicative of the strong binding between the CT and the GM_1 array. The angle shift also correlates well to the concentration of CT being incubated, an important characteristic for the use of the surface for a microarray sensor. To account for the effect of non-specific binding to the surface, CT was incubated onto a chip that had been prepared identically except that GM_1 was not incubated. At most concentrations, this non-specific signal was ~20-25% of the specific one. This indicates that this capture interface is largely interacting based on the binding pocket interactions of CTB and GM_1, rather than hydrophobic-hydrophobic interactions between the PFDTS and the overall protein. In total, when subtracting for the non-specific binding, the SPR signal a linear calibration can be constructed over a portion of the analyzed CT concentrations, the lowest being 1 μg/mL, shown in Figure 2.3c. This gives a good indication that the fluorinated surface can be used in further sensing applications.

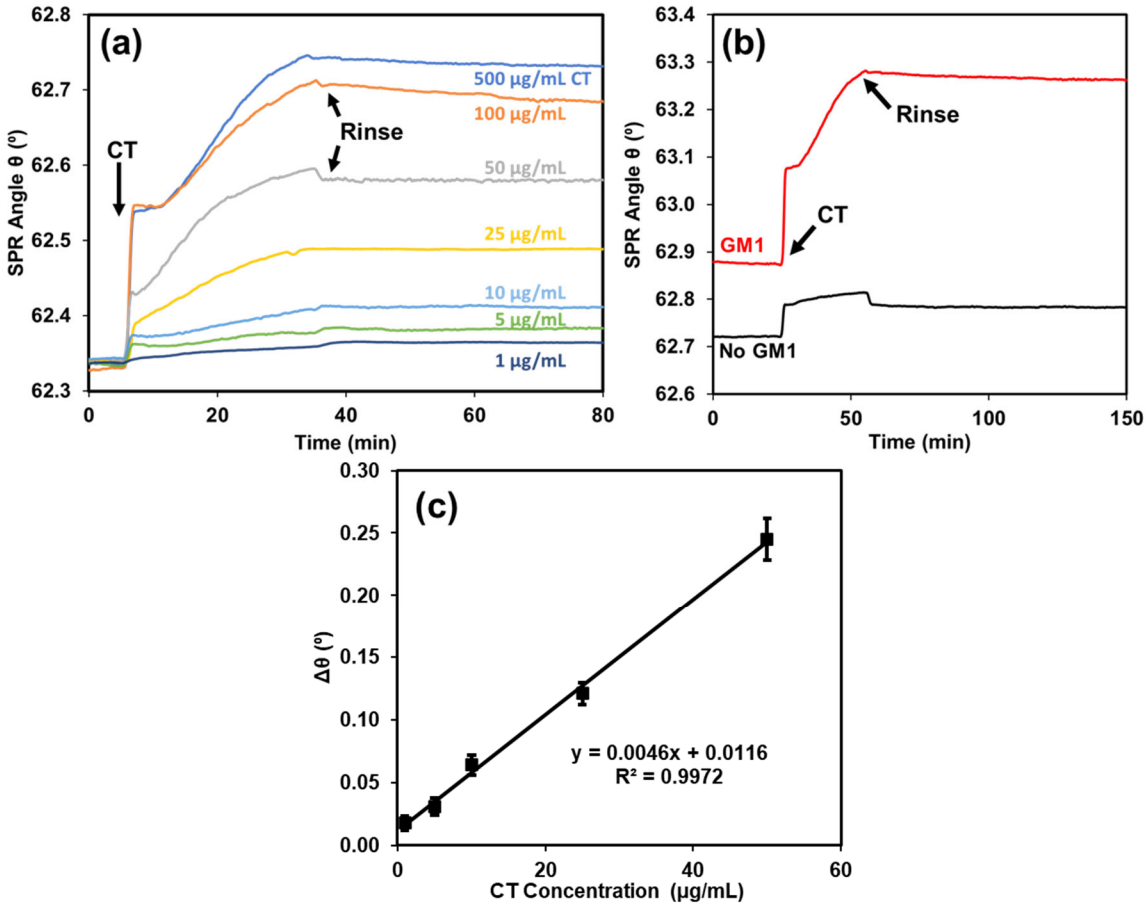

Figure 2.3. (a) SPR sensorgrams of varying concentrations of CT via conventional SPR. (b) Comparison of sensorgrams of cholera toxin capture for specific (red) vs non-specific (black) binding. (c) Conventional SPR Calibration of angle change versus CT concentration.

SPR Imaging detection of cholera toxin by microarray in river water. There is a need for high-throughput strategies for monitoring of water-borne diseases such as cholera over a long period of time. SPR imaging overcomes the low-throughput limits of conventional SPR, as many elements can be analyzed at once. Here, we combined this fluorocarbon-based surface capture scheme with an SPR imaging microarray that gives high plasmonic response and low background. We have previously reported SPRi arrays based on gold microwells with thick gold walls for attenuating background plasmonic

signal,[34] and a layer of silica to improve plasmonic response.[50] Here, we used an updated array fabrication, that both simplifies the procedure and increases the structural stability of the chips, which is crucial to their usability in multi-platform methodologies.

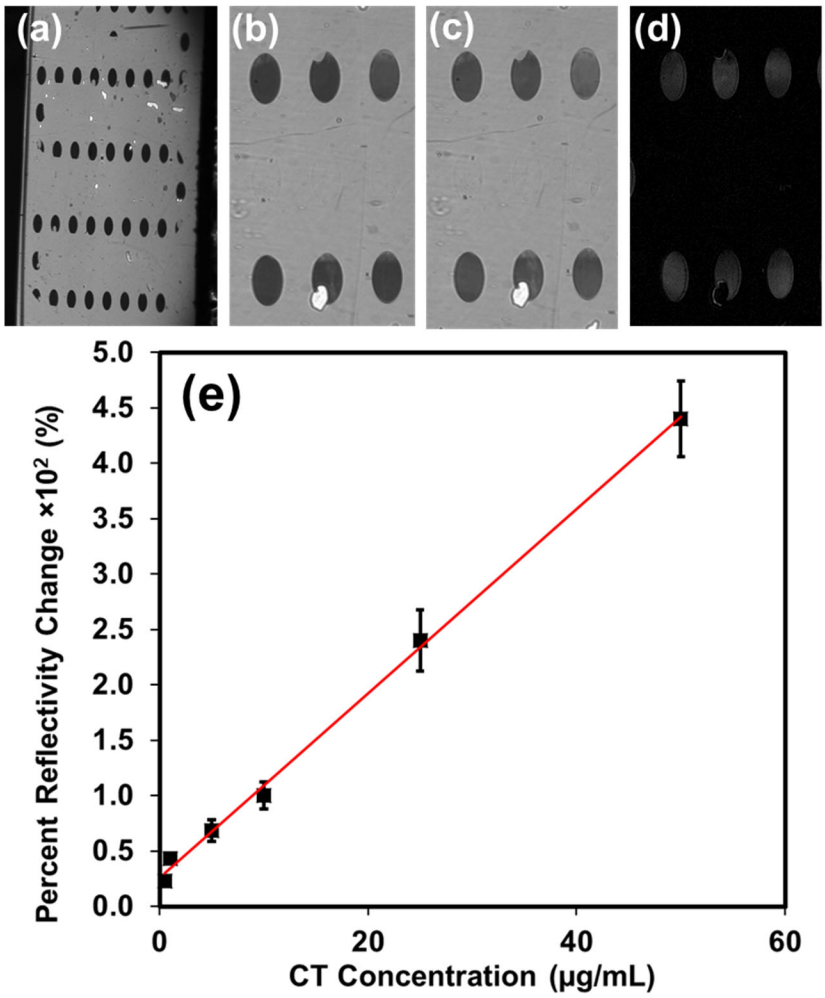

Figure 2.4. (a) Image of SPRi-mounted array. Microwells (a) before and (b) after 100 µg/mL CT capture, and (c) difference image. (d) Calibration of SPRi reflectivity change versus CT concentration in PBS.

To demonstrate the effectiveness of the array at CT quantification via SPR imaging, CT solutions were added to a flow cell that incubated onto microwells that had been spotted

with GM_1. Images of the microarray can be seen in Figure 2.4a. The binding of CT to the surface shifts the reflectivity curve, increasing the brightness of the array elements. The intensity was measured before and after CT incubation (Figure 2.4b), and a calibration of CT concentration to intensity change as a percent of maximum intensity is given in Figure 2.4c. As with conventional SPR, the response is linear, and, as expected, is somewhat more sensitive, as the 3σ limit of detection is 242 ng/mL, or 2.8 nM, The native binding affinity of GM_1 to CT has been reported to be ~10 pM,[51] indicating that the microarray is approaching the lower limits of possible detection for an unamplified technique. This reflects the dense, ordered presentation of GM_1 binding moieties to the CT proteins effectively maximizing the possible surface binding interactions. This detection limit is on the higher end of the clinically relevant range for CT detection,[52] but as a proof of concept, still reaches acceptable levels for CT water quality monitoring.

An important feature of any methodology for water monitoring is the ability to accurately quantify the target analyte in the native medium. This removes the need for pretreatment or dilution sample preparation steps. To demonstrate the effectiveness of our microarray surface at quantifying bacterial toxins in the water supply, water samples were collected from a local water source, the Santa Ana River, which has a history of significant pollution.[53] CT protein was spiked into the water before injecting into the SPR imaging flow cell and analyzing similarly to previous. There were no noticeable interferences with analysis aside from the slight refractive index mismatch between the running buffer and the incubated river water, which dissipated upon rinsing. This introduced some noise into the data, but the resulting LOD for CT was 3.3 nM in river water matrix, indicating the

robustness of the surface to interferences from the river water. The nearly super-hydrophobic property of the surface, while also serving as a link to MALDI-MS analysis, functions here as an ideally robust surface for analysis in even a environmental river water matrix.

MALDI-MS identification. While SPR can give excellent, stable long-term quantitative data, it lacks the type of absolute determination of protein identity afforded by mass spectrometry techniques. MALDI-TOF-MS, as a tandem technique, can serve as a way to qualitatively confirm the identity of analytes captured by the perfluorinated microarray. Perfluorinated surfaces have been shown to be advantageous for MALDI-MS array analysis, especially for display of carbohydrates for protein capture. Therefore, we can couple MALDI-TOF-MS analysis onto the end of our SPR imaging technique by removing the flow cell and carrying out a tryptic digest on the wells that had been in the flow path. Though cholera toxin A and B subunits are 28 and 11 kDa, respectively,[54] which fall in the analyzable MALDI range, ionization efficiency for MALDI is significantly reduced above ~1 kDa,[55] lowering the effectiveness of a sensing methodology. Digestions of captured proteins are common when analyzing for high-mass proteins,[19, 27, 56] and so was employed here. A large protein will have many resulting peptides with which to construct a biological "fingerprint" for protein identification, and hydrophobic of the microwell assists in retaining the peptides on the surface. A benefit of this procedure is that a subset of peptides which should be enough for positive ID even if not every mass is present.

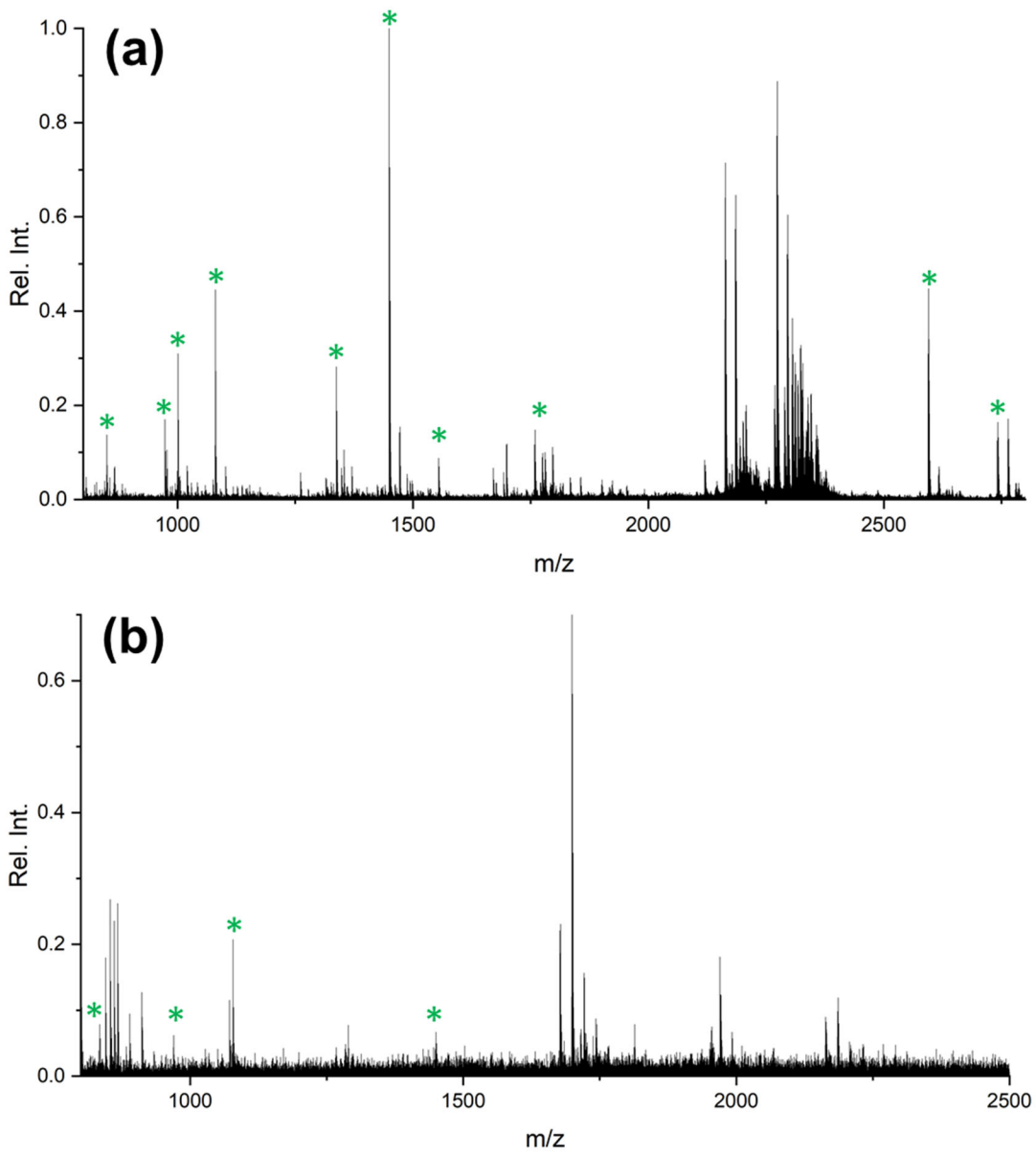

Figure 2.5. MALDI-TOF-MS spectra of (a) CT direct on-chip digestion and (b) CT in river water after SPR imaging incubation followed by MALDI on-chip digestion. Green indicators show CT peptide peaks from Table 2.1.

Table 2.1. CT peptide peaks identified from on-chip digestion.

m/z	Cholera Toxin Peptide
845	QSGGLMPR
973	EMAIITFK
1001	GQSEYFDR
1080	GLAGFPPEHR
1371	IFSYTESLAGKR
1449	HDDGYVSTSISLR
1532	GTQMNINLYDHAR
1781	QIFSGYQSDIDTHNR
2594	YYSNLDIAPAADGYGLAGFP PEHR
2741	NVNDVLGAYSPHPDEQEVSA LGGIPY

Determination of available peaks was carried by spotting higher CT concentrations (10 µg per well) onto the functionalized microwell array. A typical spectrum after tryptic digestion is shown in Figure 2.5a, and Table 2.1 details the peptides corresponding to each mass, as previously identified in literature.[33, 57] In testing the lower limit of this qualitative detection, CT was spiked into river water solutions, and the lowest level of positive qualitative detection was found to be 50 ng of CT per well, a spectrum of which can be seen in Figure 2.5b. On wells where river water with no spiked CT was incubated, the characteristic peaks were not observed. This detection level indicates good compatibility with SPR imaging sensing, as the MALDI sensitivity is higher, ensuring that any protein detected with SPR imaging can be confidently identified by the subsequent MALDI analysis. This analysis simplifies oftentimes dense and complex data analysis associated with MALDI. In a complex medium like river water, shrinking the identification process into a straightforward band of peptide peaks. In addition, further development is possible, as this is likely not the maximum sensitivity possible with an on-chip digestion, as some sample loss is created in the post-digestion desalting. Further work could focus on

developing techniques to concentrate the peptide peaks on the well surface to explore the possibility of extremely high sensitivity via MALDI-MS.

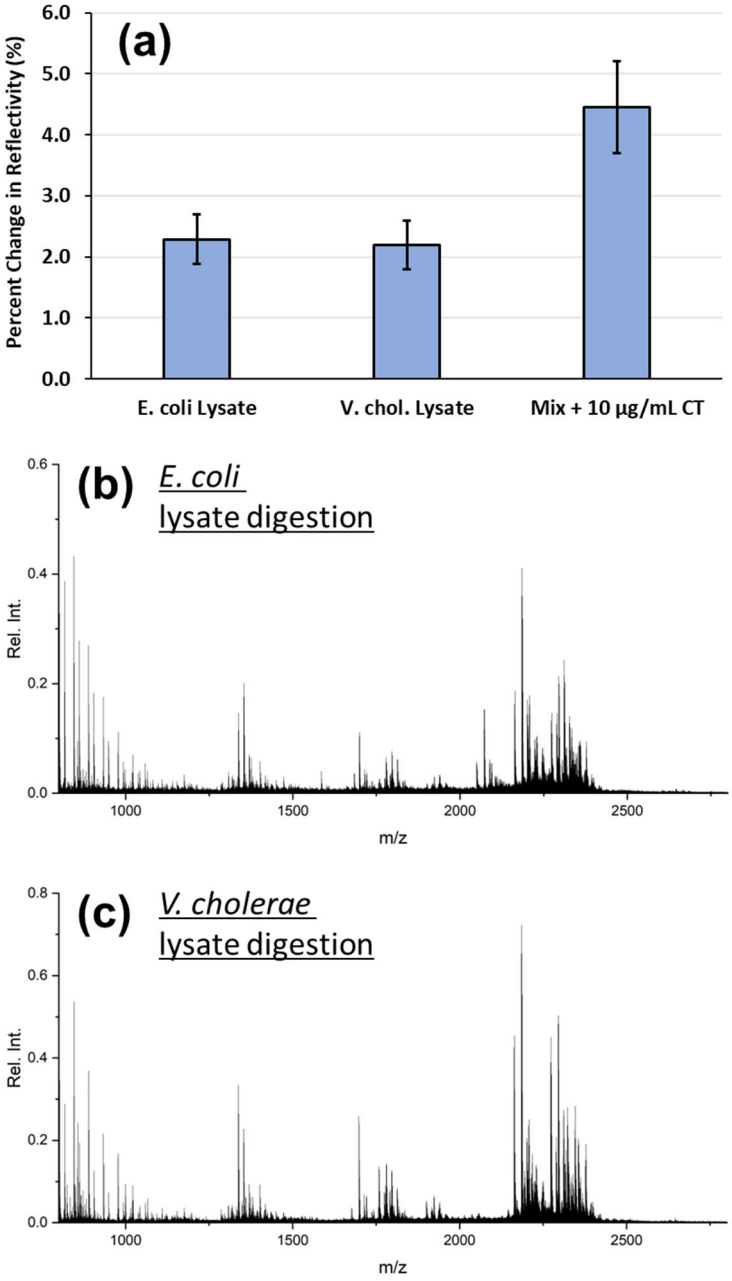

Figure 2.6. (a) Average SPR imaging responses from various complex mixtures. MALDI-TOF-MS spectra of in-tube tryptic digestions of (b) *E. coli* and (c) *V. cholerae* spotted on functionalized microarray.

SPR-MALDI in highly-contaminated matrix. For the monitoring of water-quality, a sensing system would need to be robust enough to be able to identify the specific toxic agents even in water that is highly contaminated. Outbreaks of diseases like cholera frequently coincide with natural disasters,[58] as flooding renders many water control methods moot, and these disasters are only becoming more prevalent with the escalation of climate change.[59] As such, the SPR-MALDI methodology was applied to cholera toxin spiked in a highly bacterially rich matrix. Both *V. cholerae* and *E. coli* were separately cultured and lysed, then a 1:1 mixture of the resulting lysates was used as the matrix for the SPR and MALDI analyses. Figure 2.6a shows the relative SPR imaging responses of the individual lysates and the mixture spiked with 10 μg/mL of CT. The binding response of the CT-based mixture was strong and much higher than the mixtures, indicating that while a background response is present, it does not necessarily pose a challenge to effective quantitation.

The MALDI-MS profiles of in-tube tryptic digestions of the two bacteria are shown in Figure 2.6b,c, and in comparison with the CT spectrum in Fig. 5a, the overlaps in the spectra not appear to be significant enough to interfere with the identification. To more thoroughly confirm this, full SPR-MALDI analysis with the CT-spiked lysate mix was conducted, and an averaged MALDI-MS spectrum is shown in Figure 2.7. Peaks for m/z = 845, 973, 1001, 1080, 1449, 1471 (sodiated peak of 1449), and 2594 from the CT identification were still clearly distinguishable and did not overlap with any peaks in the lysate that had a S/N ratio > 5. Notably, the very high initial concentration of the lysed cells (~10^5 cfu) did not significantly alter the identification of CT peptide peaks. The peptide

peaks being clearly visible reflects the toxin protein much stronger binding to the surface than the contaminants, so the relative amount of material to be digested and detected is accordingly much higher.

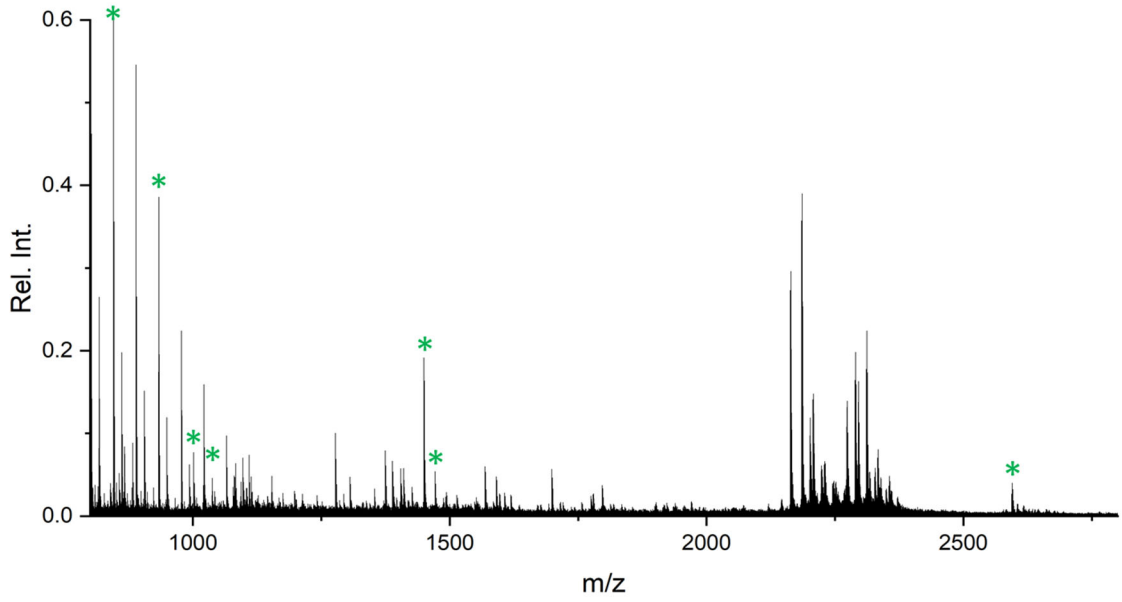

Figure 2.7. MALDI-TOF-MS portion of SPR-MALDI of CT-spiked mix of E. coli and V. cholerae lysate mixture. Green indicators show previously-identified CT peptide peaks.

2.4 Conclusion

The combination of SPR imaging and MALDI-TOF-MS into an integrated sensing platform for high-throughput sensing of bacterial proteins was achieved via a fluorinated gold microwell array. SPR imaging was able to detect cholera toxin protein at clinically relevant levels across a wide swath of microwells in an array. After a trypsin digestion of the captured protein, MALDI-TOF-MS analysis was able to identify a profile of characteristic peptides that qualitatively confirmed the identity of the analyte. The

fundamental advantages of both techniques were largely unaffected by the use of river water environmental matrix, and the SPR response and MALDI profile of target peptide peaks was still clearly visible even when spiked into a mixture of cell lysates. This platform should be very flexible for different types of protein sensing, as the type of sensing molecule can be substituted as long as it has a hydrophobic tail with which to insert into the perfluorinated SAM. This methodology should serve as an excellent basis for optimization and future development into a larger, multiplexed, and even more sensitive type of environmental screening technology.

2.5 References

1. Anker, J. N.; Hall, W. P.; Lyandres, O.; Shah, N. C.; Zhao, J.; Van Duyne, R. P., Biosensing with plasmonic nanosensors. *Nat. Mater.* **2008,** *7* (6), 442-453.

2. Homola, J., Surface plasmon resonance sensors for detection of chemical and biological species. *Chem. Rev.* **2008,** *108* (2), 462-493.

3. Hong, S.; Leroueil, P. R.; Majoros, I. J.; Orr, B. G.; Baker, J. R.; Holl, M. M. B., The binding avidity of a nanoparticle-based multivalent targeted drug delivery platform. *Chem. Biol.* **2007,** *14* (1), 107-115.

4. Cai, D. F.; Gao, W.; He, B.; Dai, W. B.; Zhang, H.; Wang, X. Q.; Wang, J. C.; Zhang, X.; Zhang, Q., Hydrophobic penetrating peptide PFVYLI-modified stealth liposomes for doxorubicin delivery in breast cancer therapy. *Biomaterials* **2014,** *35* (7), 2283-2294.

5. Yashunsky, V.; Lirtsman, V.; Golosovsky, M.; Davidov, D.; Aroeti, B., Real-Time Monitoring of Epithelial Cell-Cell and Cell-Substrate Interactions by Infrared Surface Plasmon Spectroscopy. *Biophys. J.* **2010,** *99* (12), 4028-4036.

6. Maltais, J. S.; Denault, J. B.; Gendron, L.; Grandbois, M., Label-free monitoring of apoptosis by surface plasmon resonance detection of morphological changes. *Apoptosis* **2012,** *17* (8), 916-925.

7. Shevchenko, Y.; Camci-Unal, G.; Cuttica, D. E.; Dokmeci, M. R.; Albert, J.; Khademhosseini, A., Surface plasmon resonance fiber sensor for real-time and label-free monitoring of cellular behavior. *Biosens. Bioelectron.* **2014,** *56*, 359-367.

8. Ibn Sina, A. A.; Vaidyanathan, R.; Dey, S.; Carrascosa, L. G.; Shiddiky, M. J. A.; Trau, M., Real time and label free profiling of clinically relevant exosomes. *Sci Rep* **2016,** *6*, 9.

9. Tyagi, D.; Perez, J. B.; Nand, A.; Cheng, Z. Q.; Wang, P. Z.; Na, J.; Zhu, J. S., Detection of embryonic stem cell lysate biomarkers by surface plasmon resonance with reduced nonspecific adsorption. *Anal. Biochem.* **2015,** *471*, 29-37.

10. Kim, S.; Lee, H. J., Direct Detection of alpha-1 Antitrypsin in Serum Samples using Surface Plasmon Resonance with a New Aptamer-Antibody Sandwich Assay. *Anal. Chem.* **2015,** *87* (14), 7235-7240.

11. Liu, L.; Xia, N.; Wang, J. X., Potential applications of SPR in early diagnosis and progression of Alzheimer's disease. *RSC Adv.* **2012,** *2* (6), 2200-2204.

12. Raz, S. R.; Haasnoot, W., Multiplex bioanalytical methods for food and environmental monitoring. *Trac-Trends Anal. Chem.* **2011,** *30* (9), 1526-1537.

13. Ivnitski, D.; Abdel-Hamid, I.; Atanasov, P.; Wilkins, E., Biosensors for detection of pathogenic bacteria. *Biosens. Bioelectron.* **1999,** *14* (7), 599-624.

14. Masdor, N. A.; Altintas, Z.; Tothill, I. E., Surface Plasmon Resonance Immunosensor for the Detection of Campylobacter jejuni. *Chemosensors* **2017,** *5* (2), 15.

15. Yakes, B. J.; Papafragkou, E.; Conrad, S. M.; Neill, J. D.; Ridpath, J. F.; Burkhardt, W.; Kulka, M.; DeGrasse, S. L., Surface plasmon resonance biosensor for detection of feline calicivirus, a surrogate for norovirus. *Int. J. Food Microbiol.* **2013,** *162* (2), 152-158.

16. Kodoyianni, V., Label-free analysis of biomolecular interactions using SPR imaging. *Biotechniques* **2011,** *50* (1), 32-40.

17. Scarano, S.; Mascini, M.; Turner, A. P. F.; Minunni, M., Surface plasmon resonance imaging for affinity-based biosensors. *Biosens. Bioelectron.* **2010,** *25* (5), 957-966.

18. Manuel, G.; Luptak, A.; Corn, R. M., A Microwell-Printing Fabrication Strategy for the On-Chip Templated Biosynthesis of Protein Microarrays for Surface Plasmon Resonance Imaging. *J. Phys. Chem. C* **2016,** *120* (37), 20984-20990.

19. David Bonnel, D. M., Gerardo R. Marchesini, Label-Free Biosensor Affinity Analysis Coupled to Mass Spectrometry. In *Analyzing Biomolecular Interactions by Mass Spectrometry*, Jeroen Kool, W. M. A. N., Ed. Wiley: Weinheim, Germany, 2015; pp 299-316.

20. Rouleau, A.; El Osta, M.; Lucchi, G.; Ducoroy, P.; Boireau, W., Immuno-MALDI-MS in Human Plasma and On-Chip Biomarker Characterizations at the Femtomole Level. *Sensors* **2012,** *12* (11), 15119-15132.

21. Musso, J.; Buchmann, W.; Gonnet, F.; Jarroux, N.; Bellon, S.; Frydman, C.; Brunet, D. L.; Daniel, R., Biomarkers probed in saliva by surface plasmon resonance imaging coupled to matrix-assisted laser desorption/ionization mass spectrometry in array format. *Anal. Bioanal. Chem.* **2015,** *407* (5), 1285-1294.

22. Kim, Y. E.; Yi, S. Y.; Lee, C. S.; Jung, Y.; Chung, B. H., Gold patterned biochips for on-chip immuno-MALDI-TOF MS: SPR imaging coupled multi-protein MS analysis. *Analyst* **2012,** *137* (2), 386-392.

23. Forest, S.; Breault-Turcott, J.; Chaurand, P.; Masson, J. F., Surface Plasmon Resonance Imaging-MALDI-TOF Imaging Mass Spectrometry of Thin Tissue Sections. *Anal. Chem.* **2016,** *88* (4), 2072-2079.

24. Zheng, P.; Zhong, Q.; Xiong, Q.; Yang, M. K.; Zhang, J.; Li, C. Y.; Bi, L. J.; Ge, F., QUICK identification and SPR validation of signal transducers and activators of transcription 3 (Stat3) interacting proteins. *J. Proteomics* **2012,** *75* (3), 1055-1066.

25. Shi, Q.; Yin, S. M.; Kaluz, S.; Ni, N. T.; Devi, N. S.; Mun, J. Y.; Wang, D. Z.; Damera, K.; Chen, W. X.; Burroughs, S.; Mooring, S. R.; Goodman, M. M.; Van Meir, E. G.; Wang, B. H.; Snyder, J. P., Binding Model for the Interaction of Anticancer Arylsulfonamides with the p300 Transcription Cofactor. *ACS Med. Chem. Lett.* **2012,** *3* (8), 620-625.

26. Minunni, M.; Tombelli, S.; Mascini, M.; Bilia, A.; Bergonzi, M. C.; Vincieri, F. F., An optical DNA-based biosensor for the analysis of bioactive constituents with application in drug and herbal drug screening. *Talanta* **2005,** *65* (2), 578-585.

27. Anker, J. N.; Hall, W. P.; Lambert, M. P.; Velasco, P. T.; Mrksich, M.; Klein, W. L.; Van Duyne, R. P., Detection and Identification of Bioanalytes with High Resolution LSPR Spectroscopy and MALDI Mass Spectrometry. *J. Phys. Chem. C* **2009,** *113* (15), 5891-5894.

28. Trenchevska, O.; Kamcheva, E.; Nedelkov, D., Mass spectrometric immunoassay for quantitative determination of transthyretin and its variants. *Proteomics* **2011,** *11* (18), 3633-3641.

29. Yang, H.; Chan, A. L.; LaVallo, V.; Cheng, Q., Quantitation of Alpha-Glucosidase Activity Using Fluorinated Carbohydrate Array and MALDI-TOF-MS. *ACS Appl. Mater. Interfaces* **2016,** *8* (4), 2872-2878.

30. Yang, H.; Cheng, Q., Chemoselective ligation reaction of N-acetylglucosamine (NAG) with hydrazide functional probes to determine galactosyltransferase activity by MALDI mass spectrometry. *Analyst* **2017,** *142* (14), 2654-2662.

31. Song, E. H.; Pohl, N. L. B., Fluorous-based small-molecule microarrays for protein, antibody and enzyme screening. *Future Med. Chem.* **2009,** *1* (5), 889-896.

32. Cabral, J. P. S., Water Microbiology. Bacterial Pathogens and Water. *Int. J. Environ. Res. Public Health* **2010,** *7* (10), 3657-3703.

33. Liang, B. Y.; Ju, Y.; Joubert, J. R.; Kaleta, E. J.; Lopez, R.; Jones, I. W.; Hall, H. K.; Ratnayaka, S. N.; Wysocki, V. H.; Saavedra, S. S., Label-free detection and identification of protein ligands captured by receptors in a polymerized planar lipid bilayer using MALDI-TOF MS. *Anal. Bioanal. Chem.* **2015,** *407* (10), 2777-2789.

34. Abbas, A.; Linman, M. J.; Cheng, Q. A., Patterned Resonance Plasmonic Microarrays for High-Performance SPR Imaging. *Anal. Chem.* **2011,** *83* (8), 3147-3152.

35. Wilkop, T.; Wang, Z. Z.; Cheng, Q., Analysis of mu-contact printed protein patterns by SPR imaging with a LED light source. *Langmuir* **2004,** *20* (25), 11141-11148.

36. Gasteiger, E.; Gattiker, A.; Hoogland, C.; Ivanyi, I.; Appel, R. D.; Bairoch, A., ExPASy: the proteomics server for in-depth protein knowledge and analysis. *Nucleic Acids Res.* **2003,** *31* (13), 3784-3788.

37. Bonnel, D.; Mehn, D.; Marchesini, G. R., Label-Free Biosensor Affinity Analysis Coupled to Mass Spectrometry. *Analyzing Biomolecular Interactions by Mass Spectrometry* **2015**, 299-316.

38. Ko, K. S.; Jaipuri, F. A.; Pohl, N. L., Fluorous-based carbohydrate microarrays. *J. Am. Chem. Soc.* **2005,** *127* (38), 13162-13163.

39. Srinivasan, U.; Houston, M. R.; Howe, R. T.; Maboudian, R., Alkyltrichlorosilane-based self-assembled monolayer films for stiction reduction in silicon micromachines. *J. Microelectromech. Syst.* **1998,** *7* (2), 252-260.

40. Merritt, E. A.; Sarfaty, S.; Vandenakker, F.; Lhoir, C.; Martial, J. A.; Hol, W. G. J., CRYSTAL-STRUCTURE OF CHOLERA-TOXIN B-PENTAMER BOUND TO RECEPTOR G(M1) PENTASACCHARIDE. *Protein Sci.* **1994,** *3* (2), 166-175.

41. Pukin, A. V.; Branderhorst, H. M.; Sisu, C.; Weijers, C. A. G. M.; Gilbert, M.; Liskamp, R. M. J.; Visser, G. M.; Zuilhof, H.; Pieters, R. J., Strong Inhibition of Cholera Toxin by Multivalent GM1 Derivatives. *ChemBioChem* **2007,** *8* (13), 1500-1503.

42. Šachl, R.; Amaro, M.; Aydogan, G.; Koukalová, A.; Mikhalyov, I. I.; Boldyrev, I. A.; Humpolíčková, J.; Hof, M., On multivalent receptor activity of GM1 in cholesterol containing membranes. *Biochimica et Biophysica Acta (BBA) - Molecular Cell Research* **2015,** *1853* (4), 850-857.

43. Sisu, C.; Baron, A. J.; Branderhorst, H. M.; Connell, S. D.; Weijers, C. A. G. M.; de Vries, R.; Hayes, E. D.; Pukin, A. V.; Gilbert, M.; Pieters, R. J.; Zuilhof, H.; Visser, G. M.; Turnbull, W. B., The Influence of Ligand Valency on Aggregation Mechanisms for Inhibiting Bacterial Toxins. *ChemBioChem* **2009,** *10* (2), 329-337.

44. Beddoe, T.; Paton, A. W.; Le Nours, J.; Rossjohn, J.; Paton, J. C., Structure, biological functions and applications of the AB(5) toxins. *Trends Biochem.Sci.* **2010,** *35* (7), 411-418.

45. Eidels, L.; Proia, R. L.; Hart, D. A., MEMBRANE-RECEPTORS FOR BACTERIAL TOXINS. *Microbiol. Rev.* **1983,** *47* (4), 596-620.

46. Law, K. Y., Definitions for Hydrophilicity, Hydrophobicity, and Superhydrophobicity: Getting the Basics Right. *J. Phys. Chem. Lett.* **2014,** *5* (4), 686-688.

47. Wang, H.-Y. J.; Liu, C. B.; Wu, H.-W., A simple desalting method for direct MALDI mass spectrometry profiling of tissue lipids. *J Lipid Res* **2011,** *52* (4), 840-849.

48. Weishaupt, N.; Caughlin, S.; Yeung, K. K. C.; Whitehead, S. N., Differential Anatomical Expression of Ganglioside GM1 Species Containing d18:1 or d20:1 Sphingosine Detected by MALDI Imaging Mass Spectrometry in Mature Rat Brain. *Front. Neuroanat.* **2015,** *9*, 11.

49. Jackson, S. N.; Wang, H. Y. J.; Woods, A. S., Direct profiling of lipid distribution in brain tissue using MALDI-TOFMS. *Anal. Chem.* **2005,** *77* (14), 4523-4527.

50. Abbas, A.; Linman, M. J.; Cheng, Q., Sensitivity comparison of surface plasmon resonance and plasmon-waveguide resonance biosensors. *Sens. Actuator B-Chem.* **2011,** *156* (1), 169-175.

51. Kuziemko, G. M.; Stroh, M.; Stevens, R. C., Cholera toxin binding affinity and specificity for gangliosides determined by surface plasmon resonance. *Biochemistry* **1996,** *35* (20), 6375-6384.

52. Page, A. L.; Alberti, K. P.; Mondonge, V.; Rauzier, J.; Quilici, M. L.; Guerin, P. J., Evaluation of a Rapid Test for the Diagnosis of Cholera in the Absence of a Gold Standard. *PLoS One* **2012,** *7* (5), 6.

53. Fono, L. J.; Sedlak, D. L., Use of the chiral pharmaceutical propranolol to identik sewage discharges into surface waters. *Environ. Sci. Technol.* **2005,** *39* (23), 9244-9252.

54. Ohtomo N Fau - Muraoka, T.; Muraoka T Fau - Tashiro, A.; Tashiro A Fau - Zinnaka, Y.; Zinnaka Y Fau - Amako, K.; Amako, K., Size and structure of the cholera toxin molecule and its subunits. (0022-1899 (Print)).

55. McDonnell, L. A.; Heeren, R. M. A., Imaging mass spectrometry. *Mass Spectrom. Rev.* **2007,** *26* (4), 606-643.

56. Abbady, A. Q.; Al-Daoude, A.; Al-Mariri, A.; Zarkawi, M.; Muyldermans, S., Chaperonin GroEL a Brucella immunodominant antigen identified using Nanobody and MALDI-TOF-MS technologies. *Vet. Immunol. Immunopathol.* **2012,** *146* (3-4), 254-263.

57. van Baar, B. L. M.; Hulst, A. G.; Wils, E. R. J., Characterisation of cholera toxin by liquid chromatography - Electrospray mass spectrometry. *Toxicon* **1999,** *37* (1), 85-108.

58. Jutla, A.; Khan, R.; Colwell, R., Natural Disasters and Cholera Outbreaks: Current Understanding and Future Outlook. *Current Environmental Health Reports* **2017,** *4* (1), 99-107.

59. Kundzewicz, Z. W.; Kanae, S.; Seneviratne, S. I.; Handmer, J.; Nicholls, N.; Peduzzi, P.; Mechler, R.; Bouwer, L. M.; Arnell, N.; Mach, K.; Muir-Wood, R.; Brakenridge, G. R.; Kron, W.; Benito, G.; Honda, Y.; Takahashi, K.; Sherstyukov, B., Flood risk and climate change: global and regional perspectives. *Hydrological Sciences Journal* **2014,** *59* (1), 1-28.

Chapter 3: Hybrid 3D printing and PDMS Molding Methodology for Polymer Prisms to enable High-Performing SPR Biosensing

3.1 Introduction

One of the most important innovations in the analytical sciences in recent years has been the rapid growth of three-dimensional (3D) printing. 3D printing has a number of important applications that are under heavy ongoing development in the analytical sciences.[1] While 3D printing has been known and demonstrated since at least the 1990s,[2] the expiration of patents in the last decade has led to high innovation for the printers themselves and, as a result, the applications that the process can be applied to.[3] 3D printing is an additive manufacturing technique that directly translates a digital design to a solid object by building it layer-by-layer, adhering each layer either by an adhesive in the build resin or by a UV laser polymerizing a photo-sensitive material, such as polyacrylic acid (PAA). A large portion of the analytical development around 3D printing takes advantage of the "rapid prototyping" and no geometrical constraints to prototype new microfluidic configurations for analytical and bioanalytical applications, as reported by many researchers.[4-6] At a broader level, 3D printing facilitates new instrumental configurations in the lab through the easy prototyping of simple structural components that can integrate multiple pieces in a custom-made process.[7-10]

Another important implementation of 3D printing for analytical sensing is in the manufacture of the optical components used in optical analyses. This has been enabled by the development of optically clear resins for 3D printing, and the ability to manufacture

custom components for individual applications allows for experimental setups that are not constrained by the availability of specific optical components. Instead, the optical system can be built to suit the analysis. However, while the potential resolutions of 3D printers have improved dramatically over the past two decades, with feature sizes as low 15 μm being reported in the literature with custom setups,[11, 12] the practical step height limits in commercial devices are on the order of 25 μm. This is in comparison to the surface roughnesses of optical quality SF2 and BK7 glasses, among others, which are typically < 2 nm. We have previously reported[13] the manufacture and use of 3D-printed optics for biosensing utilizing plasmonic techniques that overcome this challenge by a multi-step polishing method. Furthermore, there is another challenge to high-quality analytical optical applications with 3D resins, which is the refractive index of the polymers themselves. Higher-quality glasses such as SF2 have a refractive index of ~1.62, while the cured resin designed for 3D printers is ~1.45. This puts strains on optical configurations designed for higher-RI materials.

In this chapter, an alternative fabrication method is presented that takes advantage of the high curing smoothness available from polydimethylsiloxane (PDMS) to generate an even smoother and more repeatable set of polymer optics for SPR biosensing. PDMS is used broadly to make a variety of parts across the sciences, including masks, molds, and microfluidics, among many other components.[14-16] However, the malleability of cured PDMS renders it largely unusable for direct optical components. Here, PDMS molds were made of either already-smooth parts or of 3D printed pieces. Photopolymer resin, such as that used for 3D printing, could be poured into the mold and polymerized to the final optical

component geometry. The low surface roughness from the mold is transferred to the final prism, which could be used for highly-sensitive surface plasmon resonance (SPR) imaging. The surface roughness was reduced from ~12 nm with polishing to ~ 4 nm with the hybrid method, presenting the additional benefit of removing polishing requirements and homogenizing the preparation. Traditional 3D printing resin was found to have significant morphological challenges in bulk polymerization, so an alternate photopolymer was substituted. The analytical performance of the prisms towards plasmonic sensing was characterized and the results showed a highly sensitive measurement, both for bulk refractive index testing and for the detection of environmental pathogen cholera toxin (CT). Multiple benefits of the flexibility and ease of manufacture of the polymer prisms were demonstrated, as the prism itself could be patterned by a 3D-printed mask and used disposably, and chemical additives could be incorporated into the process to alter the optical properties of the generated prism components. This hybrid methodology should serve to widen the space of possibilities offered towards optical analysis by 3D printing.

3.2 Experimental Methods

Materials and Reagents. Chromium and gold targets for electron beam physical vapor deposition (EBPVD) were obtained as pellets of 0.9999% purity from Kurt J. Lesker (Jefferson Hills, PA). Sodium chloride, sucrose, and streptavidin protein were obtained from ThermoFisher Scientific (Pittsburgh, PA). BK-7 glass substrates for Electron-beam deposition were obtained from Corning (Painted Post, NY). 1-Palmitoyl-2-oleoyl-glycero-3-phosphocholine (POPC) was obtained from Avanti Polar Lipids (Alabaster, AL), and monosialoganglioside (GM1) was obtained from Matreya (Pleasant Gap, PA). 1-ethyl-3-

(3-dimethylaminopropyl)carbodiimide (EDC) and N-hydroxylsuccinimide (NHS) were purchased from Chem Impex (Wood Dale, Il). Cholera toxin (CT) and anti-CT antibodies were obtained from Sigma-Aldrich (St. Louis, MO). PDMS was obtained as Sylgard 184 Silicone Elastomer Kit from Ellsworth Adhesives (Germantown, WI). PEG-thiol and biotin-PEG-thiol were obtained from Nanocs (New York, NY).

Thin-films and lithography for SPR substrates. Electron beam physical vapor deposition (EBPVD) (Temescal, Berkeley, CA) was used to deposit 2 nm Cr films followed by 50 nm Au films. All EBPVD was conducted in a Class 1000 cleanroom facility (UCR Center for Nanoscale Science and Engineering). The prisms were stored in a desiccator in room temperature before use. Conventional SPR and SPR imaging substrates were fabricated with BK-7 glass microscope slides that were cleaned with boiling piranha solution (3:1 H_2SO_4:30% H_2O_2) for 1 hr then rinsed with ultrapure water and ethanol and dried with compressed air. For conventional SPR chips, similar 2/50 nm Cr/Au was deposited with EBPVD as described above.

Microarray substrates used in conjunction with molded prisms for SPR imaging were fabricated according to a previously reported procedure with some modification.[17, 18] In brief, piranha-cleaned glass slides were spin-coated at 4000 RPM for 45 s with hexamethyldisilazane (HMDS) and AZ5214E in succession, followed by a 1 min bake at 110 ° C. Photopatterning via UV exposure was conducted with a photomask and Karl-Suss MA-6 system followed by AZ400K development using standard protocols. 2/200 nm Cr/Au were deposited via EBPVD, followed by removal of wells with acetone. Finally, an

additional deposition of 2/50 nm of Cr/Au was added to form the plasmonically active wells, generating a 10 × 12 microarray of 600 μm diameter circular wells.

Atomic Force Microscopy and Ellipsometry. For molded prisms, AFM measurements were obtained using a LabRam/AIST-NT AFM (Horiba Scientific, Palaiseau, France). Data was acquired in tapping mode using a 42 N/m tip from NanoWorld. All AFM data was plotted and calculated using Gwyddion 2.59 software. Ellipsometry measurements were conducted on a UVISEL M200 (Horiba Jobin Yvon, France).

Digital Component Design and 3D printing. The 3D models of the prisms were designed by SketchUp software (Trimble, Inc., Sunnyvale, CA). A Formlabs Preform software was used to upload the 3D models to a commercial 3D stereolithography printer, Formlabs Form 3 (Somerville, MA) for a rapid prototyping process. Specifically, a compact system of lenses and mirrors were integrated in the Light Processing Unit (LPU) within the printer and a 250 mW UV laser power was used for accurate prints (XY Resolution: 25 μm). The cured prisms were placed in an isopropanol bath for 20 min and washed by isopropanol one more time before dried by compressed air. A CL-1000 UV crosslinker (UVP Inc., Upland, CA) was then applied to post-cure the prisms for 1.5 h.

PDMS Molding and Polymer Prism Manufacture. To generate PDMS mold, elastomer base and curing agent were thoroughly mixed in a 10:1 w/w ratio, respectively, then degassed in vacuum for 30 min. A BK7 prism (surplusshed.com) was placed in a small truncated-conical plastic container, followed by pouring of the mixture around the prism. After an additional 30 min of degassing, the assemblage was placed in a 100 ° C oven for

2 hr to harden. The prism was removed, followed by pipetting of photopolymer resin and polymerization with no further degassing in a UV Crosslinker oven, either CL-1000L (365 nm) or CL-1000S (254 nm).

SPR and SPR imaging analysis. For conventional SPR experiments, a dual-channel NanoSPR6-321 spectrometer (NanoSPR, Chicago, Il) was utilized, which included a GaAs semiconductor laser light source (λ = 670 nm), a 30 μL flow cell, and a manufacturer-supplied prism of high refractive index (n = 1.616). Online experiments were conducted in angular scanning mode. SPR imaging measurements were conducted on a home-built device, a detailed description of which can be found in previous reports.[17, 19] Briefly, each substrate microarray was mounted onto a 3D-printed optical stage, and matching fluid mediated contact with an equilateral prism composed of either PDMS-molded polymer or SF2 glass (n = 1.648) depending on the experiment, along with a 300 μL flow cell. The optical stage was fixed atop a goniometer that could be manually rotated to tune the incident angle of an incoherent light emitting diode (LED) source of 648 nm that initiated SPR excitation across the microarray. Reflected images were captured with a cooled 12-bit CCD camera (QImaging Retiga 1300) with a resolution of 1.3 MP (1280 × 1024 pixels) and 6.7 μm × 6.7 μm pixel size. Online experiments were conducted by recording change in reflectance in individual wells every 300 ms during injection and incubation of analyte solutions. Intensity data was normalized by dividing the intensity of p-polarized light by the intensity generated by s-polarized light and multiplying by 100 to generate a percentage value, and percent intensity values are reported as the average of at least 15 individual wells. Solutions of NaCl and sucrose for bulk sensitivity testing were

diluted with ultrapure water and respective refractive indices were measured with an Abbe refractometer (American Optics, Buffalo, NY). Membranes used in SPR and SPRi CT biosensing experiments were composed of POPC and GM1 (5% molar weight) and were generated by mixing the lipids and drying in nitrogen and placing under vacuum for 4 hr, followed by sonication and extrusion into 100 nm lipid vesicles (Whatman 100 nm membrane filters).

UV-Vis Spectra. Visible-range transmission spectra for the hemicylindrical prisms with dye additives were obtained using a previously reported SPR transmission setup with some modification.[20] A home built optical stage held the flat prism face perpendicular to the incident light source and collector. White light was generated from a HL2000 tungsten-halogen lamp, transmitted light was collected with a USB2000+VIS-NIR-ES spectrometer, and signal through 200 μm optical fibers (all components from Ocean Optics, Dunedin, Fl).

3.3 Results and Discussion

PDMS Molding of Conventionally Fabricated Components. To determine the feasibility of PDMS molds being an appropriate strategy for generating smooth polymer prism surface, the initial investigation was conducted by molded around commercially purchased 25 mm equilateral prisms. This was due to the prisms already been conventionally grinded to an optically smooth level, and in principle, any smooth enough surface of the appropriate geometry could take advantage of the following methodology. First, pre-polymerized PDMS was poured around the prism in a disposable container. After thermal curing of the mold, the prism was removed, leaving a clear equilateral mold (Figure

3.1a). The new mold was with the 3D printing resin, FormLabs Clear, and the combination was photocured in a UV oven, after which the resulting prism was removed and analyzed or used for analysis. The final polymer prisms retained good clarity compared to the glass part (see Figures 3.1b-d) and the procedure was extremely simple and repeatable. The primary benefits of this method are two-fold. First, the surface roughness would potentially be much lower than what can be accomplished via the polishing. While some loss of smoothness can be expected across the multiple steps of the procedure, the final product still retains a significant reduction than the polishing. This, in turn, leads to the second benefit of not requiring the post-processing steps that can complicate the overall process and lead to heterogenous preparations, such as polishing by hand.

Initial prisms made via this method using the FormLabs Clear resin had significant practical challenges. The final prisms, while hard, retained a "sticky" texture even after additional polymerization, and the surface was significantly bowed inward and visibly textured (Figure 3.1b). After the additional step of drop-casting more resin, leveling with microscope slips and a further 1 hr of polymerization, the prisms could be mounted onto the spectroscopy setup for data acquisition in further sections. However, an alternative was sought in the form of photocurable adhesive Norland 61 (N61). The N61 polymer was similarly cured in the PDMS molds and resulted in a much more visually even and hard final component (Figure 3.1c), and though it is classified as an adhesive, no significant adhesion to the PDMS was found after photopolymerization. Though the composition of the FormLabs resin is proprietary, this effect is potentially due to the resin being used differently than intended. The polymerization depth of penetration required on the build

platform is on the order of ~100 μm, the typical largest step size of the printer. Lower penetration depth can more easily lead to regions of heterogeneity or incomplete polymerization. Multiple polymerization wavelengths were also considered in the curing step, and both for the FormLabs and Norland resins, significant differences were observed in the final prisms based on the wavelength used. With a 254 nm curing wavelength, the Formlabs resin was as described above, but with a 365 nm oven, the prism was significantly yellowed and developed a "splatter" pattern on multiple faces (Figure 3.1e). For the N61 resin, switching to the 365 nm oven for curing resulted in a "bubbling" pattern at the top edges of the faces (Figure 3.1f).

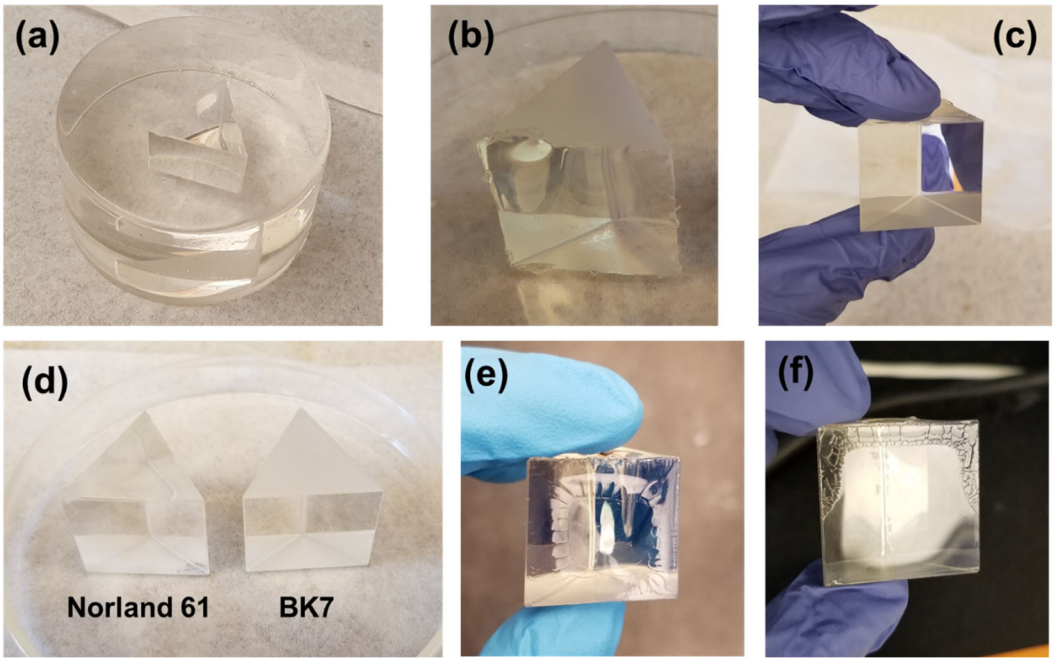

Figure 3.1. Prism molding process. (a) PDMS mold after curing and removal of original glass part. (b) FormLabs Clear molded prism. (c) Norland 61 molded prism. (d) Norland 61 prism next to conventional BK7 prism. (e) FormLabs Clear and (f) Norland 61 molded prisms cured with 365 nm oven.

The reuse of the PDMS molds would be a highly beneficial trait in practice. However, trace amounts of resin remained on the PDMS mold walls after removal of the prisms. As such, we implemented a cleaning step for the reuse of the mold that used strong base, which efficiently degrades both the crosslinking agents and base mercapto-ester components of the Norland photopolymer.[21] Used molds were immersed in a solution of ~1 M potassium hydroxide diluted in isopropanol for 2 minutes followed by rinsing with DI H_2O and drying with N_2. We found this method to reproduce clear and smooth prisms for up to five uses of a given mold.

Surface Characterization. Though the polymer prisms themselves had many visually observable differences in morphology and clarity, a more quantitative assessment was additionally pursued via atomic force microscopy (AFM). Micrographs of the polished and unpolished 3D printed prism, the prism-face of the PDMS mold surface, and the molded Norland61 prism, along with a summary comparison of RMS roughnesses, are shown in Figure 3.2. As expected, the native 3D-printed part surface was very uneven and had a high surface roughness of 78 nm. This is improved significantly by polishing via the previously reported procedure, down to 12 ± 2.8 nm. However, both stages of the hybrid molding process have significantly lower surface roughnesses. The PDMS mold, being the initial step, is the lower of the two, with R_{rms} = 2.8 ± 0.6 nm. This approaches the smoothness of commercially available polished glass (1-2 nm), and indicates that the mold effectively retains the surface quality of the initial BK7 part. The Norland 61 prism is slightly higher, with R_{rms} = 4.6 ± 0.9 nm, though this still indicates smoothness effectively transfers across steps and that the minor manual step of removing the polymer prism from

the mold did not significantly affect the final quality. Additionally, the variability as given by the measurement standard deviation of the polished prisms (2.8 nm) is ~300% higher than that of the molded prisms (0.9 nm). This supports the likelihood that removing the need for manual repetitive procedures such as polishing leads to a more consistent final surface state. The surface roughness of the Norland prism after repeated reuse of the PDMS mold was also measured to test the efficacy of the cleaning procedure. The average R_{rms} increased to 20 nm ± 2.7 nm, indicating a good retention of clarity and usability in the part, though perhaps also an area of potential future development and improvement.

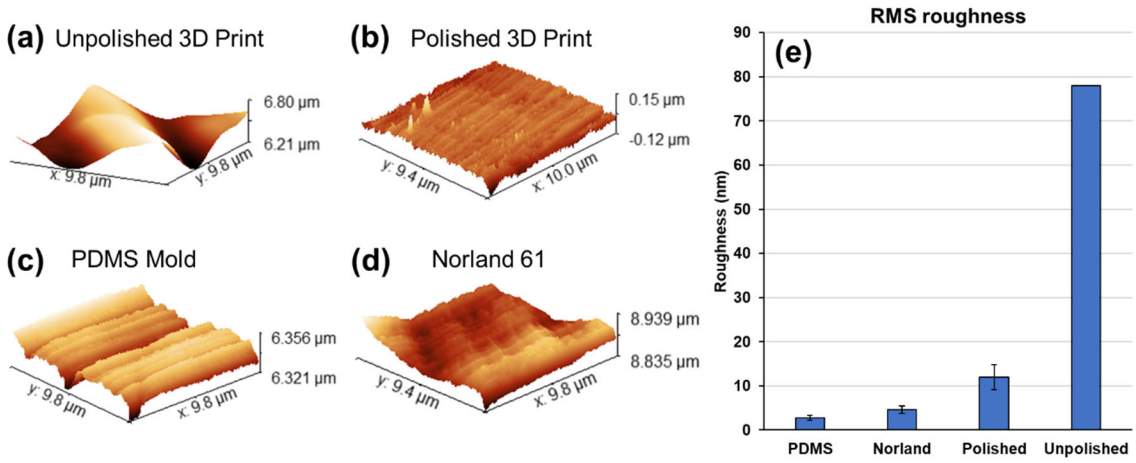

Figure 3.2. AFM micrographs of (a) unpolished and (b) 3D-printed prism surfaces, (c) the prism face surface of the PDMS mold, and (d) the face of a molded Norland 61 polymer prism. (e) Bar chart summary of the RMS roughness of each surface.

SPR-based analytical performance. Actual optical performance of the prisms in an analytical setting was conducted with the standard optical technique of SPR imaging, which uses equilateral prisms as an optical coupler to excite surface plasmons at a surface interface and thus analyze interactions at the surface. Compared to conventional SPR, SPR

imaging is a more comprehensive test method for the polymer prisms due to the need for consistent optical signal across the whole image and analysis surface. SPR imaging typically uses arrays or large regions of interest which must be compared spatially, as opposed to conventional SPR which only requires individual analysis spots. Here, we used a microarray substrate that we have previously reported with 50 nm Au wells and 200 nm Au walls to damp the plasmonic response in all regions except the wells,[17] incorporated into a home-built SPR imaging setup.

Array images taken after loading the substrate onto the polymer prisms, attachment of the flowcell, and flowing of 1 x PBS running buffer is shown in Figures 3.3a and 3.3b. The morphological features affecting the imaging of the FormLabs clear resin prisms are visually apparent, but more specifically, an important potential challenge that has been reported for bulk polymerization of photopolymers for optics is the presence of birefringence. In this scenario, incoming light passes through an anisotropic region where the polymer is not well ordered, and splits into multiple polarized components. This would be a particular difficulty for SPR-based applications, as the resonant absorption by the plasmonic metal at the interface is highly dependent on light being p-polarized relative to the surface. Polarization filters are utilized in this and other SPR imaging setups to restrict the incident light to p-polarized light that can be absorbed, as s-polarized light functions essentially as background signal. Thus, birefringence in the imaging would be marked by regions of significantly higher overall brightness, rendering them incomparable to other regions and unusable. This effect can be seen in the FormLabs resin-based prism (Figure 3.3a) but is essentially non-existent from the Norland-based prisms (Figure 3.3b).

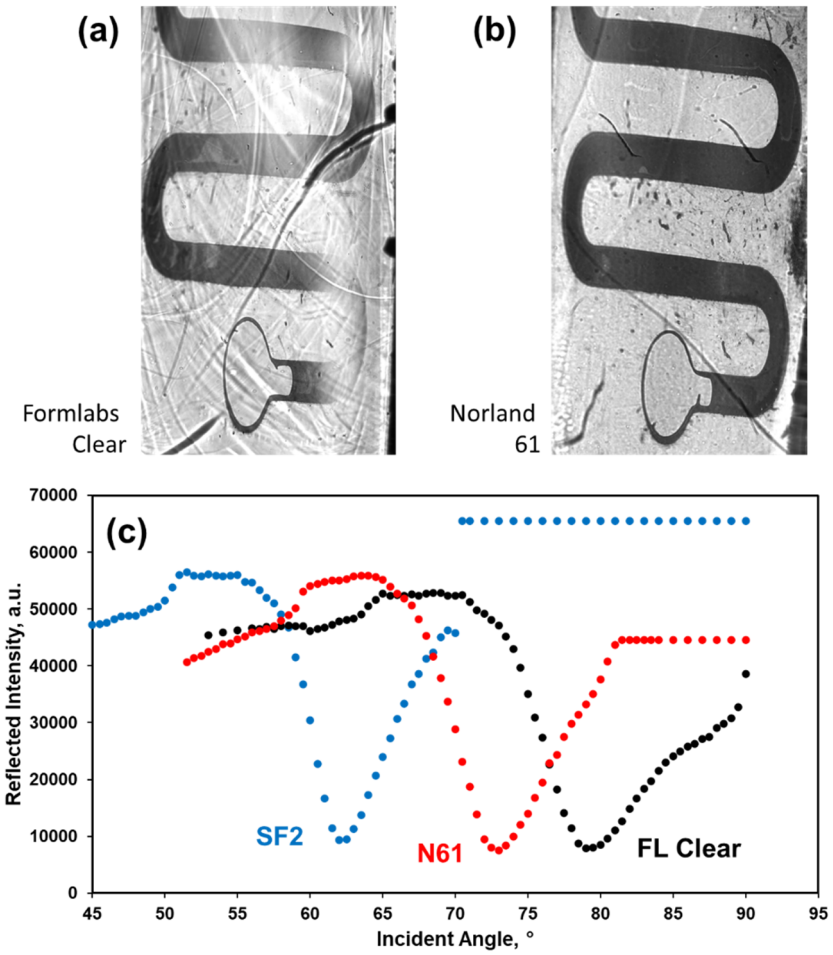

Figure 3.3. SPR images of unpatterned Al film substrate with (a) FormLabs Clear and (b) Norland 61 molded prisms. (c) SPR imaging reflectivity curves comparing molded prisms and conventional SF2 prism.

Another important aspect to consider is the overall refractive index of the cured polymer. Higher refractive indices are generally preferred in spectroscopic applications, and in the case of SPR imaging, lower refractive index generates a more warped image, as the incident angle is further from perpendicular to the plane of the array chip. Full reflectivity spectra of the FormLabs, N61, and conventional SF2 prisms are shown in Figure 3.3c which gives minimum reflectivity angles (a.k.a SPR angles) of 79 °, 73 ° and 62.5 °, respectively. Additionally, the morphological challenge of the FormLabs clear

prism was reflected in the actual optical data, as the plasmonic dip was broader and slightly misshapen, compared to that of the N61 and SF2 prisms.

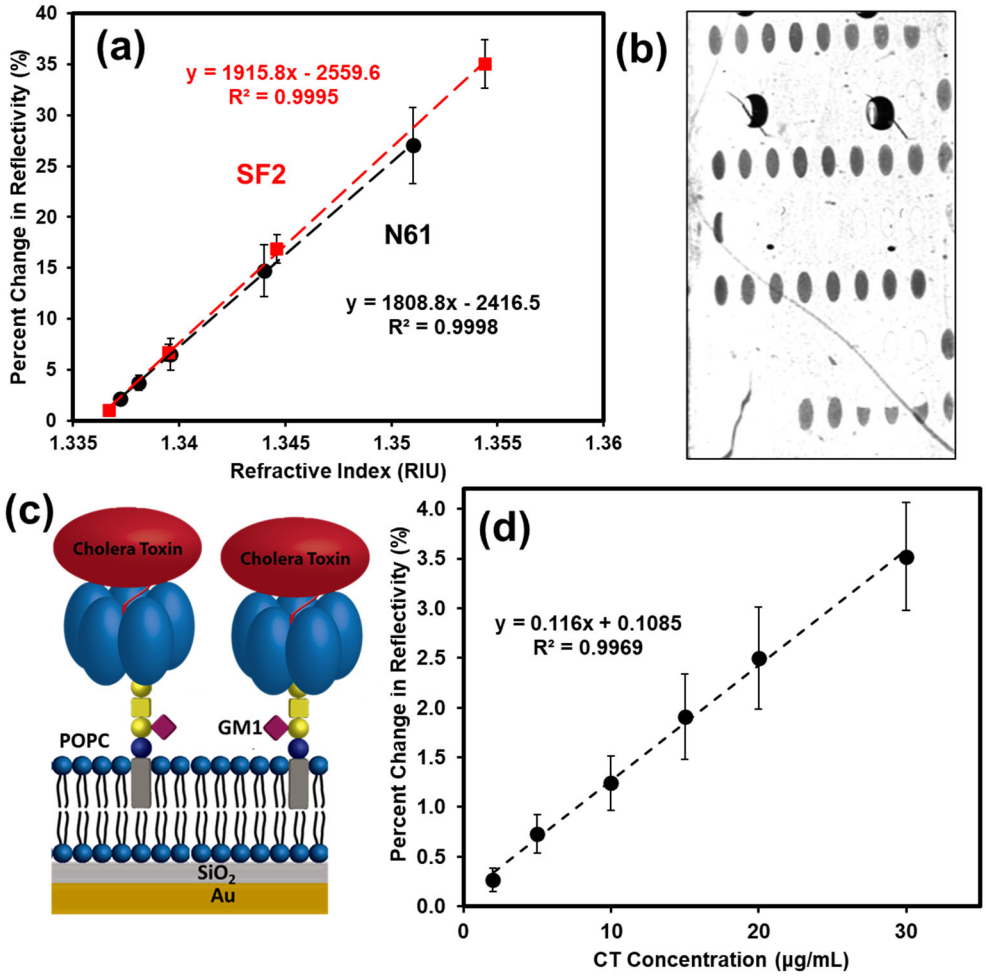

Figure 3.4. Polymer prism analytical performance. (a) Bulk SPR imaging sensitivity comparison for N61 molded prism and conventional SF2 prism. (b) SPR online array image. (c) Biosensing scheme diagram, with CT binding to GM1 embedded in a POPC supported lipid bilayer. (d) Calibration curve of CT sensing.

Calibration curves of the bulk refractive index for both the polymer prism and a conventionally-fabricated SF2 prism are shown in Figure 3.4a, which show almost identical performance towards the plasmonic response to refractive index shifts. The well-to-well variation remained small, further reinforcing the minimal impact of birefringence

on the performance with the Norland polymer prism. A fuller incorporation of the polymer prisms into a biosensor was conducted via the quantification of cholera toxin (CT), an important environmental pathogenic protein produced by *Vibrio cholerae.* A scheme of the experimental setup is shown in Figure 3.4c and utilizes the strong binding and specificity of CT towards monosialoganglioside (GM_1). While some previous work coupled the GM1 lipid to the surface via fluorinated hydrocarbons, here the GM_1 lipids were incorporated into a biomimetic lipid membrane, an increasingly popular form of surface analysis. Incubation of the membrane produced a consistent binding shift across the wells, showing little variation from the polymer prism. A calibration curve of CT concentration versus optical response is given in Figure 3.4d that shows consistent linear response with a 3σ limit of detection of 1.1 μg/mL or 13 nM, on par with previous reports.[22, 23] This indicates the polymer prisms can easily be inserted into current biosensing and detection schemes with no loss in performance or sensitivity.

3D-printed mask for direct Au deposition. An additional benefit of the ease of fabrication is the polymer prisms is their disposability. As reported in previous work, gold films may be evaporated directly onto the prisms, removing the need for matching fluid and reducing the mechanical integration steps in the optical setup. Here, this process was further developed by the addition of another 3D designed and printed component, a deposition mask, as shown in Figure 3.5. 50 nm of Au was evaporated with the mask held in place over the surface to generate plasmonically-sensitive well spots directly onto the prism. After loading the prism into the SPR imaging setup and placement of the flowcell directly onto the prism surface, images, reflectivity curves, and bulk refractive index

sensitivity were obtained similar to previous. Notably, there was loss in visual fidelity in the images. This is likely due to small variations in the prism surface that are filled in with matching fluid when a separate chip substrate is mounted onto the prism. Reflectivity curves (Figure 3.5c) show an effective dip on the visible wells that is only ~2 ° shifted from the chip-based dip, and the RI sensitivity (Figure 3.5d) is 93% that of the chip-based setup (1690 vs 1810 %/RIU, respectively).

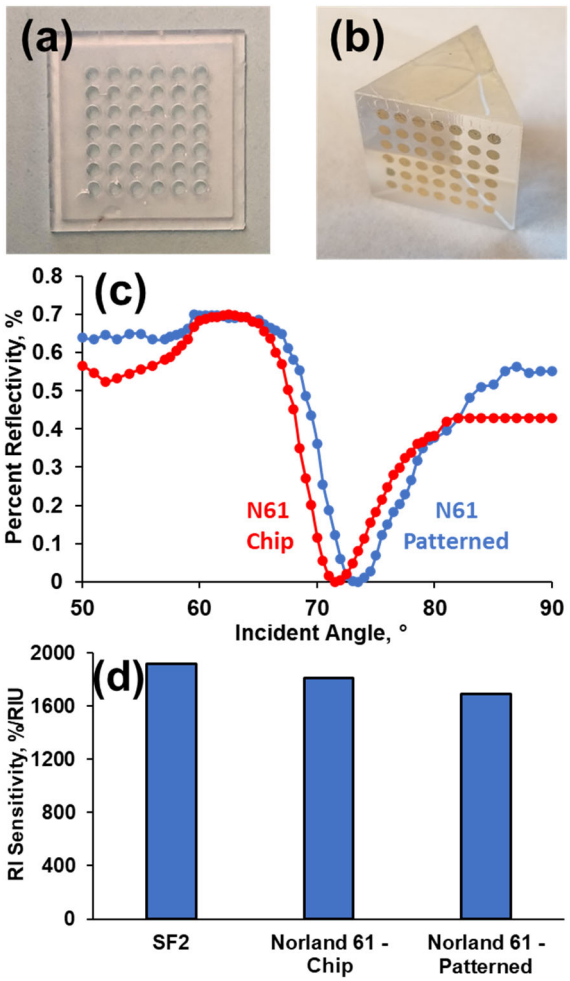

Figure 3.5. 3D-printed mask for direct Au deposition. Images of (a) printed mask and (b) N61 molded prism after 50 nm Au deposition using mask. (c) SPR imaging reflectivity curves of patterned prism and prism used with chip substrate. (d) Comparison of bulk refractive index sensitivities of both to conventional SF2 prism.

PDMS Molding of 3D-printed components. Finally, we sought to integrate the 3D printing of parts of higher geometrical difficulty. While a simple equilateral prism is easy to obtain as an already-smooth surface, a rounded prism is significantly higher cost to produce conventionally due to the rounded surface. This demonstrates the geometrical flexibility of 3D printing, as the layer-by-layer style of additive manufacturing has few specific barriers to any contiguous shape. Two components were initially tested by this method: 1) a hemispherical prism (Figure 3.6e) and a 2) hemicylindrical prism (Fig 6f). The prisms were designed in-software and 3D printed with standard settings. Tough resin (blue) rather clear resin was used, as the initial shaping piece had no requirement of transparency. Identical steps were taken for the initial PDMS molding, but key to this method is a further smoothing step with uncured PDMS and a spin-coater. After the PDMS mold was formed and the 3D printed part removed, cloudiness remains in the mold surface (Figure 3.6c) that was representative of the resolution of the 3D printer. A few drops (~0.5 mL) of additional uncured PDMS were dropped evenly along the center of mold shape, followed by a spin coating of 4000 rpm for 60 s. The smoothed mold was allowed to cure at 100 ° C for 1 hr in an inverted position so that uncured PDMS would not pool. The final rounded mold (Figure 3.6d) was optically clear and immediately usable for the photocurable polymers, which resulted in prisms (Figure 3.6e) of high clarity and usability in further aims. A typical price for a round prism is $100-200 USD, while the printed and molded component is < $1 of polymer material and only ~ 2 hr of significantly lower technically intensive work time by the user.

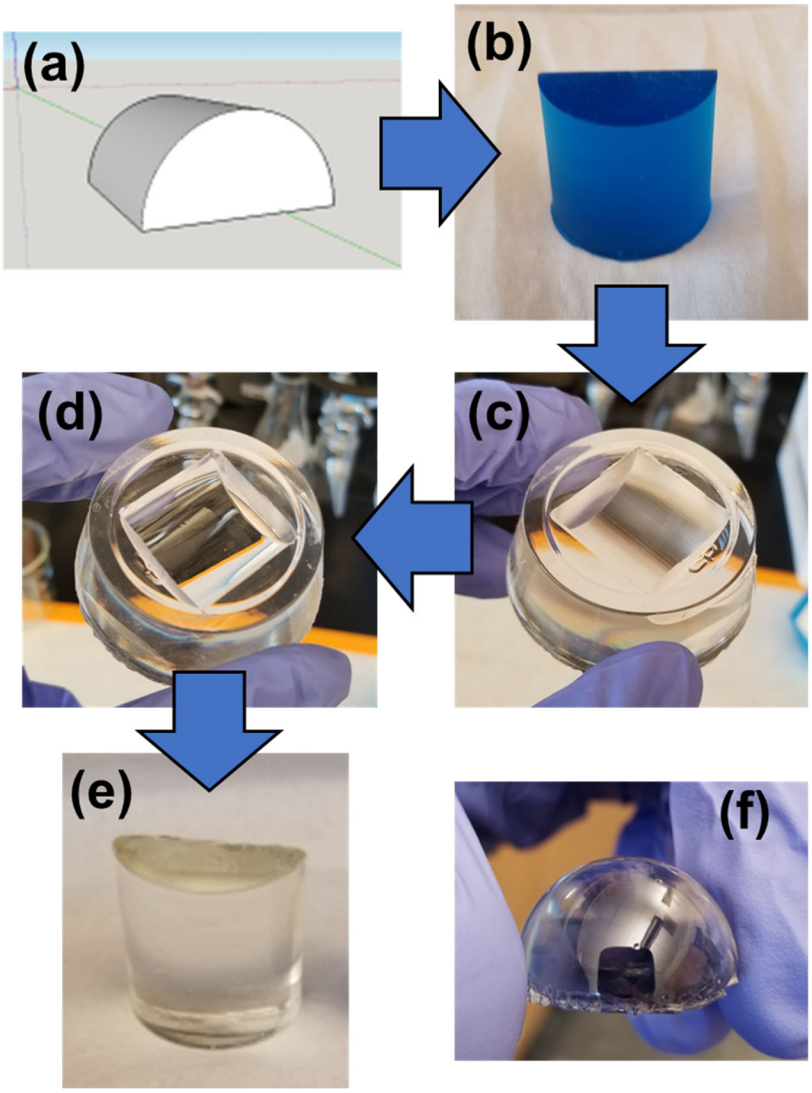

Figure 3.6. Polymer molding of 3D printed parts. A (a) software-designed part is (b) 3D printed, followed by (c) PDMS molding and removal of 3D part, then (d) smoothing with additional PDMS spincoating, and molding of (e) final hemicylindrical polymer prism. (f) A hemispherical prism made with the same process.

Resin Additives for Property Modification. A benefit of the mold-based form of fabrication for the final optical component is that additives can be more easily included in the process that alter the component's optical properties. This concept has been reported in the 3D printing of glass parts,[24-27] but the complexity of the 3D printing process is a

challenge. As seen with the bulk polymerization of the 3D printing resin, the 3D printing process is delicate and fined-tuned such that minor variations in the resin can result in large changes in the final product. As such, introduction of additives is impractical in the hardware itself without using an entirely home-built instrument and resin combination. Here, the step that creates the final component part is separated from the 3D printing step, opening up the possibility of including additives. This concept was demonstrated here by the addition of colored dyes to aliquots of the Norland resin, followed by photocuring using the smoothed hemicylindrical prism mold. Manufactured prisms showed good visual clarity (Figure 3.7a) and were able to be used in a transmission-based spectroscopic configuration (Figures 3.7b,c). Visible-range spectra for the "blue" prism are shown in Figure 3.7d, which show the prism having clean absorbances and effectively acting as a basic color filter. The capability for this functionality to be easily included in the fabrication of the optics itself, rather than with an additional color filter component, furthers the potential for in-lab custom part creation.

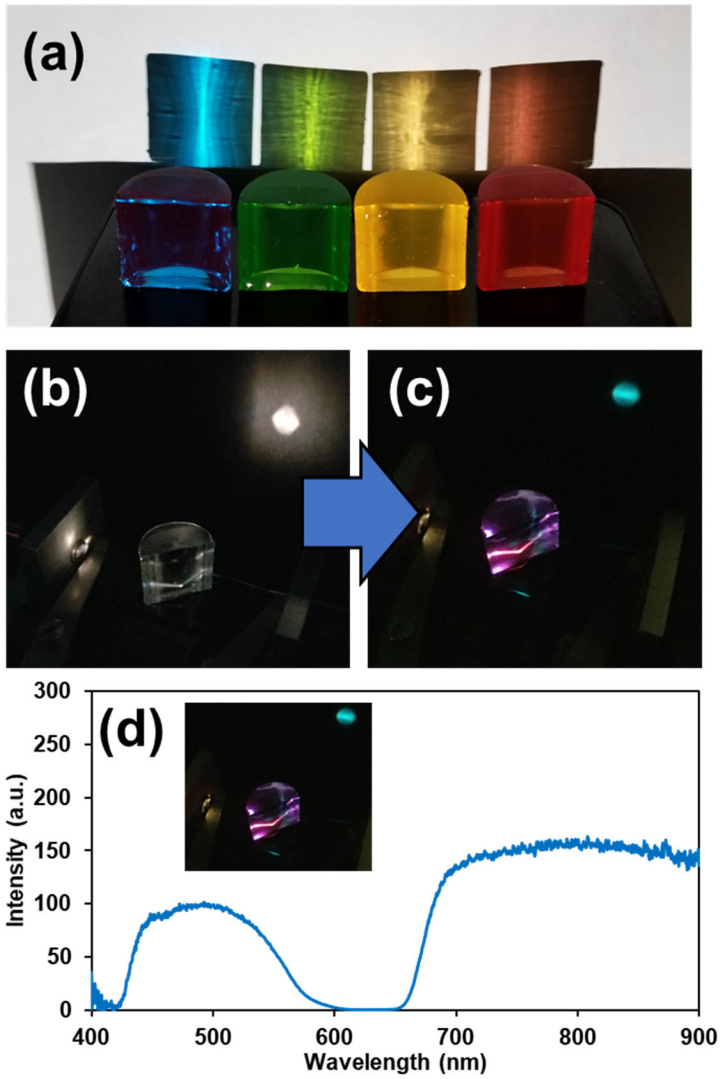

Figure 3.7. Additive-modified hemicylindrical molded prisms. (a) Variety of fabricated dyed prisms color-filtering incident white light. Total internal reflection with (b) unchanged and (b) "blue" prism. (c) Transmission spectra of blue prism.

3.4 Conclusion

In summary, we have demonstrated an alternative methodology for fabrication of ultrasmooth optical components for analytical spectroscopy. A PDMS mold of sufficient smoothness can be made of appropriate geometry as the final optical component. This can

be accomplished simply by molding a conventionally fabricated glass prism or other smooth object, or by 3D printing an optical component shape and molding it, followed by smoothing with spin-coating. This method overcomes the limitations of surface roughness and refractive index seen in previous reported methods while maintaining the space of geometrical possibility inherent in 3D printing. Of note is that the bulk polymerization of the FormLabs Clear photopolymer in the mold was found to require the use of an alternate material (Norland 61) that was more suited to the application. The analytical performance, both in basic bulk optical behavior and in a more complex biosensing scheme, was found to be of the same high quality as conventionally manufactured parts, even with the delicate and highly sensitive SPR imaging technique. Furthermore, a concept of a fully 3D printed package was developed with the addition of a 3D printed mask that generated a plasmonic array, creating a custom optical configuration that was completely disposable. Finally, the flexibility of the methodology was demonstrated by the incorporation of dye additives that shifted the transmission of incident white light in a visible-range transmission-based spectroscopy setup. This methodology is an important step in the development of facile means of custom optical component fabrication.

3.5 References

1. Lambert, A.; Valiulis, S.; Cheng, Q., Advances in Optical Sensing and Bioanalysis Enabled by 3D Printing. *ACS Sensors* **2018,** *3* (12), 2475-2491.

2. Crump, S. S. Apparatus and method for creating three dimensional objects. US5121329 A, 1992.

3. Fan, D. Y.; Li, Y.; Wang, X.; Zhu, T. J.; Wang, Q.; Cai, H.; Li, W. S.; Tian, Y.; Liu, Z. J., Progressive 3D Printing Technology and Its Application in Medical Materials. *Front. Pharmacol.* **2020,** *11*, 12.

4. Wang, L. J.; Pumera, M., Recent advances of 3D printing in analytical chemistry: Focus on microfluidic, separation, and extraction devices. *Trac-Trends Anal. Chem.* **2021,** *135*, 10.

5. Au, A. K.; Bhattacharjee, N.; Horowitz, L. F.; Chang, T. C.; Folch, A., 3D-printed microfluidic automation. *Lab Chip* **2015,** *15* (8), 1934-1941.

6. Carrasco-Correa, E. J.; Simó-Alfonso, E. F.; Herrero-Martínez, J. M.; Miró, M., The emerging role of 3D printing in the fabrication of detection systems. *TrAC Trends in Analytical Chemistry* **2021,** *136*, 116177.

7. Cevenini, L.; Calabretta, M. M.; Tarantino, G.; Michelini, E.; Roda, A., Smartphone-interfaced 3D printed toxicity biosensor integrating bioluminescent "sentinel cells". *Sensors and Actuators B-Chemical* **2016,** *225*, 249-257.

8. Wang, Y. J.; Zeinhom, M. M. A.; Yang, M. M.; Sun, R. R.; Wang, S. F.; Smith, J. N.; Timchalk, C.; Li, L.; Lin, Y. H.; Du, D., A 3D-Printed, Portable, Optical-Sensing Platform for Smartphones Capable of Detecting the Herbicide 2,4-Dichlorophenoxyacetic Acid. *Analytical Chemistry* **2017,** *89* (17), 9339-9346.

9. Bayram, A.; Serhatlioglu, M.; Ortac, B.; Demic, S.; Elbuken, C.; Sen, M.; Solmaz, M. E., Integration of glass micropipettes with a 3D printed aligner for microfluidic flow cytometer. *Sens. Actuator A-Phys.* **2018,** *269*, 382-387.

10. Mendoza-Gallegos, R. A.; Rios, A.; Garcia-Cordero, J. L., An Affordable and Portable Thermocycler for Real-Time PCR Made of 3D-Printed Parts and Off-the-Shelf Electronics. *Analytical Chemistry* **2018,** *90* (9), 5563-5568.

11. Sanchez Noriega, J. L.; Chartrand, N. A.; Valdoz, J. C.; Cribbs, C. G.; Jacobs, D. A.; Poulson, D.; Viglione, M. S.; Woolley, A. T.; Van Ry, P. M.; Christensen, K. A.; Nordin, G. P., Spatially and optically tailored 3D printing for highly miniaturized and integrated microfluidics. *Nat. Commun.* **2021,** *12* (1), 5509.

12. Gong, H.; Bickham, B. P.; Woolley, A. T.; Nordin, G. P., Custom 3D printer and resin for 18 mu m x 20 mu m microfluidic flow channels. *Lab Chip* **2017,** *17* (17), 2899-2909.

13. Hinman, S. S.; McKeating, K. S.; Cheng, Q., Plasmonic Sensing with 3D Printed Optics. *Analytical Chemistry* **2017,** *89* (23), 12626-12630.

14. Kim, P.; Kwon, K. W.; Park, M. C.; Lee, S. H.; Kim, S. M.; Suh, K. Y., Soft lithography for microfluidics: a review. *BioChip J.* **2008,** *2* (1), 1-11.

15. Raj, M. K.; Chakraborty, S., PDMS microfluidics: A mini review. *JOURNAL OF APPLIED POLYMER SCIENCE* **2020,** *137* (27).

16. Waheed, S.; Cabot, J. M.; Macdonald, N. P.; Lewis, T.; Guijt, R. M.; Paull, B.; Breadmore, M. C., 3D printed microfluidic devices: enablers and barriers. *Lab Chip* **2016,** *16* (11), 1993-2013.

17. Abbas, A.; Linman, M. J.; Cheng, Q. A., Patterned Resonance Plasmonic Microarrays for High-Performance SPR Imaging. *Analytical Chemistry* **2011,** *83* (8), 3147-3152.

18. Malinick, A. S.; Lambert, A. S.; Stuart, D. D.; Li, B. C.; Puente, E.; Cheng, Q., Detection of Multiple Sclerosis Biomarkers in Serum by Ganglioside Microarrays and Surface Plasmon Resonance Imaging. *Acs Sensors* **2020,** *5* (11), 3617-3626.

19. Wilkop, T.; Wang, Z. Z.; Cheng, Q., Analysis of mu-contact printed protein patterns by SPR imaging with a LED light source. *Langmuir* **2004,** *20* (25), 11141-11148.

20. Tran, K. Development of Nanofiber and Surface Plasmon Resonance Sensors for VOCs, Biochemical, and Bacterial Analysis. University of California - Riverside, Riverside, CA, USA, 2020.

21. Norland Optical Adhesive 61. Norland Products Inc: Cranbury, NJ.

22. Hinman, S. S.; McKeating, K. S.; Cheng, Q., DNA Linkers and Diluents for Ultrastable Gold Nanoparticle Bioconjugates in Multiplexed Assay Development. *Analytical Chemistry* **2017,** *89* (7), 4272-4279.

23. Hinman, S. S.; Ruiz, C. J.; Cao, Y.; Ma, M. C.; Tang, J.; Laurini, E.; Posocco, P.; Giorgio, S.; Pricl, S.; Peng, L.; Cheng, Q., Mix and Match: Coassembly of Amphiphilic Dendrimers and Phospholipids Creates Robust, Modular, and Controllable Interfaces. *ACS Appl Mater Interfaces* **2017,** *9* (1), 1029-1035.

24. Kotz, F.; Arnold, K.; Bauer, W.; Schild, D.; Keller, N.; Sachsenheimer, K.; Nargang, T. M.; Richter, C.; Helmer, D.; Rapp, B. E., Three-dimensional printing of transparent fused silica glass. *Nature* **2017,** *544* (7650), 337-339.

25. Cooperstein, I.; Shukrun, E.; Press, O.; Kamyshny, A.; Magdassi, S., Additive Manufacturing of Transparent Silica Glass from Solutions. *Acs Applied Materials & Interfaces* **2018,** *10* (22), 18879-18885.

26. Destino, J. F.; Dudukovic, N. A.; Johnson, M. A.; Nguyen, D. T.; Yee, T. D.; Egan, G. C.; Sawvel, A. M.; Steele, W. A.; Baumann, T. F.; Duoss, E. B.; Suratwala, T.; Dylla-Spears, R., 3D Printed Optical Quality Silica and Silica-Titania Glasses from Sol-Gel Feedstocks. *Adv. Mater. Technol.* **2018,** *3* (6), 1700323.

27. Nguyen, D. T.; Meyers, C.; Yee, T. D.; Dudukovic, N. A.; Destino, J. F.; Zhu, C.; Duoss, E. B.; Baumann, T. F.; Suratwala, T.; Smay, J. E.; Dylla-Spears, R., 3D-Printed Transparent Glass. *Adv. Mater.* **2017,** *29* (26), 1701181.

Chapter 4. Plasmonic Biosensing with Aluminum Thin Films under the Kretschmann Configuration

4.1 Introduction

Surface plasmon resonance (SPR) spectroscopy is a well-established analytical technique for label-free quantification of molecular interactions at an interface.[1] The method relies on detecting the minute changes in refractive index of a dielectric medium in contact with a nanometer-scale thin metal film.[2] The metal layer used has traditionally been gold due to its high plasmonic activity and inert chemical character. Increasing attention, however, is being invested toward other metals such as chromium,[3] copper,[4] and aluminum[5] as plasmonic materials. Aluminum is particularly attractive as it has a high electron density (3 electrons per atom in its conduction band versus 1 electron for gold and silver) and a generally higher negative permittivity than silver or gold.[6] This property leads to plasmonic resonance in a very large wavelength range, making aluminum plasmonically active from the ultraviolet to near-infrared regimes. Aluminum is also appealing for commercial applications due to high abundance, low-cost, and easy integration into manufacturing processes such as CMOS.[7]

Up until now, the study of aluminum as a plasmonic material has been almost entirely confined to aluminum nanostructures, with a range of reports exploring structures such as nanorods and nanodiscs, among others.[8-15] Aluminum as a surface-enhanced Raman scattering (SERS) substrate has also been reported.[16-18] However, the use of aluminum in the standard configuration for SPR spectroscopy (i.e., Kretschmann

configuration), where thin metal films are attached to an ATR optical coupler, has not been rigorously studied. Some reports investigated the resonances in the ultraviolet region to probe organic and biological systems that exhibit strong UV absorptions,[19, 20] while other attempts with aluminum films were impaired by substrate stability issues and failed to generate meaningful results.[21]

In this chapter, plasmonic characterization is presented of Al thin films in ATR mode, employing both FDTD and the Fresnel models to predict the surface plasmon polariton (SPP) behavior on the aluminum film and conducting an extensive experimental study to understand and verify the fundamental SPR characteristics of the metal. This analysis of Al film is essential to fully expanding the scope of potential biosensing applications, which seek to characterize various SPR refractive index sensing and biosensing performance in the standard Kretschmann configuration.

4.2 Experimental Methods

Materials and Reagents. Bovine serum albumin (BSA) was obtained from Sigma-Aldrich (St. Louis, MO). Sodium chloride was obtained from Fisher Scientific (Pittsburgh, PA). Biotinylated bovine serum albumin (Biotin-BSA) and streptavidin were obtained from Thermo Scientific (Rockford, Il). BK-7 glass substrates for deposition were obtained from Corning (Painted Post, NY). Aluminum, gold and chromium targets for electron-beam evaporation were acquired as pellets of 0.9999% purity from Kurt J. Lesker (Jefferson Hills, PA). Whole human serum was obtained from Innovative Research (Novi, MI) as single donor human serum off the clot.

SPR and SPR imaging substrate fabrication. Both SPR and SPR imaging substrates were fabricated using BK-7 glass microscope slides as the initial substrate. Slides were cleaned using boiling piranha solution (3:1 H2SO4:30% H2O2) for 1 hr, followed by rinsing with ultrapure water and ethanol and drying with compressed nitrogen gas. For conventional SPR chips, 15 nm (5.0 Å/s) of aluminum was evaporated onto one side of the slide via electron beam physical vapor deposition. (EBPVD) (Temescal, Berkeley, CA). For Au chips, evaporation instead consisted of 2 nm of chromium (0.5 Å/s) and 50 nm of gold (2.0 Å/s). All EBPVD was conducted at 5×10^{-6} Torr in a Class 1000 cleanroom facility (UCR Center for Nanoscale Science and Engineering). SPR imaging arrays were fabricated in accordance to previously described methods[22] with some modification. Cleaned glass slides were spin-coated with hexamethyldisilazane (HMDS) to promote adhesion, followed by AZ5214E, both at 4000 RPM for 45 s. After baking for 1 min at 110° C, the photoresist was patterned by UV exposure using a Karl-Suss MA-6 system and a photomask, followed by development with AZ400K developer and standard protocols. 150 nm of Al (or 2 nm Cr/200 nm Au for gold microarray) was then evaporated onto the surface via EBPVD to form the well walls. The photoresist well spots were then removed using acetone, after which an additional 15 nm of aluminum (or 2 nm Cr/50 nm Au) was evaporated to form the well surface. The final microarrays consisted of a 10 × 10 array of circular wells that were 165 nm (or 250 nm for gold microarray) deep and 600 μm in diameter. Both SPR and SPRi substrates were stored in air for 3 days prior to use.

Atomic force microscopy measurements. AFM measurements were taken using an AIST-NT instrument with a 42 N/m tip provided by NanoWorld. Data was acquired in

tapping mode. Gwyddion 2.55 software was used to analyze the resulting data and determined the root mean squared roughness of the surface to be 0.834 nm.

SPR and SPR imaging analysis. A dual-channel NanoSPR6-321 spectrometer (Nano SPR, Chicago, Il) was used for all spectroscopic measurements for conventional SPR. The device used a GaAs semiconductor laser light source (λ = 670 nm), a manufacturer-supplied prism of high refractive index (n = 1.616) and a 30 μL flow cell. Fabricated chips were inserted, and online analysis was conducted in an angular scanning mode that tracked the resonance angle every 5 s while also collecting the angular spectrum at each point. For bulk refractive index testing, 18 MΩ ultrapure water was flowed at a rate of 5 mL/hr as a baseline and NaCl solutions were flowed over the surface. Sodium chloride solutions were diluted from NaCl salt with ultrapure water, and refractive index of each solution was measured with an Abbe refractometer (American Optics, Buffalo, NY). Intensity measurements were extracted from angular spectra at a constant angle at ~20% of the maximum to ensure maximum sensitivity for both Al and Au chips. Biosensing experiments were conducted using 1×PBS running buffer at 5 mL/hr at ambient temperature. Concentrations of BSA, biotin-BSA and streptavidin used in analysis were 2 mg/mL, 2 mg/mL, and 500 μg/mL, respectively. Analytes were incubated for 30 min to 2 hr, depending on the experiment, before rinsing, and all solutions besides the whole human serum were diluted in 1×PBS prior to the experiment.

SPR imaging was conducted using a home-built setup, a detailed description of which was reported in previous work.8 In brief, each microarray substrate was mounted onto an optical stage that utilized an equilateral SF2 prism (n = 1.648) and a 300 μL flow

cell. The optical stage was fixed to a rotatable goniometer that allowed manual tuning of the incident angle of a 648 nm incoherent light emitting diode (LED) source that was used for SPR excitation. Reflected images were captured with a cooled 12-bit CCD camera (QImaging Retiga 1300) with a resolution of 1.3 MP (1280 × 1024 pixels) and 6.7 μm × 6.7 μm pixel size. Bulk refractive index testing was conducted similarly to conventional SPR testing. Realtime changes in reflectance upon injection of NaCl analyte solutions were recorded every 300 ms inside the individual well elements, and intensity changes were reported as an average of at least 20 individual wells. Intensity data was normalized by dividing the intensity of p-polarized light by the intensity generated by s-polarized light.

FDTD and Fresnel-based Simulations. FDTD based simulations were performed using EM Explorer software. Simulations were conducted in similar manner to previously reported,[23] and parameters were as follows. Real and imaginary parts of the Al and Al_2O_3 refractive indices across the wavelength spectrum were obtained from the Filmetrics database.[24] The Al thickness was varied from 9 nm to 18 nm, and Al_2O_3 was kept at a consistent 3 nm. The Yee cell size was set to be 5 nm cubes. The light was set to be p-polarized. This was then used to probe the plasmonic activity with 500-800 nm wavelength of light with a range of incident angles from 40-85 degrees. Table 4.1 lists the optical constants used in the Fresnel-based angular spectrum simulations. Literature sources were used to obtain values of Al and Au,[25] and for value of Al_2O_3.[26] Simulation was conducted as previously reported[27] and was based on standard Fresnel multi-layer calculation model, the layers of which are shown in Figure 4.1. For Au simulation, Al and Al_2O_3 were replaced with 50 nm Au.

Table 4.1. Refractive index values used in Fresnel-based simulations.

Wavelength	Prism	Al	Al_2O_3	Au	H_2O
650 nm	1.616	1.483 + i7.577	1.765	0.169 + i3.136	1.333

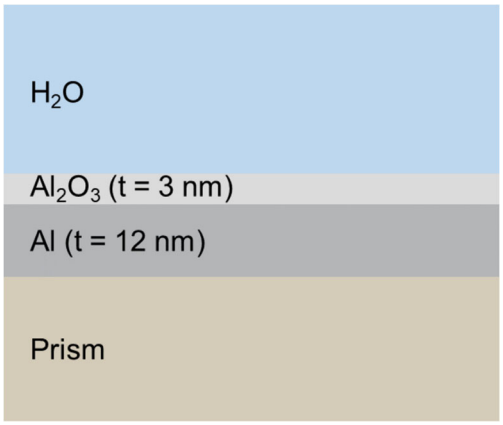

Figure 4.1. Layer configuration for Fresnel-based calculation (t = thickness).

4.3. Results and Discussion

Simulations and Modeling. Initial modeling work was conducted by using a finite difference time domain (FDTD) simulation and the Fresnel equation simulation (Figure 4.2c). The Fresnel equations determine the proportions of an incident wave that are reflected and transmitted when it strikes the interface of materials with differing refractive indexes. For the Fresnel equations to function, the materials must be universally homogeneous thin films.[28] FDTD solves for electrical and magnetic fields in all dimensions by defining a Yee cell wherein cell size is dependent on the permittivity and permeability of the material and the time step.[29] Simulation results reveal that aluminum shows a sharp peak in reflectivity before the dip (Figure 4.2b,c), whereas for gold films, a smooth total internal reflection plateau prior to the plasmonic dip is typically displayed. Using the Lorentz–Drude model,[30] this can be ascribed to the higher valence shell charge density of

aluminum, i.e., three electrons in its conduction band versus one for gold. This results in a higher metallic plasma frequency ω_p, which then results in increased real (n) and imaginary (k) portions of the refractive index (see Chapter 1, Section 1.3 for further discussion). Though the effects of n and k on angular reflectivity dips are complex,[28] high k-values are strongly correlated with plasmonic dips and increased plasmonic activity. Aluminum's higher n and k values also mean that standard film thicknesses used for Au (45–50 nm) were not applicable to Al, and the FDTD analysis across a wide range of thicknesses indicated that experimental investigation should target the 10–20 nm range (Figure 4.2c).

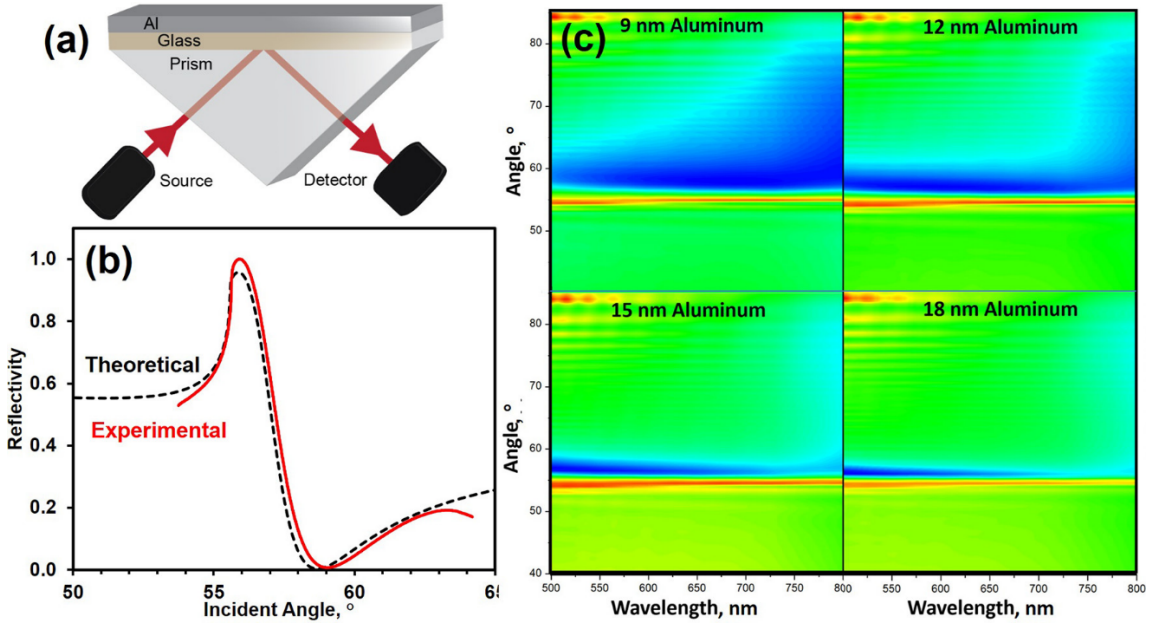

Figure 4.2. (a) Illustration of Kretschman configuration with the Al film. (b) Comparison of experimental angular spectrum of 12/3 Al/Al_2O_3 film in water at 650 nm to theoretical calculation from the Fresnel equations. (c) FDTD simulations of reflectivity of aluminum thin films with a 3 nm alumina overlayer in water.

Fabrication and Material Characterization of Al thin films. In our study, plasmonic aluminum films were fabricated by e-beam depositing Al onto glass slides, with

the initial deposited thickness set at 15 nm. The films were stored in air for 3 days in order to ensure a consistent and fully oxidized alumina layer, which can be approximated to a final Al/Al_2O_3 thickness of 12/3 nm. The films were then mounted to a prism for SPR measurement (Figure 4.2a). Figure 4.2b shows a typical angular reflection spectrum with water using the Al substrate (in red), which shows excellent agreement to the corresponding theoretical prediction (black dashed line).

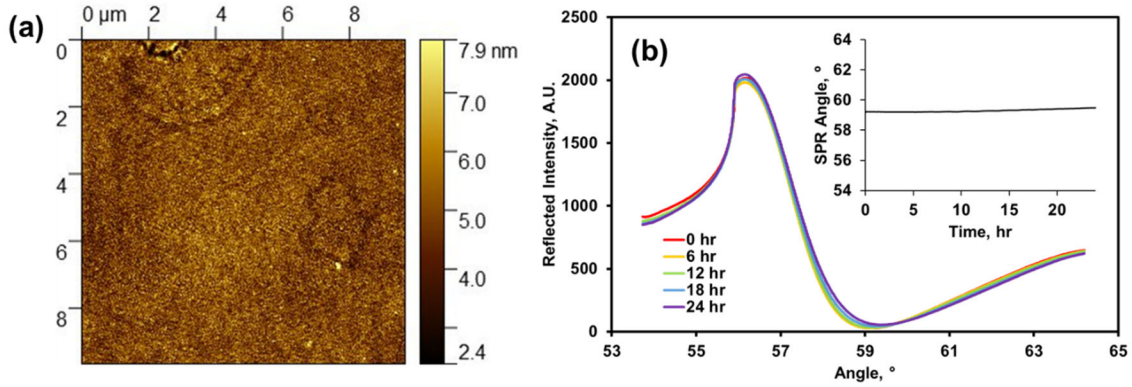

Figure 4.3. (a) AFM image of deposited Al/Al_2O_3 film. (b) Angular SPR spectra of on-line stability test of 12/3 nm Al/Al_2O_3 film with continuous 1X PBS buffer flow for 24 hr. Inset: SPR sensorgram of same experiment.

Chemical stability of aluminum in aqueous-based systems is a concern for biosensing applications[31, 32] as aluminum is more reactive than other plasmonic materials such as gold and silver and thus can be prone to corrosion. We tested the stability of the deposited aluminum surface using 1× phosphate-buffered saline (PBS) (Figure 4.3b). Continuous flowing of PBS buffer over 24 h did not significantly alter the shape of the spectrum, and the plasmonic dip did not show noticeable drift over the same period. Soaking the chips in 10× PBS buffer for 24 h also resulted in essentially no visible changes in the surface or resulting spectra. This indicates the formed aluminum oxide overlayer is

an effective protection layer to prevent corrosion across the typical time scale of biosensing experiments (1–8 h). Atomic force microscopy (AFM) of the surface after native oxidation shows an RMS surface roughness of 1.5 nm (Figure 4.3a), suggesting the oxidized surface is highly uniform and thus ideal for binding studies in SPR analysis.

Optical Characterization in Kretschmann Configuration. SPR sensitivity characterization for the aluminum film consists of two parts: bulk and surface. A bulk sensitivity test was conducted with NaCl solution in various concentrations flowed over the surface. Angular spectra of a range of solutions are displayed in Figure 4.4a. Tracking the shift in the minimum of the dip yields a calibration curve of resonant angle shifts versus refractive index, displayed in Figure 4.4b (in blue). Clearly, bulk test showed a good linear response with the Al substrate. From the curve, we determined the sensitivity with angular scanning to be 59.25°/RIU for the 15 nm Al film.

From the reflection spectra, the resonance band appears to be steeper than that of gold (Figure 4.4e). Therefore, we next moved to quantify the intensity changes at a fixed angle, a strategy that is frequently used[33, 34] and is generally simpler to track (Figure 4.4c,d). At a fixed angle, aluminum shows both a higher sensitivity (70041 IU/RIU, 13.9% higher than Au) and a much longer linear range (~0.028 vs ~0.013 RIU) than gold. For angular shift measurement, however, Au film shows a slightly better reported sensitivity (Figure 4.4b). This is largely because the aluminum's plasmonic dip is broader compared to that of gold and more complex than the gold band, compromising the angular shift tracking reliability by the instrument. The varied sensitivity trend between the fixed angle and the angle-shift data is a direct result of the spectral features of the plasmonic responses of the

metal films, as shown in Figure 4.4e,f. The steep slope of the plasmonic dip for aluminum suggests it is particularly suited for fixed angle measurements, where greater angle reflectance change leads to better sensitivity.

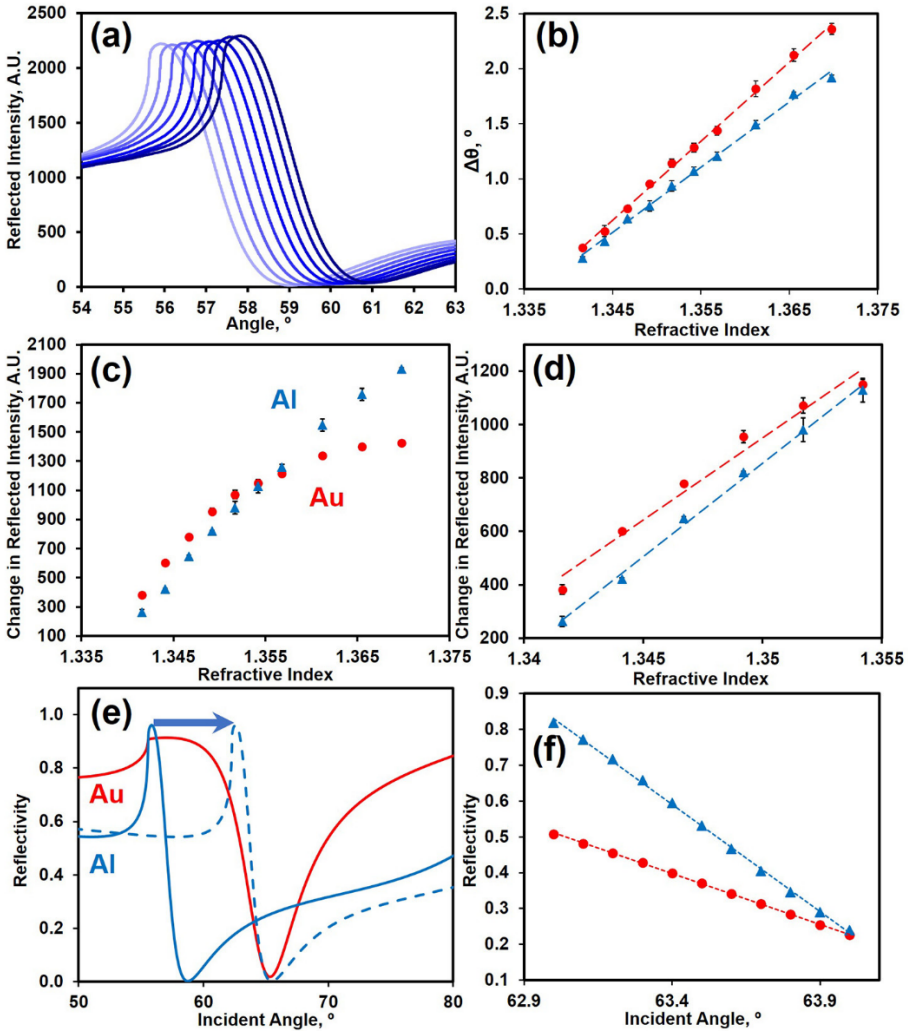

Figure 4.4. Experimental bulk refractive index testing. (a) Measured angular spectra of aluminum film with varying refractive indices from 1.33 to 1.37. (b) Shift in angular dip for gold and aluminum films. (c) Change in reflected intensity at a fixed angle and (d) across the Au linear range. (e) Simulated spectra for aluminum and gold superimposed onto each other and (f) a comparison of the reflectivities across the lower-angle side of the plasmonic dip.

Analytical Biosensing Characterization. The characterization of SPR biosensing performance, i.e., surface sensitivity, was conducted by the well-characterized biological interaction between biotin and streptavidin. As shown in Figure 4.5a, biotinylated bovine serum albumin (biotin-BSA) was incubated on the sensing surface followed by injection of streptavidin. A significant binding shift was observed after the final rinse, while in a control channel where BSA was not biotinylated resulted in little angular shift in the streptavidin step, indicating that biological affinity interactions at the surface were the sole source of the binding signal. The binding signal was stable and is consistent with Au film-based SPR experiments reported throughout literature.[35-38] This indicates that the fundamentals of protein attachment, surface sensitivity, and subsequent biosensing are equally accessible on the Al films.

An interesting aspect of aluminum films for plasmonic sensing is their lack of "stickiness" toward biological components such as proteins and lipids, as cell membrane mimics were reported to adhere much more slowly to an Al/Al_2O_3 surface than to a silica or gold surface.[39, 40] We observed when undiluted human blood serum was incubated over the surface and was followed by rinsing, very little nonspecific binding signal remained (Figure 4.5b inset), a reduction by more than 75% as compared with a gold chip under similar conditions. This potential antifouling function of the Al/Al_2O_3 surface could be of great use in biosensing in complex media. Figure 4.5b shows the sensorgrams with spiked streptavidin in undiluted serum. Subtracting a control of only blood serum, the specific binding signal was only slightly smaller in serum (0.17°) than in buffer (0.21°). This is a remarkable result for a plain surface without any antifouling modifications or steps.

Overcoming nonspecific binding is a strong challenge in implementation for all types of plasmonic based biosensors. A large amount of work by our group and others[41-51] has been conducted in order to use Au chips with complex matrixes such as blood serum, but Al chips will require much less of this type of effort in their use.

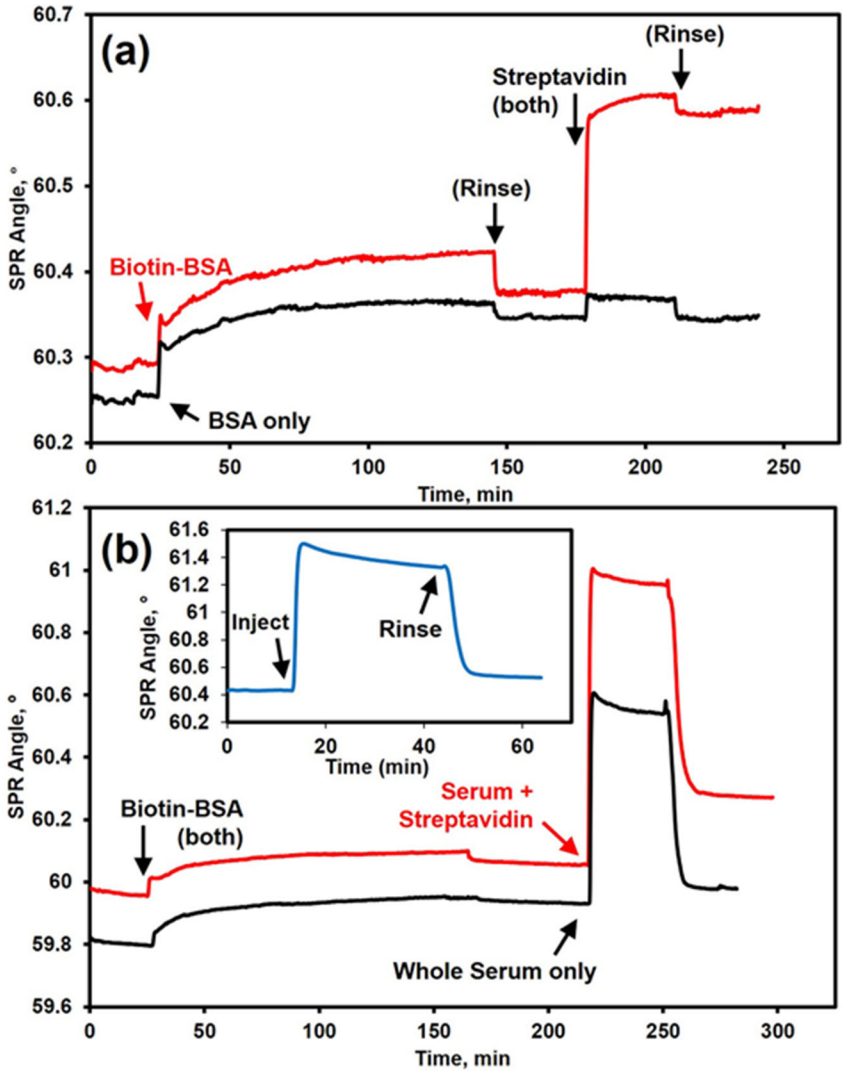

Figure 4.5. SPR sensorgrams of biosensing with Al thin films. (a) Streptavidin sensing on aluminum surface that had been incubated with biotin-BSA (red) and just BSA (black). (b) Streptavidin sensing in undiluted human serum; inset: undiluted serum on the bare Al surface.

Surface Plasmon Resonance Imaging. The spectral characteristics of the aluminum films in fixed-angle monitoring also make it an excellent candidate for SPR imaging. SPR imaging measures at a fixed angle, and the only monitored parameter is reflection intensity.[33] As the method enables the capturing of a wide swath of analysis spots, SPR imaging is frequently used with arrays, significantly improving throughput and multiplexing capabilities of SPR spectroscopy.[52] To test this potential use of aluminum thin films, we fabricated an aluminum microarray for SPR imaging adapted from a design that we have described previously.[22] A summary of the fabrication is displayed in Figure 4.4a. This includes photolithographic patterning and multiple deposition steps, which serve to create 15 nm-thick wells of 800 nm diameter with 150 nm thick walls. The 150 nm thick aluminum layer dampens effective plasmonic absorption, leaving the microwells the only plasmonically active areas.

As shown in Figure 4.6b,c, the wells were clearly distinguishable from the background surface, indicating that the plasmonic activity was effectively dampened. Figure 4.4b shows the online imaging of the well substrate at an angle (58°) of high plasmonic absorption in water (RI = 1.333). Bulk sensitivity testing was conducted similarly to the spectral SPR analysis, and images of the changes in the microwell intensities by varying refractive index are shown in Figure 4.6c. A calibration curve was again constructed and compared to gold (Figure 4.6d,e). The sensitivity figure of merit for the aluminum film is 2665% IU/RIU, which is 61.6% higher than that of the gold film (1649% IU/RIU). The high response of aluminum again proves its excellent potential for SPR imaging-based biosensing and bioanalysis.

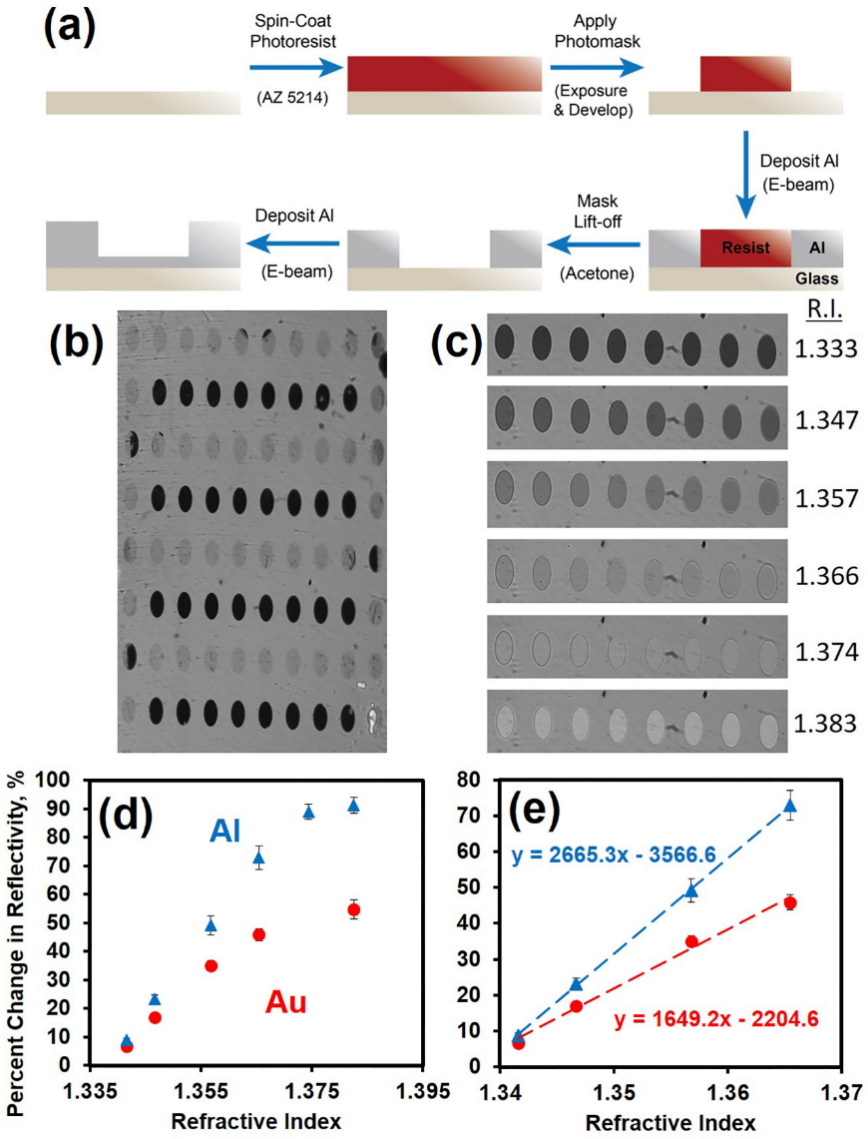

Figure 4.6. SPR imaging with Al thin films. (a) Fabrication scheme of the microarray substrate. (b) Online image of an array with water over the wells. (c) Comparison of well brightness with incubation of increasing refractive index solutions. (d) Comparison of percent change in reflectivity using Al and Au films across full and (e) Au linear ranges.

4.4 Conclusion

In summary, we have demonstrated the feasibility of using thin aluminum films for SPR analyses that are currently almost exclusively conducted by gold films. The Al films

can be fabricated by straightforward deposition techniques and show high stability toward solutions of significant salt concentrations, an important consideration as compared to very stable Au films. Bulk sensitivity characterization indicates good plasmonic response comparable or even better than that of Au films, especially when measured at a fixed angle. The surface was responsive to biosensing behavior while exhibiting antifouling behavior, suppressing significant nonspecific interactions. Aluminum is also amenable to generating background-free SPR imaging substrates of similar bulk refractive index sensitivity. Furthermore, Al_2O_3 has a broad range of established funtionalization pathways for the immobilization of biomolecules, such as silanization, carboxylation, and phosphonylation, which can be used in a similar manner to that of the common thiolation-based Au surface functionalization.[53] We believe that this work has demonstrated some of the exciting plasmonic properties of Al and could serve as a launching point for a multitude of possibilities and improvements to SPR analysis in the future.

4.5 References

1. Homola, J.; Yee, S. S.; Gauglitz, G., Surface plasmon resonance sensors: review. *Sens. Actuator B-Chem.* **1999,** *54* (1-2), 3-15.

2. Homola, J., Surface plasmon resonance sensors for detection of chemical and biological species. *Chem. Rev.* **2008,** *108* (2), 462-493.

3. Sadeghi, S. M.; Hatef, A.; Nejat, A.; Campbell, Q.; Meunier, M., Plasmonic emission enhancement of colloidal quantum dots in the presence of bimetallic nanoparticles. *J. Appl. Phys.* **2014,** *115* (13), 7.

4. Zhou, M.; Tian, M.; Li, C., Copper-Based Nanomaterials for Cancer Imaging and Therapy. *Bioconjugate Chemistry* **2016,** *27* (5), 1188-1199.

5. Gerard, D.; Gray, S. K., Aluminium plasmonics. *J. Phys. D-Appl. Phys.* **2015,** *48* (18), 14.

6. Rakić, A. D., Algorithm for the determination of intrinsic optical constants of metal films: application to aluminum. *Applied Optics* **1995,** *34* (22), 4755-4767.

7. Knight, M. W.; King, N. S.; Liu, L. F.; Everitt, H. O.; Nordlander, P.; Halas, N. J., Aluminum for Plasmonics. *ACS Nano* **2014,** *8* (1), 834-840.

8. Hobbs, R. G.; Manfrinato, V. R.; Yang, Y. J.; Goodman, S. A.; Zhang, L. H.; Stach, E. A.; Berggren, K. K., High-Energy Surface and Volume Plasmons in Nanopatterned Sub-10 nm Aluminum Nanostructures. *Nano Lett.* **2016,** *16* (7), 4149-4157.

9. Zhu, Y.; Nakashima, P. N. H.; Funston, A. M.; Bourgeois, L.; Etheridge, J., Topologically Enclosed Aluminum Voids as Plasmonic Nanostructures. *ACS Nano* **2017,** *11* (11), 11383-11392.

10. Liu, J. J.; Yang, L.; Zhang, H.; Wang, J. F.; Huang, Z. F., Ultraviolet-Visible Chiroptical Activity of Aluminum Nanostructures. *Small* **2017,** *13* (39), 9.

11. Yang, K. Y.; Butet, J.; Yan, C.; Bernasconi, G. D.; Martin, O. J. F., Enhancement Mechanisms of the Second Harmonic Generation from Double Resonant Aluminum Nanostructures. *ACS Photonics* **2017,** *4* (6), 1522-1530.

12. Rodriguez, R. D.; Sheremet, E.; Nesterov, M.; Moras, S.; Rahaman, M.; Weiss, T.; Hietschold, M.; Zahn, D. R. T., Aluminum and copper nanostructures for surface-enhanced Raman spectroscopy: A one-to-one comparison to silver and gold. *Sens. Actuator B-Chem.* **2018,** *262*, 922-927.

13. Su, M. N.; Ciccarino, C. J.; Kumar, S.; Dongare, P. D.; Jebeli, S. A. H.; Renard, D.; Zhang, Y.; Ostovar, B.; Chang, W. S.; Nordlander, P.; Halas, N. J.; Sundararaman, R.; Narang, P.; Link, S., Ultrafast Electron Dynamics in Single Aluminum Nanostructures. *Nano Lett.* **2019,** *19* (5), 3091-3097.

14. Lee, K. L.; You, M. L.; Wei, P. K., Aluminum Nanostructures for Surface-Plasmon-Resonance-Based Sensing Applications. *ACS Appl. Nano Mater.* **2019,** *2* (4), 1930-1939.

15. Arora, P.; Awasthi, H. V., Aluminum-Based Engineered Plasmonic Nanostructures for the Enhanced Refractive Index and Thickness Sensing in Ultraviolet-Visible-Near Infrared Spectral Range. *Prog. Electromagn. Res. M* **2019,** *79*, 167-174.

16. Taguchi, A.; Hayazawa, N.; Furusawa, K.; Ishitobi, H.; Kawata, S., Deep-UV tip-enhanced Raman scattering. *J. Raman Spectrosc.* **2009,** *40* (9), 1324-1330.

17. Dorfer, T.; Schmitt, M.; Popp, J., Deep-UV surface-enhanced Raman scattering. *J. Raman Spectrosc.* **2007,** *38* (11), 1379-1382.

18. Mogensen, K. B.; Guhlke, M.; Kneipp, J.; Kadkhodazadeh, S.; Wagner, J. B.; Palanco, M. E.; Kneipp, H.; Kneipp, K., Surface-enhanced Raman scattering on aluminum using near infrared and visible excitation. *Chem. Commun.* **2014,** *50* (28), 3744-3746.

19. Tanabe, I.; Tanaka, Y. Y.; Watari, K.; Hanulia, T.; Goto, T.; Inami, W.; Kawata, Y.; Ozaki, Y., Aluminum Film Thickness Dependence of Surface Plasmon Resonance in the Far- and Deep-ultraviolet Regions. *Chem. Lett.* **2017,** *46* (10), 1560-1563.

20. Tanabe, I.; Tanaka, Y. Y.; Watari, K.; Hanulia, T.; Goto, T.; Inami, W.; Kawata, Y.; Ozaki, Y., Far- and deep-ultraviolet surface plasmon resonance sensors working in aqueous solutions using aluminum thin films. *Sci Rep* **2017,** *7*, 7.

21. Oliveira, L. C.; Herbster, A.; Moreira, C. D. S.; Neff, F. H.; Lima, A. M. N., Surface Plasmon Resonance Sensing Characteristics of Thin Aluminum Films in Aqueous Solution. *IEEE Sens. J.* **2017,** *17* (19), 6258-6267.

22. Abbas, A.; Linman, M. J.; Cheng, Q. A., Patterned Resonance Plasmonic Microarrays for High-Performance SPR Imaging. *Anal. Chem.* **2011,** *83* (8), 3147-3152.

23. Li, H.; Chen, C. Y.; Wei, X.; Qiang, W. B.; Li, Z. H.; Cheng, Q.; Xu, D. K., Highly Sensitive Detection of Proteins Based on Metal-Enhanced Fluorescence with Novel Silver Nanostructures. *Anal. Chem.* **2012,** *84* (20), 8656-8662.

24. Filmetrics Refractive Index Database. http://www.filmetrics.com/refractiveindex-database (accessed December).

25. Hagemann, H. J.; Gudat, W.; Kunz, C., Optical constants from the far infrared to the x-ray region: Mg, Al, Cu, Ag, Au, Bi, C, and Al2O3. *J. Opt. Soc. Am.* **1975,** *65* (6), 742-744.

26. Smith, D. Y.; Shiles, E.; Inokuti, M., The Optical Properties of Metallic Aluminum**Work supported by the U.S. Department of Energy. In *Handbook of Optical Constants of Solids*, Palik, E. D., Ed. Academic Press: Boston, 1985; pp 369-406.

27. Tanabe, I.; Tanaka, Y. Y.; Ryoki, T.; Watari, K.; Goto, T.; Kikawada, M.; Inami, W.; Kawata, Y.; Ozaki, Y., Direct optical measurements of far- and deep-ultraviolet surface plasmon resonance with different refractive indices. *Optics Express* **2016,** *24* (19), 21886-21896.

28. Kurihara, K.; Suzuki, K., Theoretical understanding of an absorption-based surface plasmon resonance sensor based on Kretchmann's theory. *Anal. Chem.* **2002,** *74* (3), 696-701.

29. Yee, K. S.; Chen, J. S., The finite-difference time-domain (FDTD) and the finite-volume time-domain (FVTD) methods in solving Maxwell's equations. *IEEE Trans. Antennas Propag.* **1997,** *45* (3), 354-363.

30. Markovic, M. I.; Rakic, A. D., DETERMINATION OF THE REFLECTION COEFFICIENTS OF LASER-LIGHT OF WAVELENGTHS LAMBDA-EPSILON(0.22 MU-M,200 MU-M) FROM THE SURFACE OF ALUMINUM USING THE LORENTZ-DRUDE MODEL. *Applied Optics* **1990,** *29* (24), 3479-3483.

31. Correa, G. C.; Bao, B.; Strandwitz, N. C., Chemical Stability of Titania and Alumina Thin Films Formed by Atomic Layer Deposition. *ACS Appl. Mater. Interfaces* **2015,** *7* (27), 14816-14821.

32. Jha, R.; Sharma, A. K., High-performance sensor based on surface plasmon resonance with chalcogenide prism and aluminum for detection in infrared. *Optics Letters* **2009,** *34* (6), 749-751.

33. Puiu, M.; Bala, C., SPR and SPR Imaging: Recent Trends in Developing Nanodevices for Detection and Real-Time Monitoring of Biomolecular Events. *Sensors* **2016,** *16* (6), 15.

34. Brockman, J. M.; Nelson, B. P.; Corn, R. M., Surface Plasmon Resonance Imaging Measurements of Ultrathin Organic Films. *Annual Review of Physical Chemistry* **2000,** *51* (1), 41-63.

35. Perez-Luna, V. H.; O'Brien, M. J.; Opperman, K. A.; Hampton, P. D.; Lopez, G. P.; Klumb, L. A.; Stayton, P. S., Molecular recognition between genetically engineered streptavidin and surface-bound biotin. *J. Am. Chem. Soc.* **1999,** *121* (27), 6469-6478.

36. Haussling, L.; Ringsdorf, H.; Schmitt, F. J.; Knoll, W., BIOTIN-FUNCTIONALIZED SELF-ASSEMBLED MONOLAYERS ON GOLD - SURFACE-PLASMON OPTICAL STUDIES OF SPECIFIC RECOGNITION REACTIONS. *Langmuir* **1991,** *7* (9), 1837-1840.

37. Cui, X. Q.; Pei, R. J.; Wang, X. Z.; Yang, F.; Ma, Y.; Dong, S. J.; Yang, X. R., Layer-by-layer assembly of multilayer films composed of avidin and biotin-labeled antibody for immunosensing. *Biosens. Bioelectron.* **2003,** *18* (1), 59-67.

38. Kim, H.; Cho, I. H.; Park, J. H.; Kim, S.; Paek, S. H.; Noh, J.; Lee, H., Analysis of a non-labeling protein array on biotin modified gold surfaces using atomic force microscopy and surface plasmon resonance. *Colloid Surf. A-Physicochem. Eng. Asp.* **2008,** *313*, 541-544.

39. Jackman, J. A.; Tabaei, S. R.; Zhao, Z. L.; Yorulmaz, S.; Cho, N. J., Self-Assembly Formation of Lipid Bilayer Coatings on Bare Aluminum Oxide: Overcoming the Force of Interfacial Water. *ACS Appl. Mater. Interfaces* **2015,** *7* (1), 959-968.

40. van Weerd, J.; Karperien, M.; Jonkheijm, P., Supported Lipid Bilayers for the Generation of Dynamic Cell-Material Interfaces. *Adv. Healthc. Mater.* **2015,** *4* (18), 2743-2779.

41. Liu, B. S.; Liu, X.; Shi, S.; Huang, R. L.; Su, R. X.; Qi, W.; He, Z. M., Design and mechanisms of antifouling materials for surface plasmon resonance sensors. *Acta Biomaterialia* **2016,** *40*, 100-118.

42. McKeating, K. S.; Hinman, S. S.; Rais, A. N.; Zhou, Z. G.; Cheng, Q., Antifouling Lipid Membranes over Protein A for Orientation-Controlled Immunosensing in Undiluted Serum and Plasma. *ACS Sensors* **2019,** *4* (7), 1774-1782.

43. Lofas, S.; Johnsson, B.; Edstrom, A.; Hansson, A.; Lindquist, G.; Hillgren, R. M. M.; Stigh, L., METHODS FOR SITE CONTROLLED COUPLING TO CARBOXYMETHYLDEXTRAN SURFACES IN SURFACE-PLASMON RESONANCE SENSORS. *Biosens. Bioelectron.* **1995,** *10* (9-10), 813-822.

44. Zheng, X. J.; Zhang, C.; Bai, L. C.; Liu, S. T.; Tan, L.; Wang, Y. M., Antifouling property of monothiol-terminated bottle-brush poly(methylacrylic acid)-graft-poly(2methyl-2-oxazoline) copolymer on gold surfaces. *J. Mat. Chem. B* **2015,** *3* (9), 1921-1930.

45. Vaisocherova, H.; Yang, W.; Zhang, Z.; Cao, Z. Q.; Cheng, G.; Piliarik, M.; Homola, J.; Jiang, S. Y., Ultralow fouling and functionalizable surface chemistry based on a zwitterionic polymer enabling sensitive and specific protein detection in undiluted blood plasma. *Anal. Chem.* **2008,** *80* (20), 7894-7901.

46. Liu, J. T.; Chen, C. J.; Ikoma, T.; Yoshioka, T.; Cross, J. S.; Chang, S. J.; Tsai, J. Z.; Tanaka, J., Surface plasmon resonance biosensor with high anti-fouling ability for the detection of cardiac marker troponin T. *Anal. Chim. Acta* **2011,** *703* (1), 80-86.

47. Terao, K.; Hiramatsu, S.; Suzuki, T.; Takao, H.; Shimokawa, F.; Oohira, F., Fast protein detection in raw blood by size-exclusion SPR sensing. *Anal. Methods* **2015,** *7* (16), 6483-6488.

48. Luz, J. G. G.; Souto, D. E. P.; Machado-Assis, G. F.; de Lana, M.; Kubota, L. T.; Luz, R. C. S.; Damos, F. S.; Martins, H. R., Development and evaluation of a SPR-based immuno sensor for detection of anti-Trypanosoma cruzi antibodies in human serum. *Sens. Actuator B-Chem.* **2015,** *212*, 287-296.

49. Masson, J. F.; Battaglia, T. M.; Khairallah, P.; Beaudoin, S.; Booksh, K. S., Quantitative measurement of cardiac markers in undiluted serum. *Anal. Chem.* **2007,** *79* (2), 612-619.

50. Beeg, M.; Nobili, A.; Orsini, B.; Rogai, F.; Gilardi, D.; Fiorino, G.; Danese, S.; Salmona, M.; Garattini, S.; Gobbi, M., A Surface Plasmon Resonance-based assay to measure serum concentrations of therapeutic antibodies and anti-drug antibodies. *Sci Rep* **2019,** *9*, 9.

51. Emmenegger, C. R.; Brynda, E.; Riedel, T.; Sedlakova, Z.; Houska, M.; Alles, A. B., Interaction of Blood Plasma with Antifouling Surfaces. *Langmuir* **2009,** *25* (11), 6328-6333.

52. Scarano, S.; Mascini, M.; Turner, A. P. F.; Minunni, M., Surface plasmon resonance imaging for affinity-based biosensors. *Biosens. Bioelectron.* **2010,** *25* (5), 957-966.

53. Sigal, G. B.; Bamdad, C.; Barberis, A.; Strominger, J.; Whitesides, G. M., A self-assembled monolayer for the binding and study of histidine tagged proteins by surface plasmon resonance. *Anal. Chem.* **1996,** *68* (3), 490-497.

Chapter 5: Expanding Biosensing and Bioanalysis Applications of Plasmonic Aluminum Thin Films via Physical and Chemical Surface Modifications

5.1 Introduction

The search for improved plasmonic materials is wide-ranging, as the increasing miniaturization of technological applications requires more and more optic and photonic devices to utilize the nano-scale effects available from plasmonic absorption of photon.[1] In the analytical sciences, the rapid growth of the bioanalytical and biopharmaceutical fields requires more analytical methods that operate on the nanoscale to probe the fine dynamics of cellular components such as proteins, lipids, and nucleic acids. For direct biosensing and more complex bioanalysis, a large component of plasmonic applications come in the form of SPR spectroscopy, which uses an attenuated total reflection (ATR) configuration to sensitivity detect mass or solution changes at a surface in real-time at a range of ~200 nm.[2] SPR applications are typically dominated by Au films, but we have recently reported on the fundamental optical and biosensing properties of thin Al films in SPR configurations.[3] In particular, Al films were demonstrated to be of higher native sensitivity than Au in the SPR imaging mode that uses a fixed angle reflected intensity to widen the analyzable area to an entire array. Aluminum also has the practical advantages of high abundance, lower cost, and easier integration into a variety of manufacturing processes compared to Au and Ag.[4]

Aside from SPR-based applications, thin aluminum films have significant potential towards high-sensitivity MALDI-MS-based analysis. Al foils and nanostructures as

substrates have been investigated and reported as beneficial for matrix-assisted laser desorption ionization mass spectrometry (MALDI-MS).[5-7] In particular, the native aluminum oxide layer is selective for the charge density of phosphorylated peptides,[8] so Al can serve as a means for their enrichment prior to quantification. Furthermore, an attractive plasmonic property of Al compared to Au and Ag is Al's ability to plasmonically absorb a broader spectrum of incident photon wavelengths. While Au's plasmonic absorption dramatically decreases at wavelengths lower than ~500 nm, Al can absorb well into the UV range.[9] This is highly relevant for MALDI-MS analysis due to the near-UV lasers typically used to ionize sample matrices for desorption. The effect of plasmonic Au on MALDI- ionization has been demonstrated recently,[10, 11] so a similar effect could be used for plasmonic Al substrates. The coupling of SPR imaging and MALDI-MS analysis has also been demonstrated in Chapter 2 with thin Au films arrays. The higher sensitivity of plasmonic Al films in the imaging mode and the higher absorption of Al towards incident UV radiation make it a good overall candidate for coupled SPR-MALDI analysis.

In this chapter, modifications and reactions at the aluminum surface are investigated in order to broaden the scope of applications for plasmonic aluminum thin films. Key to these applications are Al thin film microarrays that can be used interchangeably with SPR imaging and MALDI-MS. First, the coordination of Al_2O_3 with phosphate groups is used for enrichment of phosphorylated peptides on an aluminum array for MALDI-MS analysis. Second, physical surface modification via coatings of ionic polymers is employed to analyze charged-based interactions of biomolecules. The expansion of surface chemistry routes via its native oxide layer of Al_2O_3 would serve to

broaden its implementation into conventional SPR experimental setups. The high sensitivity of Al in the imaging mode makes it a good candidate for array-based analysis to compare performances of different surface configurations. As a model system, two urinary chemokine biomarkers CXCL8 and CXCL10 were analyzed for their relative binding dynamics in both buffer and urine matrices. Finally, the direct chemical modification of the Al/Al_2O_3 surface for SPR biosensing was achieved with a silanization-based immobilization of the sensing moiety for determination of bacterial protein streptavidin.

5.2 Experimental Methods

Materials and Reagents. Aluminum targets for electron beam physical vapor deposition (EBPVD) were obtained as pellets of 0.9999% purity from Kurt J. Lesker (Jefferson Hills, PA). BK-7 glass substrates for E-Beam deposition were obtained from Corning (Painted Post, NY). Polyallylamine hydrochloride (PAH) was obtained from Alfa Aesar (Haverhill, MA). Biotin-PEG(2K)-silane was obtained from Nanosoft Polymers (Winston-Salem, NC). 1-Palmitoyl-2-oleoyl-glycero-3-phosphocholine (POPC), 1,2-dioleoyl-sn-glycero-3-ethylphosphocholine (EPC), and 1-palmitoyl-2-oleoyl-sn-glycero-3-phospho-(1'-rac-glycerol) (POPG) were obtained as powder from Avanti Polar Lipids (Alabaster, AL). CXCL8 and CXCL10 proteins were obtained as powder from Sino Biological (Wayne, PA). Acetonitrile, sucrose, potassium chloride, sodium chloride, calcium chloride, sodium phosphate monobasic, and sodium phosphate dibasic were obtained from Fisher Scientific (Pittsburgh, PA). Polyacrylic acid (PAA), poly-L-lysine (PLL), polystyrene sulfonate (PSS), “super” 2,5-Dihydroxybenzoic acid (sDHB), α-cyano-

4-hydroxycinnamic acid (CHCA), phosphoric acid (H_3PO_4), trifluoroacetic acid (TFA), trypsin, bovine α-casein and β-casein, sodium sulfate, uric acid, sodium citrate, creatinine, urea, ammonium chloride, potassium oxalate, and magnesium sulfate were obtained from Sigma-Aldrich (St. Louis, MO).

Artificial Urine Preparation. Artificial urine matrix for biosensing experiments was prepared according to a previously published protocol.[12] Component chemicals were added as solids at the concentrations provided there to ultrapure DI H2O held at 38 ° C under constant stirring. Solution pH was measured to be 6.0 ± 0.1 by a UB-5 pH meter (Denver Instruments, Arvada, CO), and solutions were kept for one week and tested for pH and refractive index shifts before each use.

Fabrication and modification of thin film substrates. Conventional SPR and SPR imaging/array substrates were fabricated with BK-7 glass microscope slides that were cleaned with boiling piranha solution (3:1 H_2SO_4:30% H_2O_2) for 1 hr then rinsed with ultrapure water and ethanol and dried with compressed air. An Electron beam physical vapor deposition (EBPVD) system (Temescal, Berkeley, CA) was used to deposit all Al films, and all EBPVD was conducted in a Class 1000 cleanroom facility (UCR Center for Nanoscale Science and Engineering). For conventional SPR substrates, 18 nm Al was deposited.

Microarray substrates used for SPR imaging and MALDI-MS were fabricated along previously reported procedures.[13] In brief, piranha-cleaned glass slides were spin-coated at 4000 RPM for 45 s with hexamethyldisilazane (HMDS) and AZ5214E in succession, followed by a 1 min bake at 110 ° C. Photopatterning via UV exposure was

conducted with a photomask and Karl-Suss MA-6 system followed by AZ400K development using standard protocols. 150 nm Al was deposited by EBPVD, followed by removal of wells with acetone. An additional deposition of 18 nm Al was lastly added to generate the plasmonically active layer in the wells. The final array was a 10 × 12 set of 600 μm diameter circular wells. For both conventional and imaging substrates, chips were stored under vacuum until experimental use.

For polymer surface modifications, individual aluminum chips used for conventional SPR were immersed in ~5 mL aliquots of solutions of a single polymer diluted to 1o mg/mL in ultrapure DI H_2O for 5 min, rinsed, and repeated before use. In array configurations for SPR imaging and MALDI-MS, solutions of each polymer were spotted onto individual wells in 0.5 μL aliquots, allowed to dry, then rinsed and repeated before use. For chemical functionalization, Al/Al_2O_3 chip substrates were immersed in a 1 mM solution of biotin-PEG(2K)-silane in EtOH overnight (12 hr) with mild agitation, followed by isopropanol rinse and N_2 drying.

MALDI-TOF-MS analysis. Tryptic digestions of α-casein and β-casein were conducted under standard conditions in 1 × PBS buffer. Solutions of 200 μg/mL of analyte protein were boiled at 100 ° C for 1 min to denature the protein. Next, the analyte solution and 5 μg/mL of trypsin were mixed in a 4:1 ratio, respectively, and were heated in a water bath at 38 ° C overnight (15 hr), then quenched by addition of 0.1 % TFA in a 1:10 ratio. For on-chip enrichment of peptide peaks, ~1 μL of resulting mixture was spotted onto individual microarray wells and allowed to sit in a humidity chamber for 30 minutes to reduce evaporation. Microarray wells were then further washed with 0.1 % TFA three times

for 5 min each. MALDI matrix consisting of 10 mg/mL sDHB in a 1:1 mixture of 1 % H_3PO_4 and acetonitrile was spotted and allowed to dry. MALDI-MS spectra for peptide peaks were obtained using an AB-Sciex 5800 MALDI-TOF instrument in positive reflector ion mode. Spectra were compiled and analyzed for m/z peaks with a greater than 3 S/N ratio by an in-lab Matlab package described in a previous report,[11] and peptide profiles were analyzed using Expasy FindPept tool.[14] For polymer-coated microarrays without SPR imaging coupling, solutions of each or both chemokine biomarker were spotted onto individual polymer-coated wells. This was followed by spotting of MALDI matrix consisting of 10 mg/mL CHCA dissolved in a 1:1 mixture of 0.5 % TFA and acetonitrile. Mass spectra were obtained in in linear positive mode at a laser fluency of 5500 au on the same instrument as above.

SPR and SPR imaging. Conventional SPR experiments were conducted using a dual-channel NanoSPR6-321 spectrometer equipped with a GaAs semiconductor laser light source (λ = 670 nm), a manufacturer supplied reflector prism (n = 1.616), and a 30 μL flow cell. Experimental data and sensorgrams were conducted in angular scanning mode, which measured minimum reflected intensity over time. For SPR imaging, measurements were conducted on a home-built experimental setup, a detailed description of which was reported previously.[15] Briefly, aluminum substrate microarrays were mounted onto an SF2 glass 25 mm equilateral triangular prism (n = 1.648) with a layer of high-refractive index matching fluid to facilitate even contact. A 3D printed optical stage and flow-cell holder allowed mounting of a 300 μL S-shaped flowcell that covered four primary well rows and two half-rows during online experiments. The optical stage was

fixed atop a goniometer that could be manually rotated to tune the incident angle of incoming light from an incoherent light emitting diode (LED) source (λ = 648 nm) that could be either p- or s- polarized by a rotatable polarizer. Reflected images from the array were captured with a cooled 12-bit CCD camera (QImaging Retiga 1300) with a resolution of 1.3 MP (1280 × 1024 pixels) and 6.7 μm × 6.7 μm pixel size. Online experimental data acquisition consisted of recording the p-polarized reflected intensity of each well (regions of interest manually selected) every 300 ms during baselining, injection and incubation of analyte solutions, and rinse cycles, followed by an acquisition of the s-polarized intensity. Intensity data was normalized in two ways. First, the p-polarized intensity was divided by the intensity of s-polarized intensity then multiplied by 100 to generate a percentage value. Second, during array-based experiments using polymers, a control channel was used to normalize intensities across experiments. Final percent intensity values are reported as the average of at least 6 wells per channel per experiment, resulting in ~20 wells per reported value. Solutions of sucrose and sodium chloride for bulk sensitivity testing were diluted with ultrapure DI H_2O and their refractive indices were measured with an abbe refractometer (American Optics , Buffalo, NY). Lipid vesicles used in conventional SPR experiments were generated by pipetting lipids stored in 9:1 chloroform:methanol to a 1 mg/mL concentration, drying under N_2 and placing in vacuum for 4 hr, followed by dilution with buffer, sonication, and extrusion into 100 nm lipid vesicles (Whatman 100 nm membrane filters). For SPR-MALDI coupling analyses of chemokines, after analytes were incubated and rinsed, the microarray chip was removed from the SPR imaging setup and

allowed to dry. MALDI matrix of 10 mg/mL CHCA in 1:1 0.5 % TFA:ACN was spotted and arrays were mounted and MALDI analyzed as detailed above.

5.3 Results and Discussion

Al_2O_3-mediated enrichment of phosphorylated peptides. Alpha and beta casein's presence in dairy products make them common sources of phosphorylated peptides in human diets, so their enrichment and quantification are highly investigated.[16-20] We have previously reported nanostructured TIO_2-based arrays for the on-plate enrichment of phosphopeptides and MALDI-MS analysis,[21] and the aluminum array substrate should also be selective for phosphorylated peptides, as the phosphate group coordinates with the oxygens of the surface Al_2O_3. Both α-casein and β-casein were tryptically digested and deposited onto Al thin film microarrays both with a series of enrichment and washing steps in a lightly acidic environment to promote phosphate groups binding to the Al_2O_3. This was compared to a simple deposition and washing to highlight the effect of the enrichment steps. Comparisons of averaged spectra are shown in Figure 5.1 along with lists of identified casein peptides. In both cases, the proportion of phosphorylated peaks dramatically increases after enrichment, from 28% to 43% for α-casein and from 33% to 66% for β-casein. Notably, all peptides initially identified with multiple phosphorylation sites (DIG**S**E**S**TEDQAMEDIK and NTMEHV**SSS**EE**S**IISQETYK for α-casein and RELEELNVPGEIVE**S**L**SSS**EESITR for β-casein) were retained after enrichment and washing steps, indicating that the enrichment

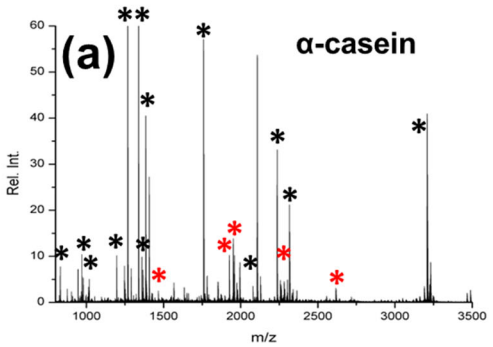

Table 5.1. α-casein peptides from digest found via MALDI-MS on Al array.

m/z	α-casein peptide	m/z	α-casein peptide
831.1	EDVPSER	1759.9	HQGLPQEVLNENLLR
979.5	FALPQYLK	1926.8	DIGSESTEDQAMEDIK
1018.5	LTEEEKNR	1952.5	YKVPQLEIVPNSAEER
1195.7	NAVPITPTLNR	2080.7	EDVPSERYLGYLEQLLR
1267.6	YLGYLEQLLR	2235.9	HPIKHQGLPQEVLNENLLR
1337.6	HIQKEDVPSER	2257.8	VPQLEIVPNSAEERLHSMK
1367.7	ALNEINQFYQK	2316.8	EPMIGVNQELAYFYPELFR
1384.7	FFVAPFPEVFGK	2617.8	NTMEHVSSSEESIISQETYK
1466.7	TVDMESTEVFTK	3208.6	EGIHAQQKEPMIGVNQELAY FYPELFR

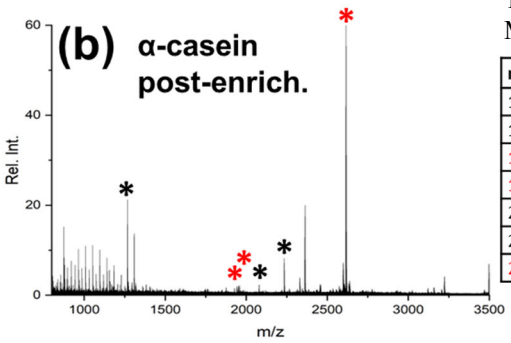

Table 5.2. α-casein peptides from digest found via MALDI-MS on Al array after enrichment.

m/z	α-casein peptide
1267.2	YLGYLEQLLR
1384.1	FFVAPFPEVFGK
1926.6	DIGSESTEDQAMEDIK
1952.2	YKVPQLEIVPNSAEER
2080.1	EDVPSERYLGYLEQLLR
2235.1	HPIKHQGLPQEVLNENLLR
2617.3	NTMEHVSSSEESIISQETYK

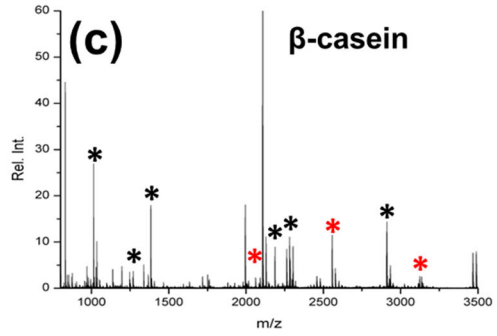

Table 5.3. β-casein peptides from digest found via MALDI-MS on Al array.

m/z	β-casein peptide
1013.4	HKEMPFPK
1270.7	AVPYPQRDMPR
1383.7	KAVPYPQRDMPR
2062.2	FQSEEQQQTEDELQDK
2186.7	DMPIQAFLLYQEPVLGPVR
2281.9	MHQPHQPLPPTVMFPPQSVL
2556.6	FQSEEQQQTEDELQDKIHPF
2911.2	DMPIQAFLLYQ EPVLGPVRGPF PIIV
3122.8	RELEELNVPGEIVESLSSSE ESITR

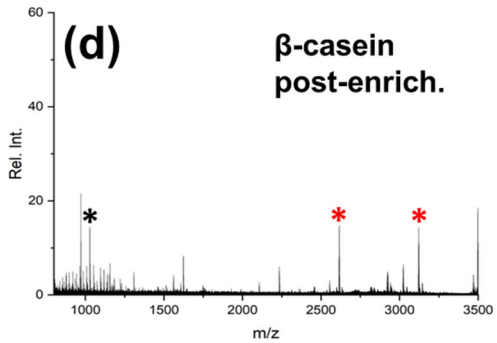

Table 5.4. β-casein peptides from digest found via MALDI-MS on Al array after enrichment.

m/z	β-casein peptide
1013.1	HKEMPFPK
2556.2	FQSEEQQQTEDELQDKIHPF
3122.4	RELEELNVPGEIVESLSSSE ESITR

Figure 5.1. MALDI-MS spectra of casein peptides from digest on Al thin film with and without enrichment. Tables 5.1-5.4 of identified peptides are shown to the right of their respective spectra, phosphorylated peptides in red and phosphorylated resides underlined.

is at least somewhat chemically driven. Significant optimization can be conducted for retention of even more phosphorylated peaks, but this represents the first report of this type of enrichment being successfully conducted on plasmonically active Al thin films.

Qualitative separation of charged vesicles via ionic polymer surface modification. After confirming the utility of bare Al/Al_2O_3, we moved to physical surface modification. As a measure of the qualitative feasibility of charge-based separation of binding signals, lipid vesicles of varying composition were tested for their binding to surfaces of different charge. Binding and fusion of lipid vesicles and membranes to a surface is highly dependent on surface material characteristics;[22-25] for example, the addition of a silica layer to Au thin films reverses lipid bilayer fusion from poor to excellent.[26] Thus, relative changes in binding should be distinguishable here. Lipid vesicles are popular for a variety of bioanalytical purposes, but here they have the benefit of being easily tunable for the desired surface charge. Different lipid head groups compositions serve to present essentially unified exteriors of positive, negative or zwitterionic charge. It should be noted that aluminum oxide has a slightly negative surface charge in aqueous conditions at physiological pH, as the surface oxide becomes slightly hydrolyzed,[27] which the case here with 1 × PBS running buffer.

Individual sensorgrams are shown in Figures 5.2b, 5.2d, and 5.2f of each surface to vesicle combination. The most striking initial feature is the binding signal for the EPC and POPG vesicles is substantially higher for the surface of opposite charge than for either the Al_2O_3 or the similarly charged surface. There is little binding of the POPC vesicles to any

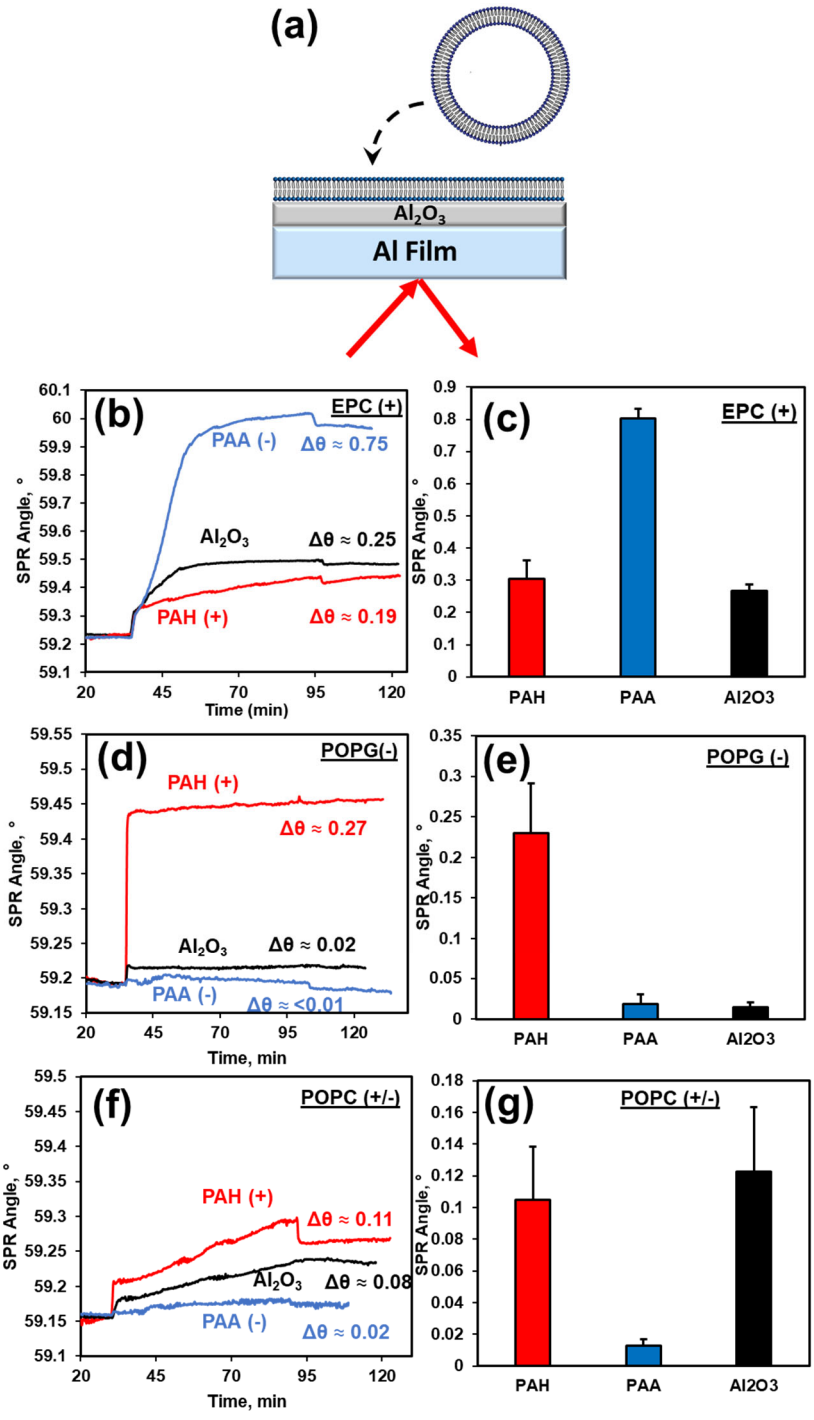

Figure 5.2. Binding of charged lipid vesicles to Al/Al2O3 surfaces with and without ionic polymer modification. (a) Surface diagram; (b), (d), (f) SPR sensorgrams of binding of EPC, POPG, and POPC vesicles, respectively, to Al2O3, and PAH- and PAA-modified surfaces; (c), (e), (g) Bar chart summaries of all experiments.

of the three surfaces, which supports the need for a specific lipid-surface interaction for significant fusion to occur. Notably, the Al_2O_3 surface did not have a vesicle of any composition that preferentially bound to it over either the PAH or PAA, a characteristic observed previously by us and others that is attributed to a strong hydration layer.[28, 29] A more quantitative comparison of the various binding combinations is given in Figures 5.2c, 5.2e, and 5.2g, that shows similar trends.

Microarray analysis of urine biomarker binding dynamics. Microarray-based bioanalysis is ideal for the high sensitivity of Al thin films for SPR imaging, so the charge separation was further interrogated using large peptide biomarkers. Urine biomarker panels are an increasingly popular means of diagnosing kidney, bladder, and prostate diseases and injuries.[30-32] The most popular biomarker type for this diagnostic method are peptides, with many reports showing good diagnostic correlation of biomarker peptide libraries with kidney diseases such as lupus, kidney injury, and bladder cancer.[33-35] Proinflammatory chemokines (C-X-C and C-C motifs) are higher weight peptides (9-11 kda) that are highly representative examples of these urinary biomarkers for these diseases.[36-38] The differences in kinetic versus steady-state binding signal serve to shed light on the pulldown efficiency of the ionic polymers. Polymers for the microarray were selected for an emphasis on the expected preferential binding of the positively charged chemokines. At physiological pH CXCL8 is +5 and CXCL10 is +10, so negatively charged polymers PAA (mildly negative) and PSS (highly negative) were selected, with the positively charged PLL used as a comparison. PAH was not usable in imaging mode, as the initial reflectivity curves for its channel were significantly shifted to higher angles compared to the other polymers, while

PLL was a much closer match (see Figure 5.3b). This match is vital for the imaging mode, as the fixed angle is constant for each channel, and the relative intensity must be initially approximately equal to have comparable results across the array. The shift in the initial reflectivity curves from the polymers indicated high surface sensitivity, so as a test to ensure differential bulk sensitivity between channels was not a colluding factor in the binding analysis, solutions of NaCl were incubated over the microarray. The bulk shifts are shown in Figure 5.4b, and show consistent response across channels, thus this potential factor is minimal here.

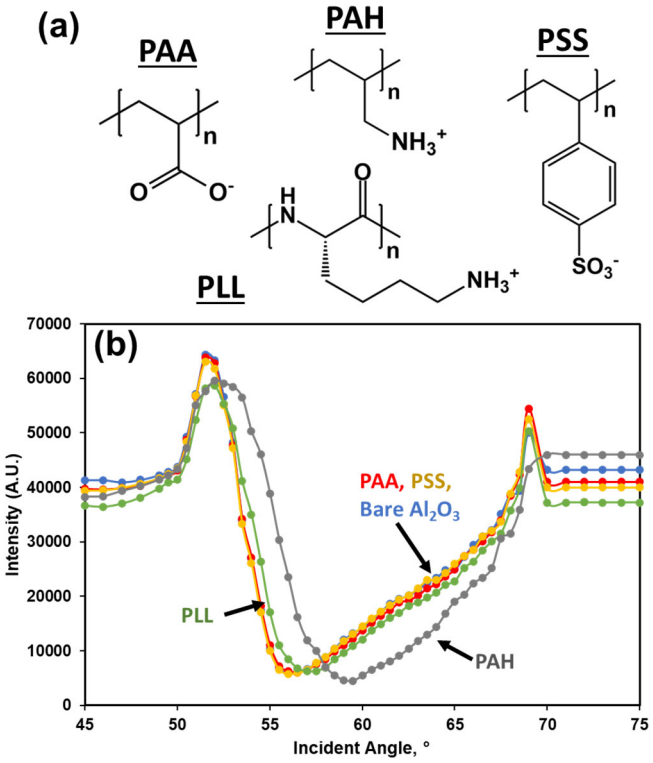

Figure 5.3. (a) Chemical structures of ionic polymer compounds considered for SPR imaging; (b) SPR imaging reflectivity curves of polymer-modified Al microarrays.

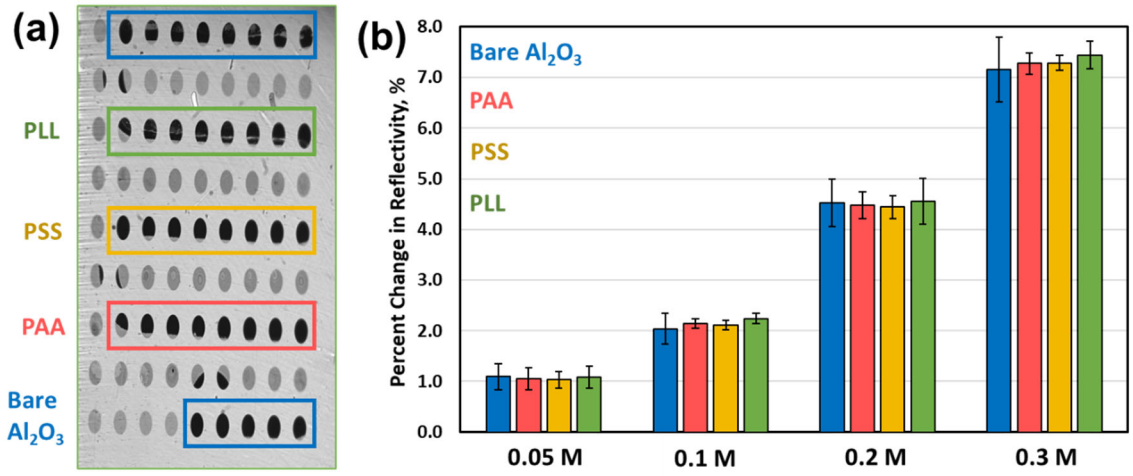

Figure 5.4. (a) Al SPR imaging microarray modified with ionic polymers. Solution flow was "bottom up", so top blue row was auxiliary blank channel. (b) Comparison SPR imaging reflectivity changes in each channel from NaCl solutions of varying concentrations.

A full SPR imaging sensorgram (showing average of well intensities) of incubation of 20 µg/mL of the biomarkers is shown in Figure 5.5a, and comparisons of channel responses are given in Figures (5.5b-e). The "endpoint", or irreversible, binding signal in each case was relatively small, reflecting the low-intensity nature of the charge-based interactions. The clearest representation of charge effects can be seen in the comparison of the kinetic shifts between the two chemokines across the three channels (Figure 5.5d). For the negatively charged PAA and PSS polymer, there is a stronger association between the CXCL10 and the surface than for CXCL8. However, for the positively charged PLL, the kinetic data is reversed, with CXCL8 showing stronger affinity than CXCL10. This reflects the relative charge interactions for CXCL8 (+5) and CXCL10 (+10) at biological buffer pH (7.4). The more positively charged CXCL10 has higher association with the negatively charged surfaces but is consequently more repelled by the positively charged surface.

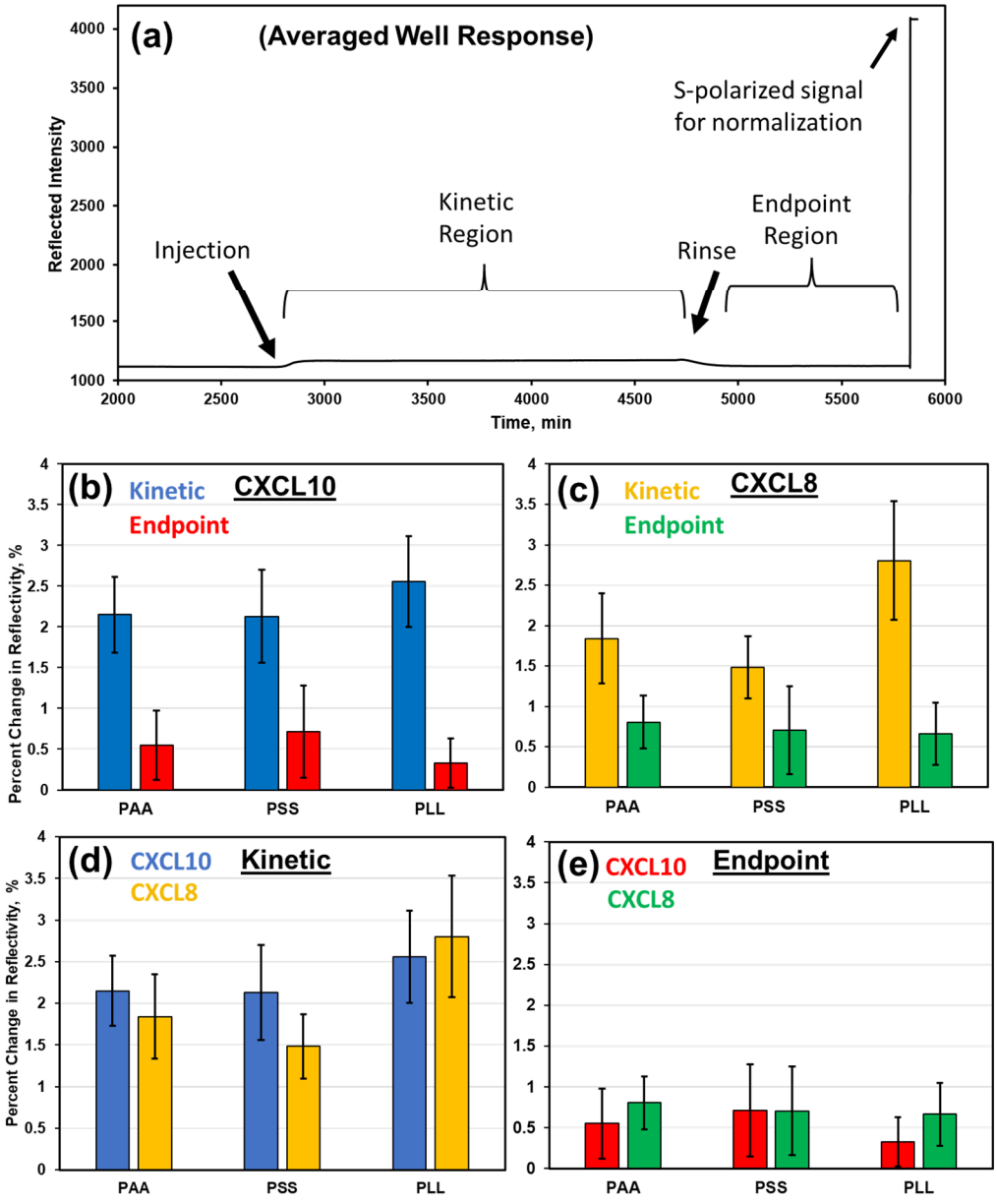

Figure 5.5. (a) SPR imaging sensorgram example using averaged well intensities indicating regions of analysis. (b-e) Bar chart summaries of reflectivity shifts from incubations of CXCL biomarkers.

The effect of a complex biological matrix on this binding was investigated by spiking the chemokines into an artificial urine matrix, a popular medium for studying urine-based biomarkers such as chemokines for kidney and bladder disease.[39-42] The much higher

ionic strength and, more importantly, lower pH (~6.0) of the urine matrix compared to PBS buffer serve to significantly alter the kinetic and endpoint data relationships, as shown in Figure 5.6. Though the bulk refractive index shifts have a higher baseline value due to the urine matrix, taken together, the relative kinetic shifts of the two chemokines reflect a more protonating environment for the binding. For the PLL surface, the relative difference in response between CXCL10 and CXCL8 (+0.68 %) is larger than seen with PBS buffer (+0.25 %), in line with the PLL surface being more positively-charged and more discriminating between positively-charged peptides. Likewise, the PSS relative difference for urine (-0.45 %) is smaller than that of PBS (-0.65 %), and the PAA response is essentially leveled for urine, reflecting the inverse effect, that the polymers are less negatively charged and thus less discriminating. It should be noted that while the change in pH does also affect the charge of the two peptides and affects CXCL8 (+5 in PBS to +7 in urine) more than CXCL10 (+10 to +11), they are still distinct enough in their charge states that they follow the same pattern as before. The SPR imaging array thus serves as an effective platform for illustrating these the pH effect, as the realtime data can be more useful and representative of the biophysical interactions than endpoint data.

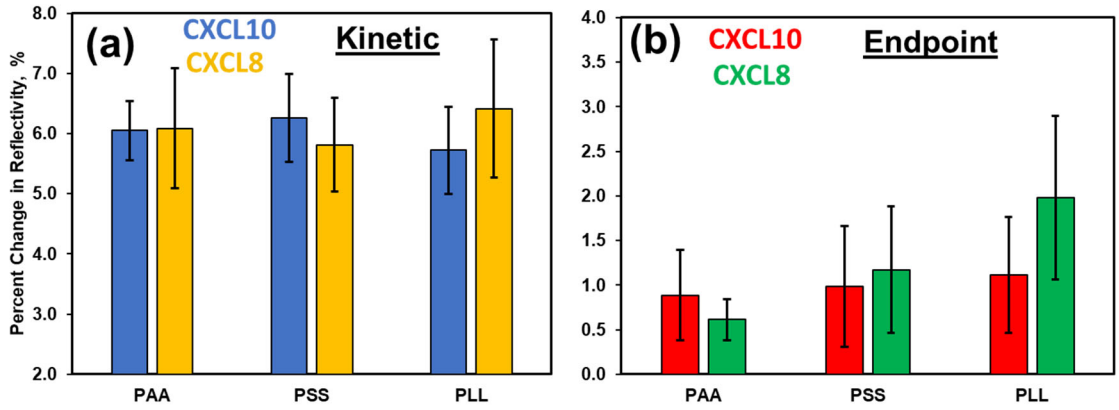

Figure 5.6. Bar chart summaries of kinetic vs endpoint SPR imaging reflectivity shifts from incubations of CXCL biomarkers spiked in artificial urine matrix.

Charge-based effects on MALDI-MS analysis. First, base spectra in linear positive mode were obtained on the Al_2O_3 surface, shown in Figure 5.7. The intact peaks for both chemokines match the expected m/z values given the expressed constructs of each (CXCL8: A29-S99, 8299 kDa; CXCL10: V22-P98, 8646 kDa). The other primary peaks reflect both doubly-charged primary ions (CXCL8: 4100; CXCL10, 4350) and cleavages at the borders of the major subdomains of each, as the chemokines, while not sharing high sequence similarity, are highly homologous, with an α-helix near the C-terminus, two internal β-sheets and third β-sheet that promotes dimerization.[43, 44] In both cases, the signals formed a distinct and consistent profile for identification. Notably, spectra of the same biomarkers obtained a conventional steel plate and an Au plate of the same microarray configuration as used in previous work have m/z intensity values significantly lower than those of the aluminum plate. This supports the assertion that the plasmonic absorption of the aluminum of the UV laser (337 nm) of the MALDI enhances the MS signal.

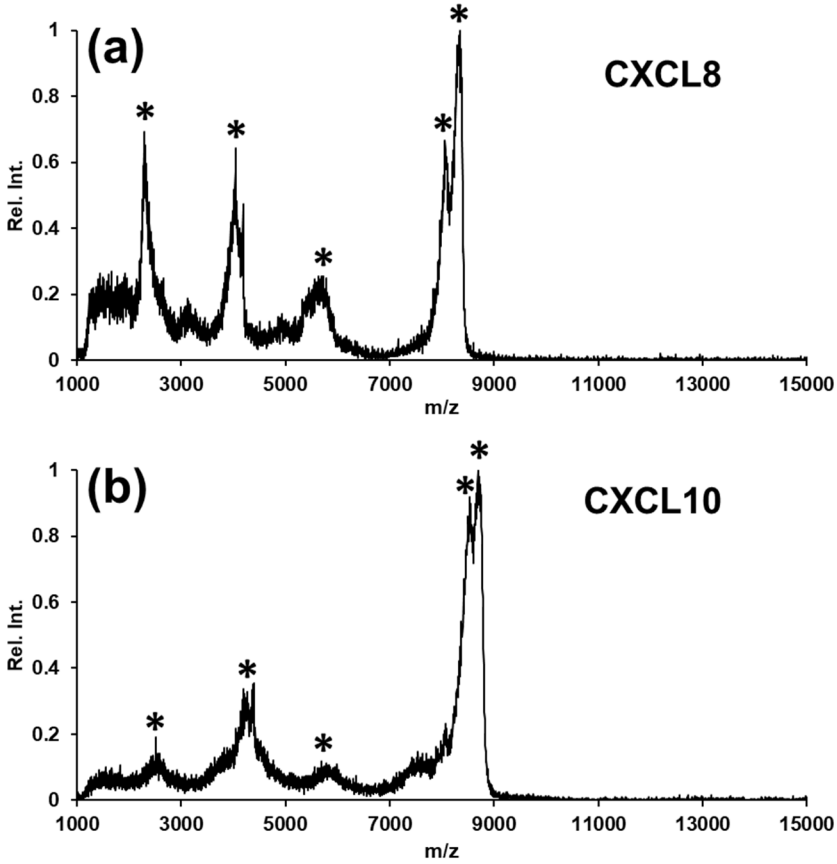

Figure 5.7. Linear MALDI-MS spectra of 100 μg/mL of CXCL biomarkers on Al microarray.

The MALDI-MS spectra in linear positive mode for the chemokines deposited directly onto the polymer surface are shown in Figure 5.8. In all cases, the presence of polymer reduced signal, as would be expected from both the physical separation from the plasmonic surface and the dilution of charge transfer from the MALDI matrix. However, the trend across polymers revealed an unexpected charge-based effect. For both biomarkers, while the PLL coating resulted in a similar peak profile to the bare Al, the PAA coating generated much lower and broader signal intensities on the key identifying peak regions of m/z = 2300, 4100, and 8350 for CXCL8 and m/z = 4350 and 8700 for

CXCL10. The PSS coating essentially suppressed all peaks, and as the peak intensities and sharpness decreased with increasingly negative polymer charge, this indicates that the negative polymer charge significantly affects ionization and signal of positive ions.

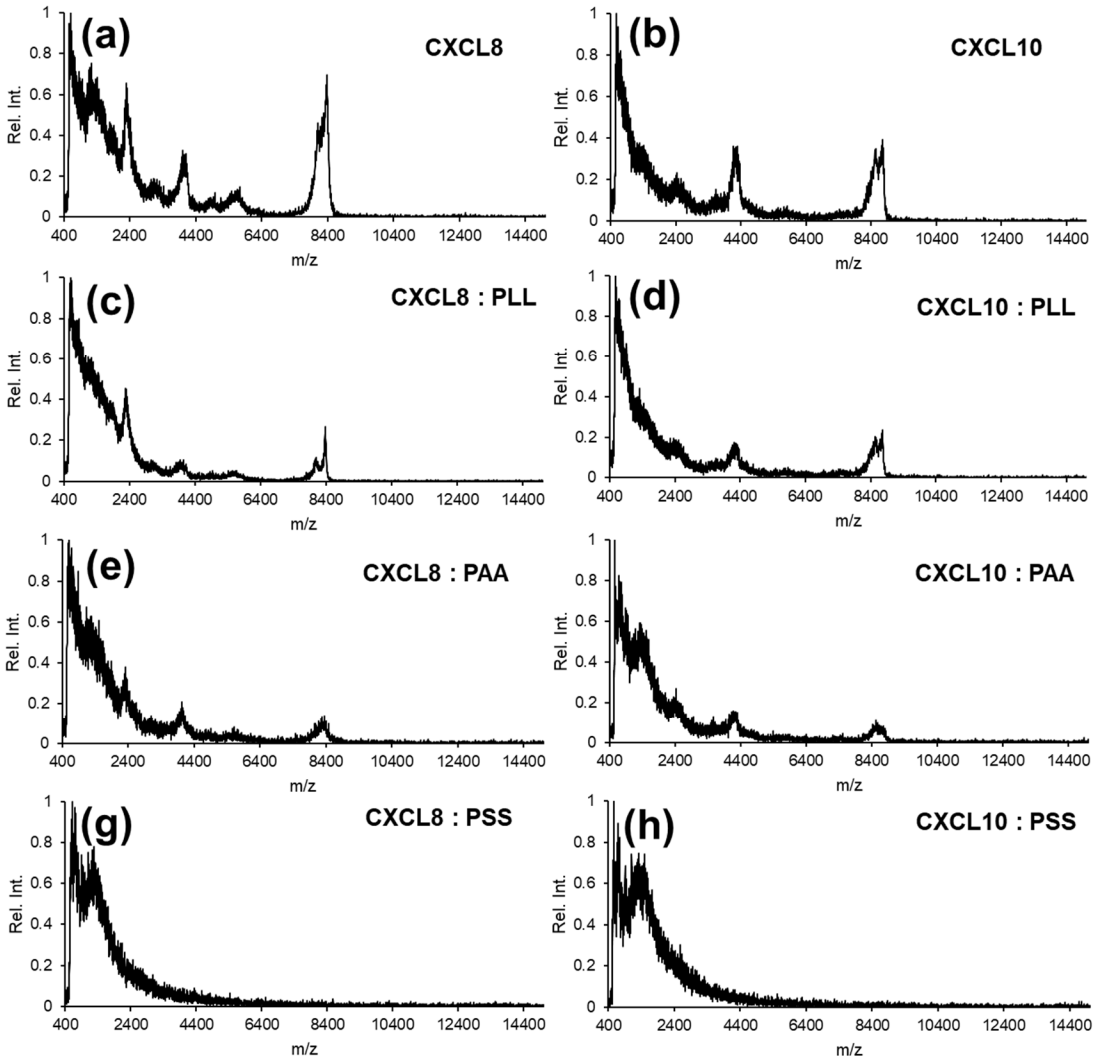

Figure 5.8. Linear MALDI-MS spectra of 20 µg/mL of CXCL biomarkers on Al microarrays with and without ionic polymer surface modification.

In total, for both biomarkers, the presence of peaks is directly correlated to the charge of the surface, with higher negative charge interfering with MALDI ionization. This

interference effect was further reinforced by the final SPR-MALDI coupling, wherein the polymer-coated microarray chip was incubated and quantified on the SPR imaging setup, removed and spotted with MALDI matrix, and used for MALDI-MS analysis. The only surface where a small amount of identifying mass signal for the chemokines was on the bare Al/Al_2O_3 control channel.

Chemical functionalization for bioanalysis via Al_2O_3 silanization. As a final direction, the functionalization of Al_2O_3 by chemical means (rather than physical) is a core component of the use of Al films in SPR biosensing. Immobilization of biological targets takes place via a variety of coupling chemistries, such as EDC/NHS or Ni:NTA-DGS.[45, 46] However, the actual surface chemistry for Au and Ag films is essentially limited to thiol bonds. Here, we demonstrate a surface coupling chemistry for SPR biosensing that is not available for Au or Ag films: silanization. Biotin-PEG(2K)-silane was ligated to an Al thin film conventional SPR chip surface via the silane-oxygen bonds that catalyze into a self-assembled monolayer (see Figure 5.9a). The final chip was mounted on the conventional SPR and used to sense bacterial protein streptavidin via the strong biotin-streptavidin affinity. As shown in Figure 5.9b, an incubation of 100 μg/mL of streptavidin generated a binding signal that remained even after rinsing, as compared to a control incubation of bovine serum albumin, which rinsed off. Thus, a new surface chemistry for conventional SPR biosensing Al_2O_3 silanization, was demonstrated for the first time.

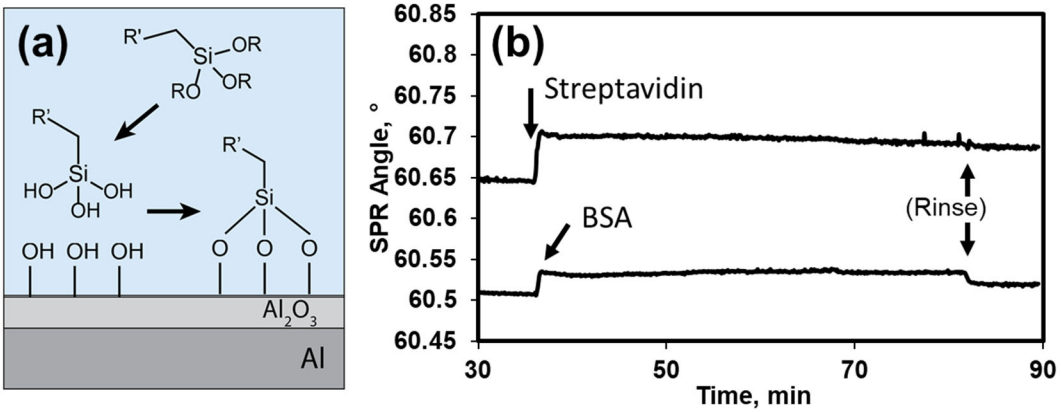

Figure 5.9. (a) Silanization surface chemistry. In this work, R = -CH_2CH_3 and R` = -PEG(2K)-Biotin. (b) SPR sensorgram of incubations of streptavidin and bovine serum albumin (BSA) on separate channels of a silane-functionalized Al chip.

5.4 Conclusion

In summary, the applications of plasmonic aluminum films were investigated via conventional SPR, SPR imaging, and MALDI-MS as the building blocks for a more dense range of analytical platforms. First, the bare Al film was shown to be effective at enrichment of phosphorylated peptides from milk proteins for mass spectrometric profiling. Second, Al films physically modified with ionic polymers were used with SPR and MALDI to analyze charge-based binding interactions for both large macromolecules (lipid vesicles) and highly medically relevant biomarkers. The qualitative separation of charged lipid vesicles by ionic polymers could be easily monitored and showed selectivity over the bare Al surface. In SPR imaging mode, the high sensitivity of aluminum allowed for quantification of kinetic differences of charge-based binding interactions between ionic polymers and biomarker peptides CXCL8 and CXCL10. The binding effects were clearly correlated to the charge densities of the biomarkers and the charged polymers, and the use

of artificial urine matrix altered the association behavior in a well-defined manner. While the MALDI-MS ionization potential of the biomarkers was clearly affected by the polymer surface, the overall insights gleaned point towards a robust method of plasmonic screening of binding affinity by aluminum-based arrays. Finally, the functionalization of the Al_2O_3 overlayer by silanization was reported for selective binding of bacterial protein streptavidin in conventional SPR, the first successful chemical functionalization for SPR biosensing that did not use Au or Ag films. The use of Al films for plasmonic label-free bioanalytical techniques is a subject of great potential and high upside for the future of understanding the complexities of biophysical interactions.

5.5 References

1. West, P. R.; Ishii, S.; Naik, G. V.; Emani, N. K.; Shalaev, V. M.; Boltasseva, A., Searching for better plasmonic materials. *Laser Photon. Rev.* **2010,** *4* (6), 795-808.

2. Tang, Y. J.; Zeng, X. Q.; Liang, J., Surface Plasmon Resonance: An Introduction to a Surface Spectroscopy Technique. *JOURNAL OF CHEMICAL EDUCATION* **2010,** *87* (7), 742-746.

3. Lambert, A. S.; Valiulis, S. N.; Malinick, A. S.; Tanabe, I.; Cheng, Q., Plasmonic Biosensing with Aluminum Thin Films under the Kretschmann Configuration. *Analytical Chemistry* **2020,** *92* (13), 8654-8659.

4. Knight, M. W.; King, N. S.; Liu, L. F.; Everitt, H. O.; Nordlander, P.; Halas, N. J., Aluminum for Plasmonics. *ACS Nano* **2014,** *8* (1), 834-840.

5. Li, Y.; Liu, Y.; Tang, J.; Lin, H.; Yao, N.; Shen, X.; Deng, C.; Yang, P.; Zhang, X., Fe3O4@Al2O3 magnetic core-shell microspheres for rapid and highly specific capture of phosphopeptides with mass spectrometry analysis. *JOURNAL OF CHROMATOGRAPHY A* **2007,** *1172* (1), 57-71.

6. Qiao, L. A.; Bi, H. Y.; Busnel, J. M.; Hojeij, M.; Mendez, M.; Liu, B. H.; Girault, H. H., Controlling the specific enrichment of multi-phosphorylated peptides on oxide materials: aluminium foil as a target plate for laser desorption ionization mass spectrometry. *CHEMICAL SCIENCE* **2010,** *1* (3), 374-382.

7. Bondarenko, A.; Zhu, Y.; Qiao, L.; Salazar, F. C.; Pick, H.; Girault, H. H., Aluminium foil as a single-use substrate for MALDI-MS fingerprinting of different melanoma cell lines. *ANALYST* **2016,** *141* (11), 3403-3410.

8. Wolschin, F.; Wienkoop, S.; Weckwerth, W., Enrichment of phosphorylated proteins and peptides from complex mixtures using metal oxide/hydroxide affinity chromatography (MOAC). *PROTEOMICS* **2005,** *5* (17), 4389-4397.

9. Gerard, D.; Gray, S. K., Aluminium plasmonics. *J. Phys. D-Appl. Phys.* **2015,** *48* (18), 14.

10. Shanta, P. V.; Li, B.; Stuart, D. D.; Cheng, Q., Plasmonic Gold Templates Enhancing Single Cell Lipidomic Analysis of Microorganisms. *Analytical Chemistry* **2020,** *92* (9), 6213-6217.

11. Li, B.; Stuart, D. D.; Shanta, P. V.; Pike, C. D.; Cheng, Q., Probing Herbicide Toxicity to Algae (Selenastrum capricornutum) by Lipid Profiling with Machine Learning and Microchip/MALDI-TOF Mass Spectrometry. *Chemical Research in Toxicology* **2022,** *35* (4), 606-615.

12. Sarigul, N.; Korkmaz, F.; Kurultak, I., A New Artificial Urine Protocol to Better Imitate Human Urine. *SCIENTIFIC REPORTS* **2019,** *9*.

13. Abbas, A.; Linman, M. J.; Cheng, Q. A., Patterned Resonance Plasmonic Microarrays for High-Performance SPR Imaging. *Analytical Chemistry* **2011,** *83* (8), 3147-3152.

14. Gattiker, A.; Bienvenut, W. V.; Bairoch, A.; Gasteiger, E., FindPept, a tool to identify unmatched masses in peptide mass fingerprinting protein identification. *PROTEOMICS* **2002,** *2* (10), 1435-1444.

15. Wilkop, T.; Wang, Z. Z.; Cheng, Q., Analysis of mu-contact printed protein patterns by SPR imaging with a LED light source. *Langmuir* **2004,** *20* (25), 11141-11148.

16. Guo, J. P.; Li, S. J.; Wang, S.; Wang, J. P., Determination of Trace Phosphoprotein in Food Based on Fluorescent Probe-Triggered Target-Induced Quench by Electrochemiluminescence. *JOURNAL OF AGRICULTURAL AND FOOD CHEMISTRY* **2020,** *68* (45), 12738-12748.

17. Xiao, J.; Yang, S. S.; Wu, J. X.; Wang, H.; Yu, X. Z.; Shang, W. B.; Chen, G. Q.; Gu, Z. Y., Highly Selective Capture of Monophosphopeptides by Two-Dimensional Metal-Organic Framework Nanosheets. *ANALYTICAL CHEMISTRY* **2019,** *91* (14), 9093-9101.

18. Qiao, L.; Roussel, C.; Wan, J. J.; Yang, P. Y.; Girault, H. H.; Liu, B. H., Specific on-plate enrichment of phosphorylated peptides for direct MALDI-TOF MS analysis. *JOURNAL OF PROTEOME RESEARCH* **2007,** *6* (12), 4763-4769.

19. Ashley, J.; Shukor, Y.; D'Aurelio, R.; Trinh, L.; Rodgers, T. L.; Temblay, J.; Pleasants, M.; Tothill, I. E., Synthesis of Molecularly Imprinted Polymer Nanoparticles for alpha-Casein Detection Using Surface Plasmon Resonance as a Milk Allergen Sensor. *ACS SENSORS* **2018,** *3* (2), 418-424.

20. Hung, Y. L. W.; Chen, X. F.; Wong, Y. L. E.; Wu, R.; Chan, T. W. D., Development of an All-in-One Protein Digestion Platform Using Sorbent-Attached Membrane Funnel-Based Spray Ionization Mass Spectrometry. *JOURNAL OF THE AMERICAN SOCIETY FOR MASS SPECTROMETRY* **2020,** *31* (10), 2218-2225.

21. Wang, H.; Duan, J. C.; Cheng, Q., Photocatalytically Patterned TiO2 Arrays for On-Plate Selective Enrichment of Phosphopeptides and Direct MALDI MS Analysis. *ANALYTICAL CHEMISTRY* **2011,** *83* (5), 1624-1631.

22. Liu, J. W.; Jiang, X. M.; Ashley, C.; Brinker, C. J., Electrostatically Mediated Liposome Fusion and Lipid Exchange with a Nanoparticle-Supported Bilayer for Control

of Surface Charge, Drug Containment, and Delivery. *J. Am. Chem. Soc.* **2009,** *131* (22), 7567-+.

23. Tero, R.; Takizawa, M.; Li, Y. J.; Yamazaki, M.; Urisu, T., Lipid membrane formation by vesicle fusion on silicon dioxide surfaces modified with alkyl self-assembled monolayer islands. *LANGMUIR* **2004,** *20* (18), 7526-7531.

24. Hardy, G. J.; Nayak, R.; Zauscher, S., Model cell membranes: Techniques to form complex biomimetic supported lipid bilayers via vesicle fusion. *CURRENT OPINION IN COLLOID & INTERFACE SCIENCE* **2013,** *18* (5), 448-458.

25. Cho, N. J.; Frank, C. W.; Kasemo, B.; Hook, F., Quartz crystal microbalance with dissipation monitoring of supported lipid bilayers on various substrates. *NATURE PROTOCOLS* **2010,** *5* (6), 1096-1106.

26. Phillips, K. S.; Wilkop, T.; Wu, J. J.; Al-Kaysi, R. O.; Cheng, Q., Surface plasmon resonance imaging analysis of protein-receptor binding in supported membrane arrays on gold substrates with calcinated silicate films. *J. Am. Chem. Soc.* **2006,** *128* (30), 9590-9591.

27. Brinker, C. J., HYDROLYSIS AND CONDENSATION OF SILICATES - EFFECTS ON STRUCTURE. *JOURNAL OF NON-CRYSTALLINE SOLIDS* **1988,** *100* (1-3), 31-50.

28. Jackman, J. A.; Tabaei, S. R.; Zhao, Z. L.; Yorulmaz, S.; Cho, N. J., Self-Assembly Formation of Lipid Bilayer Coatings on Bare Aluminum Oxide: Overcoming the Force of Interfacial Water. *ACS Appl. Mater. Interfaces* **2015,** *7* (1), 959-968.

29. van Weerd, J.; Karperien, M.; Jonkheijm, P., Supported Lipid Bilayers for the Generation of Dynamic Cell-Material Interfaces. *Adv. Healthc. Mater.* **2015,** *4* (18), 2743-2779.

30. Lopez-Beltran, A.; Cheng, L.; Gevaert, T.; Blanca, A.; Cimadamore, A.; Santoni, M.; Massari, F.; Scarpelli, M.; Raspollini, M. R.; Montironi, R., Current and emerging bladder cancer biomarkers with an emphasis on urine biomarkers. *EXPERT REVIEW OF MOLECULAR DIAGNOSTICS* **2020,** *20* (2), 231-243.

31. Stephan, C.; Ralla, B.; Jung, K., Prostate-specific antigen and other serum and urine markers in prostate cancer. *BIOCHIMICA ET BIOPHYSICA ACTA-REVIEWS ON CANCER* **2014,** *1846* (1), 99-112.

32. Wasung, M. E.; Chawla, L. S.; Madero, M., Biomarkers of renal function, which and when? *CLINICA CHIMICA ACTA* **2015,** *438*, 350-357.

33. Frantzi, M.; van Kessel, K. E.; Zwarthoff, E. C.; Marquez, M.; Rava, M.; Malats, N.; Merseburger, A. S.; Katafigiotis, I.; Stravodimos, K.; Mullen, W.; Zoidakis, J.; Makridakis, M.; Pejchinovski, M.; Critselis, E.; Lichtinghagen, R.; Brand, K.; Dakna, M.; Roubelakis, M. G.; Theodorescu, D.; Vlahou, A.; Mischak, H.; Anagnou, N. P., Development and Validation of Urine-based Peptide Biomarker Panels for Detecting Bladder Cancer in a Multi-center Study. *CLINICAL CANCER RESEARCH* **2016,** *22* (16), 4077-4086.

34. Aragon, C. C.; Tafur, R. A.; Suarez-Avellaneda, A.; Martinez, M. T.; de las Salas, A.; Tobon, G. J., Urinary biomarkers in lupus nephritis. *JOURNAL OF TRANSLATIONAL AUTOIMMUNITY* **2020,** *3*.

35. Klein, J.; Bascands, J. L.; Mischak, H.; Schanstra, J. P., The role of urinary peptidomics in kidney disease research. *KIDNEY INTERNATIONAL* **2016,** *89* (3), 539-545.

36. Rovin, B. H.; Song, H. J.; Birmingham, D. J.; Hebert, L. A.; Yu, C. Y.; Nagaraja, H. N., Urine chemokines as biomarkers of human systemic lupus erythematosus activity. *JOURNAL OF THE AMERICAN SOCIETY OF NEPHROLOGY* **2005,** *16* (2), 467-473.

37. Jakiela, B.; Kosalka, J.; Plutecka, H.; Wegrzyn, A. S.; Bazan-Socha, S.; Sanak, M.; Musial, J., Urinary cytokines and mRNA expression as biomarkers of disease activity in lupus nephritis. *LUPUS* **2018,** *27* (8), 1259-1270.

38. Shadpour, P.; Zamani, M.; Aghaalikhani, N.; Rashtchizadeh, N., Inflammatory cytokines in bladder cancer. *JOURNAL OF CELLULAR PHYSIOLOGY* **2019,** *234* (9), 14489-14499.

39. Shafat, M.; Rajakumar, K.; Syme, H.; Buchholz, N.; Knight, M. M., Stent encrustation in feline and human artificial urine: does the low molecular weight composition account for the difference? *UROLITHIASIS* **2013,** *41* (6), 481-486.

40. Mukanova, Z.; Gudun, K.; Elemessova, Z.; Khamkhash, L.; Ralchenko, E.; Bukasov, R., Detection of Paracetamol in Water and Urea in Artificial Urine with Gold Nanoparticle@Al Foil Cost-efficient SERS Substrate. *ANALYTICAL SCIENCES* **2018,** *34* (2), 183-187.

41. Tian, L. M.; Morrissey, J. J.; Kattumenu, R.; Gandra, N.; Kharasch, E. D.; Singamaneni, S., Bioplasmonic Paper as a Platform for Detection of Kidney Cancer Biomarkers. *ANALYTICAL CHEMISTRY* **2012,** *84* (22), 9928-9934.

42. Ikeda, M.; Yoshii, T.; Matsui, T.; Tanida, T.; Komatsu, H.; Hamachi, I., Montmorillonite-Supramolecular Hydrogel Hybrid for Fluorocolorimetric Sensing of Polyamines. *J. Am. Chem. Soc.* **2011,** *133* (6), 1670-1673.

43. Swaminathan, G. J.; Holloway, D. E.; Colvin, R. A.; Campanella, G. K.; Papageorgiou, A. C.; Luster, A. D.; Acharya, K. R., Crystal structures of oligomeric forms of the IP-10/CXCL10 chemokine. *STRUCTURE* **2003,** *11* (5), 521-532.

44. Baldwin, E. T.; Weber, I. T.; Stcharles, R.; Xuan, J. C.; Appella, E.; Yamada, M.; Matsushima, K.; Edwards, B. F. P.; Clore, G. M.; Gronenborn, A. M.; Wlodawer, A., CRYSTAL-STRUCTURE OF INTERLEUKIN-8 - SYMBIOSIS OF NMR AND CRYSTALLOGRAPHY. *PROCEEDINGS OF THE NATIONAL ACADEMY OF SCIENCES OF THE UNITED STATES OF AMERICA* **1991,** *88* (2), 502-506.

45. Vashist, S. K., Comparison of 1-Ethyl-3-(3-Dimethylaminopropyl) Carbodiimide Based Strategies to Crosslink Antibodies on Amine-Functionalized Platforms for Immunodiagnostic Applications. *Disgnostics* **2012,** *2* (3), 23-33.

46. Bally, M.; Bailey, K.; Sugihara, K.; Grieshaber, D.; Voros, J.; Stadler, B., Liposome and Lipid Bilayer Arrays Towards Biosensing Applications. *SMALL* **2010,** *6* (22), 2481-2497.

Chapter 6: Conclusion and Future Perspectives

6.1 Summary of Dissertation Work

The work reported in this dissertation was primarily focused around developing the technological foundations for creating new biosensing and bioanalysis methodologies with surface plasmon resonance (SPR). This ran the gamut from integrating SPR with established bioanalytical techniques (MALDI-MS) for new sensing modalities, to utilizing new technologies (3D printing) to develop novel fabrication techniques (hybrid PDMS-3D printing) for the generation of optical components for SPR, to the introduction of a new material (aluminum) for the fundamental plasmonic response element of SPR. While we have a much better understanding of life and the world around us than we did one hundred years ago, the space of biological systems and biopharmaceutical strategies to analyze increases on a seemingly constant basis. The rapid expansion of understanding of the nanoscale of these biological systems in recent times has largely been driven by improvements in bioanalytical technologies. The techniques used to analyze these biological systems, of which SPR and MALDI are core components, must similarly continuously improve and reveal new dimensions of themselves in order to continue to reveal new dimensions of the natural world. The rest of the chapter will be dedicated to a discussion of the potential of each of these technological upgrades. Though the wide span of possibility is immense, especially with the introduction of a material in aluminum to thin film SPR that is so disparate in its optical and chemical properties from the standard gold, I will be focusing on the areas that can be investigated and improved upon in the immediate future.

6.2 Potential Future Research Areas

6.2.1 Plasmonic MALDI-MS Microarrays

Chapter 2 reported the SPR-MALDI coupling for bacterial protein identification, and there are a range of other food and water-borne bacterial diseases that could be subject to the same treatment. In particular, several bacterial diseases like *E. coli*, *S. enterica typhi*, and *C. difficile*, have similar protein toxins that bind to cell-surface carbohydrate-based moieties as the initial site of host attack before endocytosis and further toxic effects, as shown in Table 1.[1-4] Due to the array-based nature of the SPR-MALDI methodology, each could easily be separately analyzed or multiplexed together to create a multi-toxin monitoring array.

However, the concept of bacterial identification from an easy-to-prepare MALDI-MS signature holds a much broader promise. In industry spaces, there is a need for quick bacterial identification, especially in the areas of food and water safety.[5] Recalls and plant shutdowns for outbreaks of E. coli or Salmonella, to name two prominent examples, cause loss of business, productivity and reputation for the producing companies.[6] My group has recently reported multiple applications of plasmonic Au films being used for lipidomics profiling.[7, 8] MALDI-MS is higher-performing for low molecular weight biomolecules such as lipids, so identifying a high number of them as a component of microbial identification would be a logical next step with high commercial potential. The improved sensitivity of plasmonic thin films towards MALDI ionization make it a good candidate for this type of analysis, and aluminum thin films would likely be advantageous in this

regard. Au films have a relatively low efficiency of UV absorption compared to Al, so Al would likely further improve this profiling and identification capacity.

6.2.2 Polymer Optics

There are also multiple avenues available for the hybrid manufactured polymer prisms. The work presented here focused on the prisms used for SPR and SPR imaging, but in principle any component could be created, especially with the geometrical flexibility inherent in 3D printing. Rotation prisms (such as dove prisms), reflector prisms, and parabolic concentrators all fit similar basic parameters to the equilateral and hemicylindrical prisms presented here, and each has a significant swath of optical and analytical applications available for their use.[9-12] Of course, the optimization of curing times and directionality of the mold would need to be determined through prototyping, but the ease of creating each mold makes this challenge relatively minor. The concept is also simple enough that everyday objects, even something as simple as a ball bearing could be used as the base part that the PDMS mold is made around. The ability to smooth the molds means that the surface of the "everyday" part does not necessarily need to have optical-grade surface finish. Though the ease of manufacture of the polymer molds makes their replication relatively trivial, further development of cleaning procedures for them would help to lengthen their lifespan further and remove even this minor need. Further investigation of the incorporation of additives into the process is also highly promising. A significant portion of ongoing literature in 3D printing is the generation of multiple functionalities or non-plastic parts by the use of hybrid polymerization materials that do not interfere with the 3D printer.[13-17] This hybrid method sidesteps that concern as detailed

in Chapter 3, and the incorporation of nanoparticles or other materials to induce color filters, plasmonic absorbances, higher refractive indices, or polarization effects would be an exciting expansion of the concept.

6.2.3 Expanding Aluminum-based SPR

Al films on commercial instrumentation. While Al films have many benefits as detailed in the previous sections, an aspect that would greatly aid their implementation in SPR-based techniques is if they could easily be used in existing instrumentation. This is not a given, since the plasmonic "dip" for Al at optimal film thickness is shifted by ~ 7 ° compared to Au. While commercial instruments, such those made by as Biacore or Bruker Sierra, typically measure by angular shift rather than wavelength shift, the physical configuration usually has a fixed optical stage so as to minimize the number of moving parts.[18] Angular spectra are generated by collecting reflected light across a linear photodiode array. How optimized this linear array is creates an initial challenge, as the array could have an angular "cut-off" that does not capture the Al dip as effectively as the Au dip. This was not an issue with the NanoSPR and home-built instruments used in the preceding chapters, as the incident angle range could easily be tuned on each.

We investigated this potential by 3D-printing a slide and slide-holder that could be compatibly inserted into a BiacoreX instrument (GE Healthcare Life Sciences, Chicago, IL) in place of their proprietary chips and depositing 18 nm Al film on a microscope slide cover slip that could be attached to the slide via Gorilla Super Glue (Cincinnati, OH) in place of a Au film slip, similar to previous work.[19] The assembly was inserted into the instrument, and SPR spectra were obtained. It is difficult to make absolute angle

comparisons since Biacore uses "pixels" rather than angles, but the plasmonic dip is barely visible with H_2O on the surface. The spectrum generated by the algorithm the software uses to improve the dip detection looks improved, though it still retains high noise in comparison to spectra from previous chapters. Additionally, NaCl solutions of varying refractive index were incubated to test online data acquisition and bulk sensitivity. A sensorgram of the incubations along with a preliminary calibration are in Fig xxxx, and both indicate good linearity of response. Biacore uses a semi-arbitrary "Resonance Unit" in its sensorgrams rather than angles, so it is again difficult to precisely track the sensitivity in an absolute sense, but their operator materials mention that 10000 RU ≈ 1 °.[20] If taken concretely, this translates into a sensitivity of ~ 52.96 °/RIU, which is close to the sensitivity reported in Chapter 4 of 59.25 °/RIU. This indicates that Al films perform well on a standard Biacore instrument and could be a significant potential area of development.

Expanding Al/Al_2O_3 surface optimization and functionalization. While the silanization of the Al/Al_2O_3 surface was reported for biosensing in Chapter 5, the sensitivity has much room to improve. Furthermore, while we did not find significant difficulty with film stability over the course of our experiments, this aspect is still the largest area of concern for commercial applications.[21-23] A more robust oxide layer (greater than the natively-forming 3 nm Al_2O_3) may be a pathway to improved performance on both of these fronts. Aluminum itself is very reactive, and the oxide layer protects it from dissolving as Al^{3+} or $Al(OH)^{4-}$ in aqueous solutions.[24] An increase of oxide on the surface will reduce any leakage of water or buffer to the Al metal, thus improving stability. An increased oxide layer will also make functionalization more robust, as more oxygen will

be incorporated into the chip surface, and the various surface chemistry pathways like silanization are dependent on coordinating with the oxygen on the surface.

This increased oxide can be accomplished by multiple means, such as annealing with low partial pressures of oxygen, directly deposited via RF sputtering, electron beam deposition (EBPVD) or atomic layer deposition (ALD), or electrochemically anodized.[25-28] The increase of surface oxide has the potential added benefit of increased base sensitivity. Fresnel-based calculations indicate that while increased oxide layer marginally shifts the base angular spectra, it may not do so at a cost to refractive index sensitivity. In fact, up to a ~24 nm additional oxide, the sensitivity is calculated to increase slightly by ~4 %. More routes of functionalization are also available that may have higher base efficiency than silanization and may not necessarily require the oxide enhancement. The application of Al functionalization is much-less well established than Au for SPR biosensing, but the existing literature on Al_2O_3 functionalization has a number of reports on carboxylation[29, 30] and phosphonylation[31, 32] in addition to silanization that could be adapted for this purpose. Combining these with more complex implementations of biomolecule immobilization, such as EDC/NHS activation, hydroxyl groups, PEG linkers, and maleimide linkages, is a promising area of investigation going forward.

6.3 References

1. Karve, S. S.; Weiss, A. A., Glycolipid Binding Preferences of Shiga Toxin Variants. *PLOS ONE* **2014,** *9* (7).

2. Deng, L. Q.; Song, J. M.; Gao, X.; Wang, J. W.; Yu, H.; Chen, X.; Varki, N.; Naito-Matsui, Y.; Galan, J. E.; Varki, A., Host Adaptation of a Bacterial Toxin from the Human Pathogen Salmonella Typhi. *CELL* **2014,** *159* (6), 1290-1299.

3. Clark, G. F.; Krivan, H. C.; Wilkins, T. D.; Smith, D. F., TOXIN-A FROM CLOSTRIDIUM-DIFFICILE BINDS TO RABBIT ERYTHROCYTE GLYCOLIPIDS WITH TERMINAL GAL-ALPHA-1-3GAL-BETA-1-4GLCNAC SEQUENCES. *ARCHIVES OF BIOCHEMISTRY AND BIOPHYSICS* **1987,** *257* (1), 217-229.

4. Imberty, A.; Varrot, A., Microbial recognition of human cell surface glycoconjugates. *CURRENT OPINION IN STRUCTURAL BIOLOGY* **2008,** *18* (5), 567-576.

5. Belias, A.; Brassill, N.; Roof, S.; Rock, C.; Wiedmann, M.; Weller, D., Cross-Validation Indicates Predictive Models May Provide an Alternative to Indicator Organism Monitoring for Evaluating Pathogen Presence in Southwestern US Agricultural Water. *FRONTIERS IN WATER* **2021,** *3*.

6. Houser, M.; Dorfman, J. H., The Long-Term Effects of Meat Recalls on Futures Markets. *APPLIED ECONOMIC PERSPECTIVES AND POLICY* **2019,** *41* (2), 235-248.

7. Shanta, P. V.; Li, B.; Stuart, D. D.; Cheng, Q., Plasmonic Gold Templates Enhancing Single Cell Lipidomic Analysis of Microorganisms. *Analytical Chemistry* **2020,** *92* (9), 6213-6217.

8. Li, B.; Stuart, D. D.; Shanta, P. V.; Pike, C. D.; Cheng, Q., Probing Herbicide Toxicity to Algae (Selenastrum capricornutum) by Lipid Profiling with Machine Learning and Microchip/MALDI-TOF Mass Spectrometry. *Chemical Research in Toxicology* **2022,** *35* (4), 606-615.

9. Huckabay, H. A.; Wildgen, S. M.; Dunn, R. C., Label-free detection of ovarian cancer biomarkers using whispering gallery mode imaging. *BIOSENSORS & BIOELECTRONICS* **2013,** *45*, 223-229.

10. Breault-Turcot, J.; Poirier-Richard, H. P.; Couture, M.; Pelechacz, D.; Masson, J. F., Single chip SPR and fluorescent ELISA assay of prostate specific antigen. *LAB ON A CHIP* **2015,** *15* (23), 4433-4440.

11. Nie, Y.; Sanna, A.; Kokkonen, A.; Sipola, T.; Sanna, U.; Grilli, S.; Ottevaere, H. In *Optical aspects of a miniature fluorescence microscope for super-sensitive*

biomedical detection, Biophotonics Congress: Biomedical Optics 2020 (Translational, Microscopy, OCT, OTS, BRAIN), Washington, DC, 2020/04/20; Optica Publishing Group: Washington, DC, 2020; p MTh4A.3.

12. Vaidya, N.; Solgaard, O., 3D printed optics with nanometer scale surface roughness. *Microsyst. Nanoeng.* **2018,** *4*, 18.

13. Kotz, F.; Arnold, K.; Bauer, W.; Schild, D.; Keller, N.; Sachsenheimer, K.; Nargang, T. M.; Richter, C.; Helmer, D.; Rapp, B. E., Three-dimensional printing of transparent fused silica glass. *Nature* **2017,** *544* (7650), 337-339.

14. Cooperstein, I.; Shukrun, E.; Press, O.; Kamyshny, A.; Magdassi, S., Additive Manufacturing of Transparent Silica Glass from Solutions. *ACS Appl. Mater. Interfaces* **2018,** *10* (22), 18879-18885.

15. Destino, J. F.; Dudukovic, N. A.; Johnson, M. A.; Nguyen, D. T.; Yee, T. D.; Egan, G. C.; Sawvel, A. M.; Steele, W. A.; Baumann, T. F.; Duoss, E. B.; Suratwala, T.; Dylla-Spears, R., 3D Printed Optical Quality Silica and Silica-Titania Glasses from Sol-Gel Feedstocks. *Adv. Mater. Technol.* **2018,** *3* (6), 1700323.

16. Nguyen, D. T.; Meyers, C.; Yee, T. D.; Dudukovic, N. A.; Destino, J. F.; Zhu, C.; Duoss, E. B.; Baumann, T. F.; Suratwala, T.; Smay, J. E.; Dylla-Spears, R., 3D-Printed Transparent Glass. *Adv. Mater.* **2017,** *29* (26), 1701181.

17. Haring, A. P.; Khan, A. U.; Liu, G. L.; Johnson, B. N., 3D Printed Functionally Graded Plasmonic Constructs. *Adv. Opt. Mater.* **2017,** *5* (18), 1700367.

18. Wilson, W. D., Analyzing biomolecular interactions. *SCIENCE* **2002,** *295* (5562), 2103-+.

19. Tran, K. Development of Nanofiber and Surface Plasmon Resonance Sensors for VOCs, Biochemical, and Bacterial Analysis. University of California - Riverside, Riverside, CA, USA, 2020.

20. Roper, D. K., Determining Surface Plasmon Resonance Response Factors for Deposition onto Three-Dimensional Surfaces. *Chem Eng Sci* **2007,** *62* (7), 1988-1996.

21. Jha, R.; Sharma, A. K., High-performance sensor based on surface plasmon resonance with chalcogenide prism and aluminum for detection in infrared. *Optics Letters* **2009,** *34* (6), 749-751.

22. Correa, G. C.; Bao, B.; Strandwitz, N. C., Chemical Stability of Titania and Alumina Thin Films Formed by Atomic Layer Deposition. *ACS Appl. Mater. Interfaces* **2015,** *7* (27), 14816-14821.

23. Oliveira, L. C.; Herbster, A.; Moreira, C. D. S.; Neff, F. H.; Lima, A. M. N., Surface Plasmon Resonance Sensing Characteristics of Thin Aluminum Films in Aqueous Solution. *IEEE Sens. J.* **2017,** *17* (19), 6258-6267.

24. Housecroft, C. E.; Sharpe, A. G., *Inorganic Chemistry*. 4th ed ed.; Pearson Educational: 2012.

25. Dutta, S.; Biser, J. M.; Vinci, R. P.; Chan, H. M., Solid State Annealing Behavior of Aluminum Thin Films on Sapphire. *Journal of the American Ceramic Society* **2012,** *95* (2), 823-830.

26. John, H.; Hausner, H., Influence of oxygen partial pressure on the wetting behaviour in the system Al/Al2O3. *Journal of Materials Science Letters* **1986,** *5* (5), 549-551.

27. Lee, W.; Park, S.-J., Porous Anodic Aluminum Oxide: Anodization and Templated Synthesis of Functional Nanostructures. *Chemical Reviews* **2014,** *114* (15), 7487-7556.

28. Sanz, O.; Echave, F. J.; Odriozola, J. A.; Montes, M., Aluminum Anodization in Oxalic Acid: Controlling the Texture of Al2O3/Al Monoliths for Catalytic Aplications. *Industrial & Engineering Chemistry Research* **2011,** *50* (4), 2117-2125.

29. Al-Shatty, W.; Lord, A. M.; Alexander, S.; Barron, A. R., Tunable Surface Properties of Aluminum Oxide Nanoparticles from Highly Hydrophobic to Highly Hydrophilic. *Acs Omega* **2017,** *2* (6), 2507-2514.

30. Debrassi, A.; Ribbera, A.; de Vos, W. M.; Wennekes, T.; Zuilhof, H., Stability of (Bio)Functionalized Porous Aluminum Oxide. *Langmuir* **2014,** *30* (5), 1311-1320.

31. Hoque, E.; DeRose, J. A.; Kulik, G.; Hoffmann, P.; Mathieu, H. J.; Bhushan, B., Alkylphosphonate modified aluminum oxide surfaces. *J. Phys. Chem. B* **2006,** *110* (22), 10855-10861.

32. Portilla, L.; Halik, M., Smoothly Tunable Surface Properties of Aluminum Oxide Core-Shell Nanoparticles By A Mixed-Ligand Approach. *ACS Appl. Mater. Interfaces* **2014,** *6* (8), 5977-5982.